

**LIBRARY
Michigan State
University**

This is to certify that the
dissertation entitled

**LATTICE BOLTZMANN SIMULATION OF LASER
INTERACTION WITH WEAKLY IONIZED PLASMAS**

presented by

Huayu Li

has been accepted towards fulfillment
of the requirements for the

Ph.D. degree in Mechanical Engineering



Major Professor's Signature

10/13/2008

Date

Date

PLACE IN RETURN BOX to remove this checkout from your record.
TO AVOID FINES return on or before date due.
MAY BE RECALLED with earlier due date if requested.

DATE DUE	DATE DUE	DATE DUE

LATTICE BOLTZMANN SIMULATION OF LASER INTERACTION WITH
WEAKLY IONIZED PLASMAS

By

Huayu Li

A DISSERTATION

Submitted to
Michigan State University
in partial fulfillment of the requirements
for the degree of

DOCTOR OF PHILOSOPHY

Mechanical Engineering

2008

ABSTRACT

LATTICE BOLTZMANN SIMULATION OF LASER INTERACTION WITH WEAKLY IONIZED PLASMAS

By

Huayu Li

Laser-plasma interaction (LPI) is an important subject to a variety of disciplines in engineering and science, such as laser welding, pulsed laser deposition (PLD), laser-generated x-rays and laser-aided ignition of inertial confinement fusion (ICF). In particular, laser interaction with weakly ionized plasmas has invoked a great deal of interest to the laser manufacturing community because plasmas naturally appear and interact with a laser beam in such high energy manufacturing processes. Due to the complexity and richness of physics, numerical model studies have been pivotal in the understanding of LPI. A number of numerical models have been created to study LPI and help design LPI equipment, and there are basically two kinds of numerical models: the kinetic-based model and the hydrodynamic model. Although kinetic models (e.g., particle-in-cell model) have been very successful, they are computationally expensive in most cases and their application is rather limited. Hydrodynamic models are also a powerful tool for LPI simulations, but they fail in some circumstances because they are based on the continuum assumption.

In this study, a new numerical model based on the lattice Boltzmann method (LBM) is introduced to simulate laser interaction with weakly-ionized plasmas. The LBM

is a kinetic theory based method, where the distribution functions of the individual species of particles in the plasma are solved and thus the macroscopic variables (such as number density and momentum) are obtained. In this study, the Boltzmann equation with ionization and recombination terms is solved. Since only number density and momentum can be correctly retrieved from the two-dimensional nine-bit (D2Q9) discretization scheme, a set of energy equations is derived from the Boltzmann equation and solved separately to calculate temperature fields. The electromagnetic field from both laser and plasma is updated by solving Maxwell's equations using the finite-difference time-domain (FDTD) method. In the implementation of the present model, a rescaling scheme is introduced to select the appropriate simulation parameters for the LBM, so that the physical properties of the plasma can be used. This rescaling scheme has been validated by hydrodynamic flow problems and the electron diffusion problem. In this study, a two-dimensional weakly-ionized helium plasma interaction with a continuous wave CO₂ laser beam is simulated.

This model is a mesoscale approach based on the kinetic theory and the LBM, so it has a number of inherent advantages over previous models. Because the LBM solver is employed, this approach is computationally efficient and easy to parallelize. In addition, this model is capable of predicting time-dependent number densities, velocities, and temperatures of all particle species for a fairly large scale problem without employing the continuum assumption. It is believed that this model has a lot of potential for the studies of weakly ionized plasmas in a wide spectrum of applications.

DEDICATED TO MY WIFE AND MY PARENTS

ACKNOWLEDGEMENT

I would like to deeply acknowledge my advisor, committee members, colleagues and families, because this thesis work could not have been done without their support and/or contribution.

First of all, I wish to express my special appreciation to my advisor, Professor Hyungson Ki, whose guidance and directions have been greatly supportive throughout my entire Ph.D. studies. In the summer of 2004, I joined Dr. Ki's team and started my research on modeling laser interactions with matters by using the lattice Boltzmann method under his supervision. He spent enormous time and energy to help me to start as a self-motivated graduate student. I am especially grateful not only for his patience and encouragement on the academic side, but also for his generous supports in my personal life.

I also would like to thank my committee members, Dr. Andre Benard, Dr. Patrick Kwon and Dr. Timothy Grotjohn, whose advice and comments were greatly valuable and helpful for my research and dissertation.

Working with my previous and current colleagues and friends, Kuiyan Xu, Mehdi Abarham, Taylor Young, Brian Powell, Ankit Aggarwal and Admir Trnjanin, makes the past five-year unforgettable. Their friendship, help and encouragement will remain in my memory.

Finally, I would thank my families, my wife Lei Jin, my parents and my in-laws. They have spent extensive time and efforts to support me. Their immeasurable loves and understandings are overwhelming and go beyond words.

TABLE OF CONTENTS

LIST OF TABLES	viii
LIST OF FIGURES	ix
NOMENCLATURE	xiv
CHAPTER 1	
BRIEF REVIEW OF LASER-PLASMA INTERACTIONS	1
1.1 Physics of laser-plasma interactions	1
1.2 Applications of laser-plasma interaction	6
1.3 Numerical Models.....	9
1.4 Main Content of This Research	23
CHAPTER 2	
LATTICE BOLTZMANN METHOD FOR INCOMPRESSIBLE HYDRODYNAMICS FLOWS	26
2.1 Boltzmann Transport Equation and Its Collision Term.....	26
2.2 From Boltzmann Equation to Lattice Boltzmann Equation.....	31
2.3 From Lattice Boltzmann Equation to Navier-Stokes Equation	36
2.4 LBM Simulation of Two-dimensional Driven Cavity Flow.....	40
CHAPTER 3	
EVALUATION OF THE EXTERNAL FORCE TERM IN LATTICE BOLTZMANN METHOD	43
3.1 Different External Force Models	43
3.2 LBM Simulation of Magnetohydrodynamics Flows	56
CHAPTER 4	
LATTICE BOLTZMANN SIMULATION OF ISOTHERMAL WEAKLY IONIZED PLASMAS	73
4.1 Mathematical Model	74
4.2 Rescaling Scheme	80
4.3 Simulation Results	98
CHAPTER 5	
LATTICE BOLTZMANN SIMULATION OF WEAKLY IONIZED HELIUM PLASMA WITH IONIZATION AND RECOMBINATION	108
5.1 Mathematical Model	108
5.2 Finite-Difference Time-Domain Method.....	115
5.3 Numerical Implementation	122
5.4 Simulation Results	131

CHAPTER 6	
CONCLUSION.....	150
REFERENCE.....	154

LIST OF TABLES

Table 1 F_α and \mathbf{u}^* in different external force models	47
Table 2 Relative errors ($\times 10^4$) of Poiseuille flow	49
Table 3 Relative errors ($\times 10^5$) of free diffusion problem	54
Table 4 Quantitative comparison of simulation results with Dellar's work	67
Table 5 Simulation parameters and simulation errors for different values of τ in the simulation of two-dimensional driven cavity flows.....	91
Table 6 Two examples of the air state that give invalid dimensionless relaxation time ..	94
Table 7 Rescaled simulation parameters and # of iterations until convergence	94
Table 8 Simulation parameters for air at 300 K and 1 atm (Case 1)	95
Table 9 Simulation parameters used for the electron diffusion problem.....	99
Table 10 Macroscopic Quantities from Moments of Distribution Function.....	113
Table 11 Primary simulation variables	126
Table 12 Secondary simulation variables	127

LIST OF FIGURES

- Figure 1 Schematic of D2Q9 square lattice. The two-dimensional continuous phase space is discretized by nine microscopic velocity components in a square lattice..... 34
- Figure 2 Streamlines of driven cavity flow with different Reynolds numbers. The flow pattern is strongly dependent on the Reynolds number. If the Reynolds number is sufficiently large, secondary vortices appear at the right and left lower corners. 41
- Figure 3 (a) Velocity profiles for u through the geometric center of the cavity; (b) Velocity profiles for v through the geometric center of the cavity..... 42
- Figure 4 Profile of x -component velocity obtained by He's model ($g = 5.774 \times 10^{-2}$). The simulation results agree very well with the analytical solution.. 50
- Figure 5 Evolution of relative errors of simulation of Taylor vortex flow obtained by the five external force models. All the errors are in the same order of values. 51
- Figure 6 Profiles of x -component velocity along the center line of x -axis at time steps of 1500 and 3000 by using He's model. The simulation results are in good agreement with the analytical solutions..... 52
- Figure 7 Fluid density distribution obtained by He's model and Guo's model at 200 time steps with different magnitudes of the external force: (a) $a_x = 4.0$ (b) $a_x = 10.0$. Both Guo's model and He's model can produce good results if the external force is small (as shown in (a)). However, if the external force is relatively large, Guo's model induces larger error than dose He's model (as shown in (b)). 55
- Figure 8 Profiles of x -component velocity with different Hartmann numbers: $M=0$ (squares), $M=1$ (circles), $M=2$ (upper triangles), $M=5$ (lower triangles), $M=10$ (diamonds), $M=20$ (stars). The solid lines show the analytical solutions. The simulation results agree very well with the analytical solutions. 62
- Figure 9 Profiles of x -component magnetic field for different Hartmann numbers: $M=0$ (squares), $M=1$ (circles), $M=2$ (upper triangles), $M=5$ (lower triangles), $M=10$ (diamonds), $M=20$ (stars). The solid lines show the analytical solutions. The simulation results agree very well with the analytical solutions.. 62
- Figure 10 Evolution of vorticity for the 2-D Orszag-Tang vortex. The flow pattern becomes complicated due to the nonlinear interactions between the velocity field and the magnetic field. A flat quadrupole-like configuration emerges with time lapse..... 64

Figure 11 Evolution of current density for the 2-D Orszag-Tang vortex. The existing current sheet at the center of the figure is enhanced and eventually, a thin elliptic structure establishes due to the magnetic reconnection occurring there..... 65

Figure 12 Iso-surface contours of magnitudes of vorticity and current density at $t=0$ and $t=0.598$ sec for the 3-D Orszag-Tang vortex. The patterns of the current sheet and the corresponding vorticity resemble Figure 11 and Figure 10 closely because initially, the variations of current density and vorticity in z-directions are relatively smaller in values than those in the x-and y-direction..... 69

Figure 13 Evolution of magnetic flux function for doubly periodic coalescence instability. The position of the magnetic current sheets does not change with time. The magnetic islands move towards each other. The two corners coalesce into one and the original two square cells become two adjacent pentagons. A current sheet forms between the two cells and the intensity of the current sheet increases. Eventually, the neighboring square cells merge together, simplifying the topology structure of the magnetic field to four square-like islands. 71

Figure 14 Maximum value of current density vs. magnetic diffusivity. The temporal maximum of current density can be approximated as $j_{\max} \propto \eta^{-1/2}$ 72

Figure 15 Schematic of second order interpolation method for ion (neutral) distribution function. The value of distribution function of the heavy particles at p can be found by using the post-collision values at o' , p' and q' 79

Figure 16 Distribution of electron number density at $t = 3.5$ ns. Non-physical peaks appear if the physical variables of electrons are used..... 84

Figure 17 Electron number density distribution at (a) $t = 1.116$ ns and (b) $t = 3.347$ ns with different ionization degrees. Non-physical sub-peaks caused by using the physical variables travel with the constant lattice speed. A higher ionization degree leads to a higher lattice speed. The ratio of the magnitude of the sub-peaks to that of the primary peak corresponds to the value of the ratio of the weight coefficients..... 85

Figure 18 Contour plot of electron number density at $t = 1.116$ ns. The distribution of electrons is along with the discretized velocity directions if the effects of collisions are not included in LBM..... 86

Figure 19 Velocity profiles along the central lines of the computational domain obtained by using the physical properties of air without the rescaling when the dimensionless relaxation time is in the valid range. (a) dimensionless x -velocity (b) dimensionless y -velocity..... 90

Figure 20 Number of iterations until convergence vs. τ ($Re = 200$). A larger τ leads to a quicker convergence.. 92

Figure 21 (a) τ as a function of Re and Ma (N=128). It is apparent that τ needs to be close to 0.5 if a high Ma and/or a high Re are desired. (b) Re vs. τ at different grid densities. Increasing grid density is an effective way to increase Re if the other simulation parameters are kept unchanged. 93

Figure 22 Locations of the primary vortices at different Reynolds numbers. The simulation results obtained by the rescaling scheme agree well with other researchers' results. 95

Figure 23 Velocity profiles along the central lines of the computational domain (a) dimensionless x-velocity (b) dimensionless y-velocity. The simulation errors are relatively large if the Reynolds number is high. It is due to the high Mach number resulted by the high Reynolds number according to Eq. (119). 97

Figure 24 Electron number density distributions with different initial number densities of neutrals. The simulation results obtained by the rescaling scheme are in good agreement with the analytical solutions. 100

Figure 25 Electron number density distribution (Circle: without internal electric field, Squares: with internal electric field, both at 0.223 ns. Solid line shows the initial distribution). The internal electric field generated by the charge density largely enhances the electron diffusion process. 102

Figure 26 Snapshot of electron number density (solid lines) and ion number density (dashed lines) at $t = 1.116$ ns. The electrons and ions move along opposite directions because they have opposite charges. The ions travel much more slowly than the electrons since the ions have much heavier mass. 103

Figure 27 Electron number density distribution (at $t = 6.69$ ns) obtained by using different equilibrium distribution functions for the external force term. Apparent simulation errors would be resulted by using the cross-collision equilibrium distribution function in He's external force model. 104

Figure 28 Relative errors in electron number density vs. time for three different grids. The errors are calculated at the center of the domain with comparison to the analytical solution. Second order accuracy in space discretization can be seen from the figure. ... 105

Figure 29 Time evolution of number density and x-component velocity of electrons at the center of the computational domain. (Solid lines: simulation results obtained without the rescaling scheme, circles and squares: simulation results obtained with the rescaling scheme) 106

Figure 30 Position of the electric and magnetic field vector components about a cubic unit cell of the Yee space lattice 117

Figure 31 Schematic of computational domain for simulation of a femtosecond laser pulse interaction with a silicon substrate. 118

Figure 32 Time history of laser pulse propagation. (In these plots, the radial component of the electric field (E_r) is used.).....	120
Figure 33 Time history of laser energy absorbed by electrons.....	121
Figure 34 Schematic of the rescaling scheme. The value of distribution function at p can be found by using the post-collision values at o' , p' and q'	125
Figure 35 Positions of the simulation variables. H_z , n_s , u_s and T_s are calculated at the white node points while E_x and E_y are staggered in space and evaluated at the black node points.....	126
Figure 36 Flowchart of the present model.....	130
Figure 37 Correlation among three equations.....	131
Figure 38 Schematic of the computational domain for simulation of interaction between a continuous CO_2 laser beam and a weakly ionized helium plasma.....	132
Figure 39 Evolution of maximum electron number density with different laser intensities. At the early stage, the electron number density increases exponentially because of the laser-induced ionization. However, it shows saturation later due to the equilibrium between ionization and recombination.	133
Figure 40 Evolution of maximum electron temperature with different laser intensities. The electron temperature increases very quickly due to the rapid heating. It decreases after the ionization takes place because the generation of new free electrons consumes the laser energy.	134
Figure 41 Evolution of ionization coefficient with different laser intensities. The ionization coefficient shows a similar pattern with the electron temperature because it mainly dependent on the electron energy.	135
Figure 42 Evolution of recombination coefficient under different laser intensities. The recombination coefficient increases due to the generation of new free electrons and the decrease of the electron temperature.....	136
Figure 43 Evolution of maximum ion temperature with different laser intensities. Compared to the electron temperature, the ion temperature increases with a lower rate because of the heavy mass. It decreases due to the attenuation of the electric field.	137
Figure 44 Evolution of neutral temperature with different laser intensities. Unlike the temperatures of electrons and ions, the neutral temperature keeps increasing because the neutrals are heated by the cross-heat transfer from the charged particles.	138
Figure 45 Distribution of electron temperature along beam propagation axis at different time moments. The highest temperature always appears at the interface.....	139

Figure 46 Distribution of electron number density along the beam propagation axis at different time moments. Most of the new free electrons are generated near the interface.	139
Figure 47 Snapshots of electron and neutral number densities at (a) $t = 49.93$ ps and (b) $t = 149.80$ ps.....	140
Figure 48 Contours of electron temperature at (a) $t = 4.86$ ps, (b) $t = 13.26$ ps, (c) $t = 49.93$ ps and (d) 149.80 ps.....	142
Figure 49 Electron number density distribution along x-axis at $j = 195$ at different time moments.....	143
Figure 50 Snapshot of (a) impact ionization coefficient and (b) recombination coefficient at $t = 149.80$ ps.....	143
Figure 51 Snapshots of Joule heating at (a) $t = 4.86$ ps, (b) $t = 13.26$ ps, (c) $t = 49.93$ ps and (d) $t = 149.80$ ps.....	145
Figure 52 Snapshots of x-component of electric field at (a) $t = 4.86$ ps, (b) $t = 13.26$ ps, (c) $t = 49.93$ ps and (d) $t = 149.80$ ps.....	146
Figure 53 Evolution of (a) number densities (b) temperatures (c) ionization and recombination coefficients and (d) magnitude of electric field at Point A.....	148

NOMENCLATURE

$\mathbf{a}_{e(i)}$	Acceleration of charged particles caused by the external force
a_x	x-component of the acceleration
a_y	y-component of the acceleration
B	Magnetic induction (magnetic flux density)
B_x	x-component of magnetic induction
B_y	y-component of magnetic induction
c_s	Lattice speed of particle species s
D	Diffusivity
D	Electric flux density
E	Electric field
E_x	x-component of the electric field
E_y	y-component of the electric field
e	Unit electronic charge
\mathbf{e}_s^α	Discretized microscopic velocity of particle species s along the α -th direction
f_s	Single particle distribution function of particle species s
f_s^{eq}	Self-collision equilibrium distribution function of particle species s
$f_{ss'}^{eq}$	Cross-collision equilibrium distribution function of particle species s due to the binary collisions with particle species s'

F_α	Discretized external force term along the α -th direction
g	Pressure gradient
\mathbf{H}	Magnetic field
H_z	z-component of the magnetic field
\mathbf{J}	Electric current density
k_B	Boltzmann constant
L_0	Characteristic length of the flow problem
m_s	Mass of particle species s
n_s	Number density of particle species s
N_x	Number of grids along x-direction
N_y	Number of grids along y-direction
\mathbf{P}_s	Kinetic pressure dyad of particle species s
q_s	Electronic charge of particle species s
\mathbf{q}_s	Heat flux of particle species s
R_s	Ionization and recombination coefficient of particle species s
T_s	Temperature of particle species s
$T_{e(i)n}$	Post-collision temperature of electrons (ions) due to binary collisions with neutrals
\mathbf{u}_s	Macroscopic velocity of particle species s
$\mathbf{u}_{e(i)n}$	Barycentric velocity of electrons (ions) due to binary collisions with neutrals
\mathbf{u}_s^*	Equilibrium macroscopic velocity of particle species s

U_0	Characteristic velocity of the flow
U_i	First ionization potential of helium
\mathbf{v}_s	Microscopic velocity of particles species s
\mathbf{v}_d	Drift velocity
β_s	Interpolation parameter of particle species s
ϵ_0	Electrical permittivity in free space
ϵ_s	Total energy of particle species s
ϵ_{Ts}	Thermal energy of particle species s
γ_s	Rescaling parameter of particles species s
η	Magnetic diffusivity
κ_s	Thermal conductivity of particles species s
$\lambda_{ss'}$	Relaxation time of particle species s due to the binary collisions with particle species s'
μ	Magnetic permeability
ν	Fluid viscosity
$\tilde{\nu}$	Lattice viscosity
θ_s	Sound speed of particle species s
$\tilde{\theta}_s$	Lattice sound speed of particle species s
ρ_s	Mass density of particle species s
ρ_V	Charge density
σ	Electrical conductivity

σ_{sn}	Cross section of binary collisions between particle species s and n
σ_i	Cross section of electron impact ionization
τ_s	Dimensionless relaxation time of particle species s
Δt	Time step
Δx	Space step along x-direction
Δy	Space step along y-direction

Chapter 1

Brief Review of Laser-Plasma Interactions

Laser-plasma interactions are of great interests to researchers from many different fields of expertise. The characteristics of laser-plasma interactions are high nonlinearity, strong coupling, large spans of spatial and temporal scales, and multiple physics. A complete description of laser-plasma interactions should include laser-induced ionization, absorption of laser energy, plasma responses and electromagnetic wave propagation inside the plasma, all of which are strongly coupled and dependent upon the incident laser intensity. The higher the laser intensity, the more complicated the physics involved will be. In this chapter, the physics, applications and numerical models of laser-plasma interactions will be briefly reviewed. The main content of this dissertation is also introduced.

1.1 Physics of laser-plasma interactions

When a laser beam impinges on a target which is initially in non-plasma state, the neutral atoms or molecules will be excited and free electrons will be generated if the laser irradiance (or intensity) exceeds some threshold. For metals, in which there are already “free” electrons in the conduction band, the electron impact ionization caused by the thermal collisions between electrons and heavy particles (ions and neutral particles) dominates the ionization process. The impact ionization mainly depends on the electron energy that is obtained from the incident laser beam through inverse bremsstrahlung heating. For dielectrics, there is a well-defined threshold for the laser-induced breakdown

which depends on the laser pulse duration [1, 2], the wavelength of the incident laser pulse [3] and the band gap or ionization potential of the material. Besides the impact ionization, the multi-photon ionization also plays an important role in laser-induced breakdown of dielectric. In the multi-photon ionization, the laser energy carried by the photons shifts the electrons from the valence band to the conduction band and thus produces the “feed electrons” for the following impact ionization. If the laser intensity is high enough, the strong electric field of the laser beam will distort the potential barrier of the atom (or molecule) drastically. The electrons can pass the barrier easily to become free electrons. This ionization mechanism is referred as to tunneling ionization or field ionization. Laser-induced ionization of gases has similar mechanisms as the dielectrics. Parameters of the incident laser beam, ionization potential of the gas and the gas state (such as temperature and pressure) are the main impact factors of the ionization process. Besides the ionization of neutral particle (atoms, molecules, etc.), other atomic physics, such as excitation of neutral particles or ions, three-body recombination of charged particles, charge attachment and de-excitation, also happen simultaneously inside the plasma. Three-body recombination is the inverse process of ionization and lead to losses of free electrons. It depends on the number density of charged particles and the electrons temperature. Thus it is only prominent in dense, low-temperature plasmas.

Once the laser-induced plasma emerges, the laser energy will be absorbed into the plasma through different mechanisms. At relatively low laser intensity, the inverse bremsstrahlung heating [4, 5] (also referred to as collisional heating), absorption of photons by charged particles undergoing collisions, dominates the absorption of laser energy. In dense plasma, where the plasma frequency is higher than the laser field

frequency, the stimulated Compton effects [6] prevails the inverse bremsstrahlung for heating of plasma electrons [7]. In a nonuniform plasma, the ponderomotive effect due to the electron acceleration in the nonuniform electric field from the incident laser beam may be efficient for plasma heating if the nonuniformity of the plasma is sufficiently strong so that the characteristic gradient scale length is shorter than the electron oscillation amplitude [7]. At high laser intensities (above 10^{15} W/cm² or so [8]), the collisions among particles become ineffective [9] and the quiver velocity of electron is comparable to the thermal velocity, which reduces the effective collision frequency further [10]. Instead of collisional heating, some collisionless absorption mechanisms become prominent in this regime of laser intensities. These collisionless mechanisms are based upon the parametric instabilities that are caused by the plasma parameters oscillation with the strong laser field: it is possible for the parameters to become resonant with the field fluctuations just as the case of mechanical vibration systems. As the representative collisionless mechanisms for laser energy absorption, two-plasmon photon decay, stimulated Raman scattering, stimulated Brillouin scattering and plasma resonance are strongly depend upon the plasma nonuniformity. The two-plasmon decay [11, 12] involves the decay of a laser photon into the quantum of a Langmuir plasma wave and an ion acoustic wave. This mechanism is remarkable in sufficiently dense plasmas where the plasma density $n > n_{cr}/4$ where n_{cr} is the critical electron density of the plasma. The stimulated Raman scattering (SRS) [13, 14] usually happens in underdense plasma where $n < n_{cr}/4$. In SRS, the laser energy is absorbed by the plasma Langmuir wave and the transverse electromagnetic field which is shifted in frequency. The stimulated Brillouin scattering (SBS) [15, 16], which is significant for longer laser pulses, absorbs the laser

energy by exciting an ion acoustic wave. If the nonuniformity of the plasma is sufficiently strong, the plasma resonance absorption presents and excites a plasma wave. This plasma wave grows over several laser periods and is eventually damped either by collisions at low intensity area or by particle trapping and wave breaking at high intensity area [15]. If the laser intensity increases further to relativistic regime (usually higher than 10^{18} W/cm²), two more parametric instabilities emerge: laser filamentation [17, 18] and laser modulation [19, 20], both of which are closely related with the electron mass oscillation due to the relativistic effect. Another heating mechanism of electrons exists near the interface between vacuum and plasma, which is called vacuum heating [21, 22]. In this scenario, electrons are dragged away from the plasma surface into the vacuum, turned around and accelerated back into the solid all within half a laser cycle and heated due to the strongly inelastic inverse bremsstrahlung or the ponderomotive scattering [7]. Vacuum heating occurs when a p-polarized laser pulse is obliquely incident on the vacuum-plasma surface while another similar heating mechanism, $\mathbf{j} \times \mathbf{B}$ heating [23, 24], happens when the laser pulse impinges the plasma surface normally. In $\mathbf{j} \times \mathbf{B}$ heating, the electrons oscillating near the interface of vacuum-plasma are forced into the plasma by the magnetic field of the laser beam every half period of the laser.

Besides absorptions of laser pulse energy, the laser pulse propagation inside the plasma is also an important aspect in laser-plasma interactions. A basic phenomenon in this category is the ionization-induced defocusing [25, 26] of the laser beam. When a laser pulse whose center intensity is close or above the ionization potential propagates inside the plasma, more free electrons due to the ionization will appear around the center of the beam, resulting in a steep radial gradient of electron number density. Since the

refractive index of the plasma is dependent on the distribution of electron number density, this radial gradient of electron number density will lead to a smaller refractive index on the propagation axis, acting as a defocusing lens for the following laser beam. However, when the laser intensity is in the relativistic range, the self-focusing mechanism of the laser pulse propagation emerges due to the interplay between relativistic modification of the electron mass and the ponderomotive effect [27]. By considering the relativistic effect, the distribution of refractive index is not only dependent upon the electron number density, but also reliant on the relativistic factor that can be modified by the electron mass. Meanwhile, the electrons at the center position are expelled by the laser ponderomotive force, leading to a reduction of the electron number density on axis. Owing to above two effects, the refractive index of the plasma decreases on axis, acting as a focusing lens for the following portion of the laser beam. Based upon the dynamical equilibrium between the defocusing and the self-focusing [28], a plasma channel can be established in the plasma, through which the laser pulse can propagate a relatively long distance which is significant in many applications.

Generation of fast electrons is a representative physics of plasma responses to the laser-plasma interaction. In the interaction between underdense plasmas and short-pulsed high-intensity lasers, electrons can be heated to a very high temperature during the laser pulse period while the ions, due to their large inertia, remain “cold” at the same time. Thus, a large local charge separation is resulted and the electrons oscillate at the plasma frequency, creating alternating regions of net positive and negative charge. Then a plasma wave wake is generated whose phase velocity is roughly equal to the velocity of the laser pulse, which is approximately equal to the speed of light in the tenuous plasmas. The

plasma wave wake has a longitudinal electric field so that it can efficiently accelerate the charged particles [29], potentially to GeV level [8]. Those highly energetic electrons can lead to a large space charge potential and ions can be accelerated in this electrostatic sheath to MeV level under short-pulse high-intensity laser-plasma interaction [29]. Another direct result of those hot electrons is generation of hard X-rays. A fast electron can penetrate into the cold target due to its long mean free path where it either emits bremsstrahlung via collisions with ions, or produces line radiation by knocking out a bound K-shell electron [8].

1.2 Applications of laser-plasma interaction

Thanks to the robust physics involved in the laser-plasma interaction, there are many applications of laser-induced plasmas and laser-plasma interactions.

In the field of laser material processing, laser-induced breakdown is considered to be the main reason for the high ablation precision of metals and dielectrics by ultrashort lasers [2, 30]. In the application of pulsed laser deposition (PLD) [31, 32], the interactions of incident laser pulses and the resulted plasma plume, such as absorption of the laser energy within the expanding plume, expansion of the plasma plume and evolution of the plasma temperature, have significant effects on the uniformity and quality of the deposited film. In laser welding, the incident laser beam will ionize the target material so that partially ionized plasma is generated in the keyhole and near the top of the workpiece surface. The plasma inside the keyhole, as a good conductive medium, will assist the energy transport from the laser beam to the workpiece [33]. On the other hand, the inhomogeneous distribution of the free electrons in the plasma on the

top surface of the workpiece will affect the propagation of the laser beam, defocusing the beam and leading to undesirable laser energy dissipation.

Laser-plasma interaction is even more important in the context of inertial confinement fusion. In the indirect-drive approach [14], bunch of laser beams heat the inner wall of a gold cavity called holhraum that contains the deuterium-tritium (DT) pellet, creating a superhot plasma which radiates a uniform “bath” of soft X-rays. The X-rays rapidly heat the outer surface of the fuel pellet, causing a high-speed ablation of the surface material and imploding the fuel capsule. Symmetrically compressing the capsule with radiation forms a central hot spot where fusion process could take place. Comparing to the indirect-drive approach, the direct-drive approach [34] uses powerful beams of laser to directly focus on the pellet. The rapid heating caused by the laser “driver” makes the outer layer of the target explode. The remaining portion of the target is driven inwards in a rocket-like implosion, causing compression of the fuel inside the capsule and the formation of a shock wave, which further heats the fuel in the very center and results in a self-sustaining burn. A new ignition scheme, fast ignition [35], has gained more and more interests recently. The main feature of fast ignition is that the compression stage is separated from the ignition phase. Fast ignition uses the same hardware as the direct-drive approach but adds a high-intensity, ultrafast pulsed laser as the “spark” that achieves ignition. The DT target is first compressed to high density by laser beams, and then the short-pulsed laser delivers energy to ignite the compressed core. An advantage of fast ignition is that the density and pressure of the DT target are less than those in indirect- or direct-drive approaches. In addition, much less mass of the DT fuel is used in the fast ignition, resulting in reduced input energy. From the above description of the

three schemes of ignition for ICF, one can conclude that the laser-plasma interaction plays a very important role and deep understanding of the laser-plasma interaction in the context of ICF is highly desired.

Based upon the physics of laser-generated fast electrons and ions as described above, the concepts of laser wakefield accelerator (LWFA) [36] and self-modulated laser wakefield accelerator (SMLWFA) [20, 37] have been studied for the potential realization of table-top particle accelerator. In LWFA, an electron plasma wave is driven resonantly by a short laser pulse whose pulse length is approximately equal to the plasma wave length through the laser ponderomotive force [38, 39]. The electron energy up to 200 MeV has been reported by Malka's group at LOA [40] by using LWFA. SMLWFA is a hybrid scheme which combines the elements of forward stimulated Raman scattering and the concept of LWFA, in which an electromagnetic wave decays into one plasma wave and another forward propagating light wave via the stimulated Raman forward scattering instability. The most impressive results by using this scheme are reported by a group working with the Vulcan laser at RAL, UK [40, 41] with observations of electrons at energies as high as 120MeV.

Laser-plasma interaction can also be used for atomic emission spectroscopy. For example, laser-induced breakdown spectroscopy (LIBS) [42] utilizes a highly energetic laser pulse as the excitation source. By focusing the laser onto a small area at the surface of the specimen, a very small amount of material is ablated. The resulted plasma plume expands and cools within a very small timeframe. At this point the characteristic atomic emission lines of the elements can be observed. The main feature of LIBS is that it can analyze any matter regardless of its physical state, be it solid, liquid or gas, limited only

by the power of the laser as well as the sensitivity and wavelength range of the spectrograph and detector. Another advantage of LIBS is that it is considered essentially a non-destructive or minimally-destructive technique because only a small amount of material is ablated during the LIBS process and there is almost no specimen heating surrounding the ablation site. In addition, since LIBS is purely an optical technique, the remote analysis can be achieved easily, which is especially significant for use in hazardous environments. The drawback of LIBS is that it is subject to variation in the laser spark and resultant plasma which often limits reproducibility. In order to enhance the signal from the plasma emission, double-pulse LIBS [43] was developed. Depending on pulse separation, the second pulse is more or less absorbed by the plasma plume caused by the previous pulse, resulting in a reheating of the laser plasma and leading to signal enhancement.

Another application of laser-plasma interaction can be seen in the field of medical imaging, which is mainly dependent upon the laser-plasma-generated X-rays. The advantages of using laser-plasma X-ray source include the possibility of substantial dose reduction [44], enhancement of image contrast and reduction of unwanted information by using differential imaging with rapid simultaneous exposure [45], and the possibility to place the X-ray source inside the object of investigation [46].

1.3 Numerical Models

Besides experimental studies and theoretical analysis, numerical modeling is also a powerful tool to obtain deep understanding of the laser-plasma interaction physics and to provide guidelines and optimism methods to applications of laser-plasma interactions.

There are mainly two categories of numerical methods for modeling laser-plasma interactions: hydrodynamics models and kinetic based models.

1.3.1 Hydrodynamics models

The common feature of the hydrodynamics models is that the individual particle species of the plasma or the plasma itself is treated as a continuum fluid. The conservations of mass, momentum and energy are described by hydrodynamic equations. The specific formulations of the conservation equations, generation of free electrons and laser energy deposition vary in different models.

Hydrodynamics simulation of laser-plasma interaction are widely applied in the context of laser-driven ICF, providing guidance for the design of hohlraum targets on the ignition facility and detailed understanding of the interaction physics between incident laser beam and the plasma. The very first hydrodynamic model for intense laser interaction with underdense plasma is LASNEX [47] that was developed by the Lawrence Livermore Laboratory in the late of 1980's. LASNEX solves hydrodynamic equations in Lagrangian coordinates which include flux-dependent electron and ion thermal conductivities, radiative transport for the plasma radiation, laser-radiation absorption and some other physical processes [48]. In the past 30 years, many physical packages such as magnetic field and ray trace have been added into the code of LASNEX, making it a powerful simulation tool in many applications [49-51]. Another early stage hydrodynamics model is SAGE [52] which was developed for simulation of thermal self-focusing in laser plasmas. SAGE is a two-dimensional Eulerian code including a self-consistent ray-tracing algorithm for laser beam propagation. Thus, the dependence of self-focusing on the laser wavelength and the laser energy absorption can be simulated

more realistically. This model uses perfect-gas equation of state and a one-temperature fluid assumption. Laser beam diffraction, radiation emission, superthermal-electron generation and magnetic effects are neglected. However, the above assumptions can be well justified if only low-atomic-number targets are considered [52].

In the past decade, motivated by the fast development of the new concepts and designs of the ignition facility for ICF, many new hydrodynamics models emerge, such as HYDRA [53, 54], PONHF2D [55], PF3D [13, 56-58], HARMONHY [59] and PARAX [60-63]. HYDRA can be regarded as the successor of LASNEX for three-dimensional simulation of laser-plasma interaction in the hohlraum. HYDRA is based upon arbitrary Lagrange Eulerian (ALE) hydrodynamics, employing modern monotonic artificial viscosities to stabilize shocks. HYDRA includes a ray tracing package for laser beam propagation and takes into account ponderomotive effects, heavy ion deposition and radiation transport. In addition, local thermodynamics equilibrium (LTE) and non-LTE opacity models are also included in HYDRA. HYDRA has been utilized in design and simulation of laser-driven experiments [64, 65]. In a later simulation [54], a kernel-based nonlocal electron thermal conduction package based upon the model in [66] was installed in HYDRA, enabling the code to handle the effects of long-range electrons. However, there are still some physics missing in HYDRA [53], including the power loss from the beam due to laser power instability, beam steering due to the ponderomotive force and magnetic fields that may affect the electron temperature profile in the low density regions inside the hohlraum.

In order to simulate the time-dependent filamentation and stimulated Brillouin forward scattering in ICF plasmas, Schmitt and Afeyan developed a two-dimensional

code PONHF2D [55]. The laser beam propagation in this model is achieved by a scalar paraxial wave equation which is coupled to the plasma through the dielectric constant. Two different approaches are used to model the plasma response. One is to use a two-dimensional Flux-Corrected-Transport (FCT) algorithm [67] to solve the continuity equations for the plasma density and momentum, assuming a quasineutral one-fluid plasma. The other approach uses a spectral FFT based algorithm to solve the ponderomotive driven ion-acoustic wave (IAW) equation. The PONHF2D model includes background flow and can treat nonlinear plasma behavior. Furthermore, the derivatives of the fluids variables in the direction of the beam propagation are not ignored, which enables correct description of both laser-plasma and plasma-plasma coupling in the time evolution of filamentation. However, this model neglects the effects of thermal filamentation and nonuniform inverse bremsstrahlung heating. The ionization level of the plasma and the plasma temperature are also assumed to be known independently.

In contrast, interplay between strong inverse bremsstrahlung absorption, laser pulse temporal profile and target expansion are included in the model of HARMONHY [59]. A similar three-dimensional model with HARMONHY is PF3D [13], which includes a nonlinear hydrodynamic package as described in [68] coupled with a paraxial solver for the laser propagation. PF3D can describe the (nonlinear) evolution of ponderomotive and thermal filamentation, forward Brillouin scattering, and such phenomena as beam deflection in the presence of transverse flows. Instead of prescribing the plasma parameters (number density, temperature, etc.) as does in PONHF2D, simulation results of plasma variables obtained from other hydrodynamic plasma models are input to PF3D as the initial conditions. For example, the results from SAGE and

HYDRA are used as the initial conditions for the work in [56] and [57], respectively. The significant advantage of PF3D over HARMONHY is its prominent parallel computation performance using message passing.

Another hydrodynamic model that also uses the paraxial wave equation for the laser beam propagation is PARAX [60]. In this model, nonlocal transport effects [66, 69] are included by using the nonlocal Navier-Stokes equations [62]. Although PARAX can describe various physics emerging in the interactions between laser and plasma, the backscattering processes (SRS and SBS), the expansion of the plasma in the parallel direction and a nonlocal transport model that would be valid in the strongly nonlinear regime are still missing. In addition, the present PARAX simulations are implemented with preformed plasmas. It is expected that the plasmas parameters obtained from other plasma models need to be input to PARAX as the initial conditions.

The common feature of PONHF2D, HARMONHY, PF3D and PARAX is that all of them are using a paraxial approximation for the laser beam propagation in the plasma. However, this approximation is invalid near the critical surface of the plasma inside the hohlraum [56]. In order to overcome this problem, a hydrodynamic model called KOLIBRI [70] was developed without the priori of the paraxial approximation. Instead, a scalar model which corresponds to s-polarization in the two-dimensional case is applied for the laser propagation, allowing for SBS in backward and all sideward directions as well as its coupling with filamentation.

The hydrodynamic models are also widely utilized to simulate the laser-produced plasma and the laser-plasma interaction in the field of laser material processing. By assuming that the electrons in the laser-induced plasma in CO₂ laser welding are in the

local thermal equilibrium, Finke *et al.* [71] proposed a one-dimensional steady state model to describe the laser energy deposition into the workpiece. Based upon a steady state one-dimensional Boltzmann equation of the ions, the mass and momentum conservations of the ions and the quasineutral plasma can be established through the first and second moment of the distribution function. Three mechanisms of the energy transfer inside the keyhole: laser energy absorption through inverse bremsstrahlung, generation of free electrons and recombination of charged particles on the wall, are considered in the model and the energy balance equation can be established. A similar model was proposed by Tix and Simon later [72], in which a system of transport equations for all species particles inside the keyhole plasma is setup also based on stationary kinetic equations. Both the convective and conductive transports and inverse bremsstrahlung heating are included in the model. The model assumes cylindrical symmetry and no dependence of the quantities on the direction of the keyhole axis; that is, the simulation was taken on a slice of the keyhole, far enough from the surface. The simulation results suggest that the main part of the plasma (except for the part near the wall) can be considered to be a fully ionized plasma and can be described by the heat conduction. A model describing the process of deep-penetration laser welding was developed by calculating the keyhole profile using a point-by-point energy balance analysis along the wall [73]. The absorption of laser energy by the plasma is described by Beer-Lambert's law where the absorption coefficient is from the dominant inverse bremsstrahlung. The degree of ionization as a function of temperature is described by Saha's equation. In the above three models, no laser beam propagation is considered. However, the laser beam propagation can be largely affected by the plasma. As a consequence, the plasma absorption and the laser

intensity distribution can be altered a lot. In order to deal with this problem, a model proposed in [74] uses the paraxial wave equation to calculate the laser beam propagation through the plasma plume whose properties are pre-set within the calculation. The simulation results indicate that the focusing of the laser beam is strongly deteriorated in the plasma plume due to refraction and absorption. This plasma defocusing is believed the main reason of the so-called “plasma shield” in laser welding. By keeping the treatment of laser beam propagation with the paraxial equation, Kim and Farson [75] proposed a axisymmetric model with compressible Navier-Stokes equations to simulate a CO₂ laser beam impinging on a flat iron surface with helium and argon as the shielding gas. Besides the refraction and absorption in the plasma plume, the effects of the shielding gas and the reflection at the workpiece surface are also included in the simulation. Chen and Wang developed a model [33] with a simplified three-dimensional keyhole model to study both the keyhole plasma and the plasma plume. Radiation and scalar laser energy absorption are included in the governing equations as the source term. But the laser beam propagation is not coupled in their model. Another three-dimensional keyhole model for laser welding was proposed by Ki *et al.* [76, 77]. The main feature of this model is that the evolution of the liquid/vapor interface is consistent with the fluid flow and the heat transfer in the model. The level set method is adopted to incorporate the liquid/vapor interface boundary condition into the Navier-Stokes equation and the energy equation. The ray tracing method is applied with the level set method to take into account the multi-reflection effects inside the keyhole. The laser energy dissipated into the wall is obtained by the energy balance analysis on the wall surface.

Except for the applications in laser welding, the hydrodynamic models are also exploited in the fields of pulsed laser ablation of metals and dielectrics, pulsed laser deposition (PLD) [78-80], and even laser ablation of organic materials [81, 82]. In modeling of UV pulsed laser ablation of metallic targets, an integral model based on the energy balance analysis of the different processes involved in the laser-solid interaction was proposed in [83]. Laser energy absorptions due to inverse bremsstrahlung and photoionization are considered in this model. Moreover, electron-impact excitation and ionization, three-body recombination process, and energy transfer from hot-plasma electrons to the heavy particles are included in the vapor/plasma kinetics. However, no laser propagation is solved in this model. Another hydrodynamics model, MULTI-FS, was developed in [84] to simulate subpicosecond laser interaction with solid density matter. This method is based upon its previous version MULTI [85], which is a one-dimensional, one-fluid, two-temperature model including electronic heat conduction and multigroup radiation transport. Comparing with MULTI, MULTI-FS is improved in the following three aspects: 1) Maxwell's equations are solved by the matrix method on a high resolution mesh whereas a WKB approximation was used in MULTI; 2) electron collision frequency is modeled to include its effects on the collisional absorption of the laser, the energy transfer between electron and ion and the thermal conductivity; 3) SESAME equation of state are used for electron and ion separately. The code of MULTI-FS is validated by several absorption measurement performed with aluminum targets irradiated by a subpicosecond pulsed laser. In order to resolve the multiple timing scales in the laser-induced plasma plume dynamics, a combined one-dimensional Lagrangian – two-dimensional Large Particle Model was developed in [86]. This model consists of two

parts. The first part describes the rapid laser-matter interaction within 4 ns. A one-dimensional Lagrangian hydrodynamic model is used in the first part where the two-temperature approximation is applied. The laser energy absorption is treated by numerically solving the Helmholtz equation coupled with equations of motion. The second part models the two-dimensional plasma plume expansion until several hundreds of nanoseconds with the results from the first part as the initial condition. The Large Particle Method, which includes Euler and Lagrange steps, is used to solve the system of hydrodynamic equations in the second part. The most recent hydrodynamic model for diagnostics of the plasma created on a surface of Ag target irradiated by intense femtosecond laser pulses is proposed in [87]. This is a semiempirical model where the numerical coefficients are chosen so as to ensure the best accordance of the simulation to the experimental measurements. The wave equations are solved for the laser beam propagation and inverse bremsstrahlung heating is included in the hydrodynamic equations as the energy source term.

As for the laser ablation of dielectrics, Jiang and Tsai [88] proposed a semi-hydrodynamic model because, in spite that the electron number density is governed by a Fokker-Plank equation, the temperature equation is still in the hydrodynamic form. Another difference with other hydrodynamic models is that the heating term in this model is Joule heating term. The ablations of barium aluminum borosilicate and fused silica by a 220 fs pulsed laser with different fluences are simulated and the free electron number density, the ablation depth and the reflectivity are obtained as the simulation results. In order to interpret the effects of ionization on the interaction between femtosecond laser and silicon, Li and Ki [89] proposed a model which solves the full Maxwell's equations

by the finite-difference time-domain (FDTD) method. The generation of free electrons is obtained by a local energy balance analysis. The simulation results show that the ionization of silicon by the incident laser beam makes the silicon behave metallicly. The laser energy is absorbed mostly in the thin layer below the target surface and the laser beam propagation is even blocked. A threshold characteristic in the regime of femtosecond laser ablation is clearly seen from the results.

1.3.2 Kinetic Based Models

Although hydrodynamics simulations of laser-plasma interactions have gain great success in many fields, they tend to be invalid at high laser intensities where collisionless and relativistic characterize the laser-plasma interaction. A relevant research indicates that the validity range of laser intensity for hydrodynamic simulations is less than 10^{17} W/cm² [84]. Moreover, even with low laser intensity, hydrodynamic models are still invalid if the Knudsen number of the problem is large, e.g., when a laser-induced plasma plume expands in vacuum [90].

From the first, simplest one-dimensional collisionless model developed in 1950's [91] until today's sophisticated parallelized three-dimensional collisional code, particle-in-cell (PIC) method [92, 93] has become the most popular methodology for plasma modeling, especially in simulating laser-plasma interactions with high laser intensities. The principle of PIC methods is to solve the equations of motion of charged particles in the self-consistent electromagnetic fields that are calculated from the full set of Maxwell's equations. The particles are weighted to the spatial grids so that they have an effective size on the order of the grid, allowing one to model a plasma problem using fewer particles than in an actual experiment. Except for the numerical errors generated by

the discretization of space and time, PIC methods retain the physics to the maximum extent theoretically because there are no physical assumptions (such as continuum approximation) presented. However, due to the limitation of computational expanse and the diversity of physical characteristics for different problems, there are more or less approximations applied on PIC codes in the practical implementations.

Nowadays, the representative PIC codes for laser-plasma interactions include WAKE [94, 95], OOPIC [96-98], QUICKPIC [99], CALDER [100-102], and etc. The algorithm of WAKE consists of three approximations [94]. The first approximation is referred to as ponderomotive guiding center motion of the particles whereas only the low-frequency motion of electrons is retained. However, this approximation breaks if there are self-trapped electrons in the plasma or the axial speed of electron approaches to the speed of light. The quasi-static approximation is the second approximation in WAKE. It assumes that the profile of the laser pulse dose not change significantly during the time of interaction with the electrons. As the third approximation, extended paraxial approximation is applied in WAKE to simulate the laser pulse propagation. Based upon the above three approximations, Chessa *et al.* [94] applied WAKE including a tunneling ionization model to simulate short laser pulse self-focusing in underdense plasma. Besides the tunneling ionization, the impact ionization due to the binary collisions between electrons and neutrals are also included in OOPIC, which is a two-dimensional relativistic object-oriented PIC code [96, 97]. The main feature of OOPIC is that a moving window scheme is adopted because only the small vicinity around the laser pulse in the plasma is of interest. The moving window scheme in which the computational window moves with the laser pulse was firstly adopted in the two-dimensional cylindrical

code of ISIS [103]. In a later work, Decker *et al.* [104] extended this scheme to the two-dimensional Cartesian geometry and simulated forward Raman scattering induced by short pulse high intensity lasers. The above introduced PIC codes have a common drawback: highly computationally expensive even with today's fastest computers [99]. Encouragingly, a newly developed, full parallelized, full three-dimensional PIC code, QUICKPIC [99], can largely save the computational time. The main assumption in QUICKPIC is that there are two distinct time scales for the laser pulse and the plasma evolution. Besides, the ponderomotive guiding center motion of the particles and quasi-static approximations are also included. Simulation of a benchmark problem by QUICKPIC and a conventional PIC code OSIRIS [105] shows that this new code can reduce the computational time by 2-3 orders of magnitude while reproduce satisfactory results. However, the ionization mechanisms are not considered in QUICKPIC. Another representative two- or three-dimensional, parallelized, full relativistic PIC code is CALDER [100], which has been applied to simulate the fast electron energy deposition in fast ignition [102], proton acceleration [101] and laser-accelerated ion beams [106].

As another particle simulation method of plasma, molecular dynamics (MD) models are also proactive in simulation of laser-plasma interactions. Unlike PIC, which is based on particle-mesh (PM) scheme, MD relies on particle-particle (PP) or particle-particle-particle-mesh (P^3M) schemes [93]. Although PM is the most widely applied in particle simulation, the PP is preferred in some special circumstances, for example, in the many-body collisions dominated plasmas. In addition, PP can handle three-dimensional problems just as easily as two-dimensional ones, with insignificant increase in computational expense [107]. However, since solving the individual equation of motion

for each of N particles would require $N^2/2$ individual force calculations to be undertaken every integration time step, the main drawback of PP scheme is apparent: the computational expense is much higher than that of the PIC approach. In order to utilize the advantages of both PM and PP to the greatest extent, most MD codes apply P^3M as the underlying scheme, where the force on a particle is divided into a collective, long-range term from the majority of the particles (PM) and a short range term arising from particles close to the particle of interest [108]. The main feature of MD models is that the collisions between particles are inherently treated as many-body collisions instead of binary collisions in most of PICs. Thus, MD models have been applied to simulate collective collisional phenomena in plasmas, such as inverse bremsstrahlung [108, 109] and interactions between KrF laser pulses and plasma cluster with ionization [107]. Gibbon *et al.* [110] also uses MD to simulate the proton acceleration from laser-irradiated targets in which their calculation is based upon tree algorithm and uses massively parallel computers.

Comparing to PIC and MD, both of which are particle simulation of plasmas, the Boltzmann equation with Fokker-Planck collision term governing the electron (ion) collisions can be directly solved to simulate laser-plasma interactions. The first numerical solution of Fokker-Planck-type Boltzmann equation [111] was obtained in the study of the effects of steep temperature gradients appearing near the critical surface on the electron heat transport, where the Boltzmann equation was solved by an expansion of the distribution function in spherical harmonics. In a later work [112], a one-dimensional Fokker-Planck code, FPI (Fokker-Planck International), was developed and inverse bremsstrahlung and ion motion were included in the model. In the past two decades, FPI

was developed and improved by adding more and more physics into it, such as Coulomb collision, cold ion hydrodynamics, transport for each energy group and self-consistent electric field to ensure the quasi charge neutrality [113, 114]. In a newer version of FPI [115], collisional ionization and excitation, three body recombination and de-excitation, line emission, and the high density effects of continuum lowering and pressure ionization were included. In this code, the electromagnetic wave was calculated by a Helmholtz equation solver while the system of equations was solved by finite difference and time-splitting methods. In order to save the computational expanse, an average ion model [116], which is often used in hydrodynamics code, was adopted in this code. Besides FPI, there are also other codes to solve the Fokker-Planck-type Boltzmann equation. For example, Town *et al.* [117] used their own Fokker-Planck solver to simulate the short-pulsed laser interaction with solid but no ionization mechanism was included. In a subsequent work [118], they added collisional ionization and recombination and also applied the self-consistent average ion model.

Except for the above mentioned kinetic models, there are other approaches to simulate laser-plasma interaction on the kinetic base. For example, a cellular automaton (CA) model was developed to simulate laser-plasma interactions [119]. Although there are many assumptions applied upon that model, such as no ionization and recombination, fixed ion background and quasi-static electrons, the preliminary results show an encouraging potential to apply CA on laser-plasma simulations. In Ref. [90], Itina *et al.* introduced a hybrid model to simulate the laser-induced plasma plume expansion. In the first stage of plume expansion, a one-fluid two-temperature gas dynamics model was used to describe the plume and the Large Particle Method [120] was adapted to solve the

system numerically. When the plume expands into a region where the gas dynamics model becomes invalid due to the steep density gradient and fails to describe the diffusion process, the direct simulation Monte Carlo (DSMC) method [121] was applied. Relativistic Vlasov simulation [122] and propagator of distribution function [7] are other examples to simulate laser-plasma interactions by kinetic based methods.

1.4 Main Content of This Research

In the present research, a new model is proposed to simulate interactions between laser and weakly ionized plasmas. In this model, Boltzmann equation is used to describe the transports of different species of particles in the plasma. The contributions of electron impact ionization and three body recombination are treated as part of the collision terms in the Boltzmann equation. Besides, the elastic collisions between particles are also included by using the Bhatnagar-Gross-Krook (BGK) approximation. The laser beam propagation inside the bulk of the plasma is simulated by solving the full set of Maxwell's equations directly. The Maxwell's equation and the Boltzmann equation are coupled by the external force term and the current density. In addition, energy equations of all particle species in the plasma are derived directly from the Boltzmann equations and are solved by finite volume method. The advantage of this present model over other hydrodynamic models is that less assumption are made so that the physics of laser-plasma interactions can be retained to a great extent, especially for the wave-related phenomena since they are described by the full set of Maxwell's equations here. Comparing to the kinetic based models, this model can be applied in much longer length and time scales with relatively low computational expense.

In Chapter 2, basic theory of lattice Boltzmann method (LBM) with BGK approximation of the collision term is described, including derivation of the lattice Boltzmann equation from the continuous BGK-type Boltzmann equation and the recovery of the macroscopic equations by Chapman-Enskog expansion. As an application example of LBM for incompressible hydrodynamics flow, the two-dimensional driven cavity flow is simulated to show the capabilities of the standard LBM. Different evaluation methods of the external force term are introduced in Chapter 3. Poiseuille flow, Taylor vortex flow and free diffusion problem under a uniform applied external force are simulated to compare the different external forcing models. Based upon the comparison results, one external force model is selected for all the plasma simulations in this research. In this chapter, magnetohydrodynamic (MHD) flows, including Hartmann flow, Orszag-Tang vortex system (both in 2D and 3D) and magnetic reconnection problem, are simulated by a new developed hybrid LBM model, where the induction equation is solved by the finite difference method and it is coupled with the LBM through the external force term. Although the standard LBM are successful in many applications of fluid flow problems, it may produce large simulation errors if the physical properties of fluid are used in the calculation. It gets more deteriorated in plasma simulations. In order to overcome this problem, a rescaling scheme is introduced in Chapter 4 to determine the simulation parameters of LBM. Isothermal weakly ionized helium plasma is simulated by using LBM with the rescaling scheme in this chapter. The new model as well as the rescaling scheme is validated by the simulation results of electrostatic wave in the plasma and electron diffusion problem. In Chapter 5, the LBM model developed in Chapter 4 is extended to simulation of laser interaction with weakly ionized plasma. This model,

which is essentially a thermal LBM model, takes into account for the temperature evolutions of individual species of plasma particles so that the electron impact ionization and its reverse process, three-body recombination, can be included. Preliminary results of interaction between a continuous laser beam and a weakly ionized helium plasma are presented in this chapter. The capabilities, limitations and future work necessary for improvement of the present model are concluded in Chapter 6.

Chapter 2

Lattice Boltzmann Method for Incompressible Hydrodynamics Flows

In recent years, lattice Boltzmann method (LBM) has been widely applied as a successful alternative scheme to simulate fluids flows [123]. Unlike the traditional numerical methods which solve the Navier-Stokes equations for macroscopic variables, LBM is based on kinetic theory and solves the Boltzmann transport equation for the evolution of particle distribution functions. The macroscopic averaged properties which obey the desired macroscopic equations will be obtained from proper moments of the distribution function. LBM first originated from its Boolean counterparts, the lattice gas automata (LGA), but it has been proved that it can be derived directly from the continuous Boltzmann transport equation by discretization in both time and phase space [124, 125], which gives LBM a more rigorous theoretical foundation. In this chapter, some basic theories of LBM for incompressible hydrodynamics flows, including the BGK approximation of the collision term, derivation of lattice Boltzmann equation from the continuous Boltzmann equation and recovery of macroscopic conservation equations by Chapman-Enskog expansion, are introduced. As a simulation example, a 2D driven cavity flow is simulated by the standard D2Q9 LBM to illustrate its capabilities.

2.1 Boltzmann Transport Equation and Its Collision Term

The Boltzmann equation, a nonlinear seven-dimensional (in phase space) partial differential equation, describes the evolution of the phase space distribution functions of different species of particles in various types of gases or gas mixtures, including plasmas.

The continuous Boltzmann transport equation for the particle species of s in the fluid has the following form:

$$\frac{\partial f_s}{\partial t} + \mathbf{v}_s \cdot \nabla_{\mathbf{x}} f_s + \mathbf{a}_s \cdot \nabla_{\mathbf{v}} f_s = Q_s(f, f') \quad (1)$$

where $f_s = f_s(\mathbf{x}, \mathbf{v}_s, t)$ is the single particle distribution function in the phase space, \mathbf{v}_s is the microscopic velocity and \mathbf{a}_s is the acceleration of fluid particles caused by the external force. Based upon the assumption that only binary collisions in the fluid are taken into account [126], the collision term $Q_s(f, f')$ representing the change of rate of the distribution function due to the collisions can be expressed as:

$$Q_s(f, f') = \int_{-\infty}^{\infty} d\mathbf{v}_{s'} \int_0^{4\pi} d\Omega \sigma_{ss'}(\Omega) |\mathbf{v}_s - \mathbf{v}_{s'}| [f(\mathbf{v}'_s) f(\mathbf{v}'_{s'}) - f(\mathbf{v}_s) f(\mathbf{v}_{s'})] \quad (2)$$

where the subscript s and s' represent particle s and particle s' which are involved in the binary collision, the superscript prime stand for the post collision state, Ω is the solid angle in the collision and $\sigma_{ss'}(\Omega)$ is the differential collision cross section of the collision between particle s and particle s' . When $s' = s$, the above formation of collision term describes the self-collisions; otherwise, it represents the cross-collisions between different species of particles in the fluid.

After we obtain the distribution function by solving the Boltzmann equation, the desirable macroscopic quantities can be deduced by proper moments of the distribution function. For example, the number density, macroscopic velocity and thermal energy are given by:

$$n_s = \int_{-\infty}^{\infty} f_s(\mathbf{x}, \mathbf{v}_s, t) d\mathbf{v}_s \quad (3)$$

$$n_s \mathbf{u}_s = \int_{-\infty}^{\infty} \mathbf{v}_s f_s(\mathbf{x}, \mathbf{v}_s, t) d\mathbf{v}_s \quad (4)$$

$$n_s \varepsilon_s = \frac{1}{2} \int_{-\infty}^{\infty} (\mathbf{v}_s - \mathbf{u}_s)^2 f_s(\mathbf{x}, \mathbf{v}_s, t) d\mathbf{v}_s \quad (5)$$

where $\varepsilon_s = \frac{D_0}{2} \frac{k_B T_s}{m_s}$ and D_0 is the degree of freedom of the fluid particle.

Since the Boltzmann equation is essentially a statistical treatment of the microscopic behaviors of the particles inside the gas or plasma, it is more fundamental than Navier-Stokes equation which is based on the assumption that the fluid of interest is continuum macroscopically; unlike Navier-Stokes equation which is only applicable for small Knudsen number (usually less than 0.1), the Boltzmann equation can be applied in a much larger range of Knudsen number [127] and thereby it is especially suitable to describe the complex fluid flows, such as non-ideal fluids, multiphase or multicomponent fluids and those which cannot be described by Navier-Stokes equation accurately and effectively.

Unfortunately, the nature that Boltzmann equation expressed by Eq. (1) with the collision term (Eq. (2)) is an integral-differential equation makes it almost impossible to find analytical or even numerical solutions [126]. An alternative way to evaluate the collision term is provided by the relaxation model among which the BGK model [128] is the most commonly used. In this model it is assumed that a situation initially not in equilibrium reaches a local equilibrium condition exponentially with time, as a result of collisions, within a relaxation time λ_y . The local equilibrium state of the particles is

characterized by a local equilibrium distribution function $f_s^{eq}(\mathbf{x}, \mathbf{v}, t)$ which often takes the form of Maxwell-Boltzmann distribution:

$$f_s^{eq}(\mathbf{x}, \mathbf{v}_s, t) = \frac{n_s}{(2\pi\theta_s^2)^{D/2}} \exp\left[-\frac{(\mathbf{v}_s - \mathbf{u}_s)^2}{2\theta_s^2}\right] \quad (6)$$

where D is the dimension of the space and $\theta_s = \sqrt{k_B T_s / m_s}$ is the sound speed of the fluid particle s with k_B as the Boltzmann constant, T_s as the temperature and m_s as the mass of the fluid particle s . If there is only one type of particle existing in the gas, the collision term can be mathematically expressed as

$$Q_s(f_s, f_s') = -\frac{(f_s - f_s^{eq})}{\lambda_s} \quad (7)$$

Finally, by neglecting the subscript s , the single-particle Boltzmann equation with BGK approximation for the collision term can be written as:

$$\frac{\partial f}{\partial t} + \mathbf{v} \cdot \nabla_{\mathbf{x}} f + \mathbf{a} \cdot \nabla_{\mathbf{v}} f = -\frac{f - f^{eq}}{\lambda} \quad (8)$$

Note that the simplification of collision term by BGK model expressed by Eq. (7) is only valid for short-range elastic collisions. Physically, there are also long-range collisions inside the fluid, such as the Coulomb collision between charged particles in plasmas. By considering that the charged particle encounters a series of consecutive weak (small deflection angle) binary collisions [129], one can derive the Fokker-Planck collision form to describe the long-range collisions from Boltzmann equation. The general form of Fokker-Planck collision term for the charged particle s can be written as [130]:

$$Q_{FP} = -\frac{\partial}{\partial \mathbf{v}} \cdot \left(\left\langle \frac{\Delta \mathbf{v}}{\Delta t} \right\rangle_s f_s \right) + \frac{1}{2} \frac{\partial^2}{\partial \mathbf{v} \partial \mathbf{v}} : \left(\left\langle \frac{\Delta \mathbf{v} \Delta \mathbf{v}}{\Delta t} \right\rangle_s f_s \right) \quad (9)$$

The vector $\langle \Delta \mathbf{v} / \Delta t \rangle_\alpha$ and the tensor $\langle \Delta \mathbf{v} \Delta \mathbf{v} / \Delta t \rangle_\alpha$ describe the dynamical friction and diffusion in velocity space, respectively. They are given by

$$\left\langle \frac{\Delta \mathbf{v}}{\Delta t} \right\rangle_s = \frac{4\pi q_s^4}{m_s^2} \ln \Lambda \frac{\partial}{\partial \mathbf{v}} \sum_{s'} \left(\frac{q_{s'}}{q_s} \right)^2 \frac{m_s + m_{s'}}{m_{s'}} \int \frac{f_{s'}(\mathbf{v}_{s'})}{|\mathbf{v} - \mathbf{v}'|} d\mathbf{v}' \quad (10)$$

$$\left\langle \frac{\Delta \mathbf{v} \Delta \mathbf{v}}{\Delta t} \right\rangle_s = \frac{4\pi q_s^4}{m_s^2} \ln \Lambda \frac{\partial^2}{\partial \mathbf{v} \partial \mathbf{v}} \sum_{s'} \left(\frac{q_{s'}}{q_s} \right)^2 \int f_{s'}(\mathbf{v}_{s'}) |\mathbf{v} - \mathbf{v}'| d\mathbf{v}' \quad (11)$$

where $f_{s'}(\mathbf{v}_{s'}) = f_{s'}(\mathbf{x}, \mathbf{v}_{s'}, t)$ is the distribution function of particle species s' , and q_s and $q_{s'}$ are the charges of particles s and s' , respectively. The summation is over all charged components including particle s itself. Λ is the plasma parameter which is the number of charged particles in the Debye sphere. In practical calculation, many simpler forms of Fokker-Planck equation as well as numerical algorithms are adopted to solve Eq. (9) [131-133].

In weakly ionized plasmas, since the number density of neutral particles is much greater than that of charged particles, the collisions with neutral particles dominates the whole process. Thus we neglect the long-range Coulomb interaction between charged particles in this research and the collision term approximated by BGK model as illustrated in Eq. (7) is applied to evaluate the elastic collisions between charged particle and neutral particle in all simulations of this research.

2.2 From Boltzmann Equation to Lattice Boltzmann Equation

By neglecting the external force term in Eq. (8), the single-particle Boltzmann equation can be rewritten as [125]:

$$\frac{df}{dt} + \frac{f}{\lambda} = \frac{f^{eq}}{\lambda} \quad (12)$$

where $\frac{d}{dt} = \frac{\partial}{\partial t} + \mathbf{v} \cdot \nabla_{\mathbf{x}}$ is the Lagrangian derivative along the microscopic velocity \mathbf{v} and

the equilibrium distribution function f^{eq} takes the form illustrated by Eq. (6). By integrating Eq. (12) over a small time interval Δt , we can get:

$$f(\mathbf{x} + \mathbf{v}\Delta t, \mathbf{v}, t + \Delta t) = \frac{e^{-\Delta t/\lambda}}{\lambda} \int_0^{\Delta t} e^{s/\lambda} f^{eq}(\mathbf{x} + \mathbf{v}s, \mathbf{v}, t + s) ds + e^{-\Delta t/\lambda} f(\mathbf{x}, \mathbf{v}, t) \quad (13)$$

where $0 \leq s \leq \Delta t$. Assuming that the time step Δt is sufficiently small and f^{eq} is smooth enough locally, $f^{eq}(\mathbf{x} + \mathbf{v}s, \mathbf{v}, t + s)$ can be expanded by Taylor expansion with neglecting the term of order $O(\Delta t^2)$:

$$f^{eq}(\mathbf{x} + \mathbf{v}s, \mathbf{v}, t + s) = \frac{s}{\Delta t} f^{eq}(\mathbf{x} + \mathbf{v}\Delta t, \mathbf{v}, t + \Delta t) + \left(1 - \frac{s}{\Delta t}\right) f^{eq}(\mathbf{x}, \mathbf{v}, t) \quad (14)$$

Substituting Eq. (14) into Eq. (13) and after some manipulations, we can get:

$$\begin{aligned} f(\mathbf{x} + \mathbf{v}\Delta t, \mathbf{v}, t + \Delta t) - f(\mathbf{x}, \mathbf{v}, t) &= (e^{-\Delta t/\lambda} - 1)[f(\mathbf{x}, \mathbf{v}, t) - f^{eq}(\mathbf{x}, \mathbf{v}, t)] \\ &+ \left(1 - \frac{\lambda}{\Delta t} + \frac{\lambda}{\Delta t} e^{-\Delta t/\lambda}\right)[f^{eq}(\mathbf{x} + \mathbf{v}\Delta t, \mathbf{v}, t + \Delta t) - f^{eq}(\mathbf{x}, \mathbf{v}, t)] \end{aligned} \quad (15)$$

Again, expanding $e^{-\Delta t/\lambda}$ in its Taylor expansion and neglecting the terms of order $O(\Delta t^2)$, we obtain the Boltzmann equation discretized in time as:

$$f(\mathbf{x} + \mathbf{v}\Delta t, \mathbf{v}, t + \Delta t) - f(\mathbf{x}, \mathbf{v}, t) = -\frac{\Delta t}{\tau} [f(\mathbf{x}, \mathbf{v}, t) - f^{eq}(\mathbf{x}, \mathbf{v}, t)] \quad (16)$$

where $\tau = \lambda/\Delta t$ is the dimensionless relaxation time. Note that Eq. (16) has first order accuracy in time [125].

Eq. (16) is still continuous in the phase space and $\mathbf{v} \in (-\infty, +\infty)$ for 2D problems. As illustrated in Eqs. (3) to (5), the hydrodynamics variables are proper moments of the distribution function $f(\mathbf{x}, \mathbf{v}, t)$ (or equilibrium distribution function $f^{eq}(\mathbf{x}, \mathbf{v}, t)$) with respect to the microscopic velocity. This can be generalized as:

$$\phi(\mathbf{x}, t) = \int_{-\infty}^{\infty} f(\mathbf{x}, \mathbf{v}, t) \chi(\mathbf{v}) d\mathbf{v} = \int_{-\infty}^{\infty} f^{eq}(\mathbf{x}, \mathbf{v}, t) \chi(\mathbf{v}) d\mathbf{v} \quad (17)$$

where $\phi(\mathbf{x}, t)$ is the hydrodynamics variable, which is dependent upon both position and time, and $\chi(\mathbf{v})$ is a function of the microscopic velocity \mathbf{v} . Assuming that the temperature is constant and the macroscopic velocity of the particle is small (low Mach number approximation), the equilibrium distribution function can be expanded with Taylor series up to the order of $(\mathbf{u} \cdot \mathbf{u})$ [124, 125]:

$$f^{eq} = \frac{n}{(2\pi\theta^2)^{D/2}} \exp\left(-\frac{\mathbf{v}^2}{2\theta^2}\right) \left[1 + \frac{(\mathbf{v} \cdot \mathbf{u})}{\theta^2} + \frac{(\mathbf{v} \cdot \mathbf{u})^2}{2\theta^4} - \frac{\mathbf{u}^2}{2\theta^2} \right] \quad (18)$$

Substituting Eq.(18) into Eq. (17), $\phi(\mathbf{x}, t)$ can be expressed as:

$$\phi(\mathbf{x}, t) = \int_{-\infty}^{\infty} \exp\left(-\frac{\mathbf{v}^2}{2\theta^2}\right) \psi(\mathbf{v}^m) d\mathbf{v} \quad (19)$$

where $\psi(\mathbf{v}^m)$ is a m-th order polynomial of \mathbf{v} . The integration in Eq. (19) has the structure of e^{-x^2} and the integration limitation is from ∞ to $-\infty$. Enlightened by the above observation, it is intuitive to apply Hermite quadrature to find the value of Eq. (19) exactly to the order of m:

$$\phi(x, t) = \sum_{\alpha} W_{\alpha} \exp\left(-\frac{\mathbf{e}_{\alpha}^2}{2\theta^2}\right) \psi(\mathbf{e}_{\alpha}^m) \quad (20)$$

where W_{α} and \mathbf{e}_{α} are the weights and abscissas (or discrete velocities) of m-th order Hermite polynomial, respectively. Then the hydrodynamics variables can be computed by the quadrature as well:

$$n = \sum_{\alpha} f_{\alpha} \quad (21)$$

$$n\mathbf{u} = \sum_{\alpha} \mathbf{e}_{\alpha} f_{\alpha} \quad (22)$$

$$n\varepsilon = \frac{1}{2} \sum_{\alpha} (\mathbf{e}_{\alpha} - \mathbf{u})^2 f_{\alpha} \quad (23)$$

According to the dimensions of the physical problem (1D, 2D or 3D) and the number of macroscopic variables desired, different number of abscissas of the Hermite polynomial may be needed, and accordingly, resulting in different sets of discrete velocities. For example, the D2Q9 discrete velocity model may be applied for 2D isothermal problems. To derive this nine-bit lattice Boltzmann equation, a Cartesian coordinate system is used and $\psi(\mathbf{v}^m)$ is set as $\psi(\mathbf{v}^m) = v_x^m v_y^n$, where $1 \leq n \leq m$. Then Eq. (19) can be rewritten as:

$$\phi(x, t) = (\sqrt{2}\theta)^{m+n+2} I_m I_n \quad (24)$$

where

$$I_m = \int_{-\infty}^{\infty} e^{-\zeta^2} \zeta^m d\zeta \quad (25)$$

and $\zeta = v_x/\sqrt{2}\theta$ or $\zeta = v_y/\sqrt{2}\theta$. In the derivation of the nine-bit model in 2D, it is natural to use the third order Hermite quadrature to evaluate Eq. (25); that is,

$I_m = \sum_{j=1}^3 \omega_j \zeta_j^m$, where the three abscissas and the corresponding three weights are:

$$\begin{aligned} \zeta_1 &= -\sqrt{3/2}, & \zeta_2 &= 0, & \zeta_3 &= \sqrt{3/2} \\ \omega_1 &= \sqrt{\pi}/6, & \omega_2 &= 2\sqrt{\pi}/3, & \omega_3 &= \sqrt{\pi}/6 \end{aligned} \quad (26)$$

Then Eq. (24) becomes:

$$\phi(\mathbf{x}, t) = 2\theta^2 \omega_2^2 \psi(\mathbf{0}) + \sum_{\alpha=1}^4 \omega_1 \omega_2 \psi(\mathbf{e}_\alpha) + \sum_{\alpha=5}^8 \omega_1^2 \psi(\mathbf{e}_\alpha) \quad (27)$$

where the discrete velocities \mathbf{e}_α are:

$$\mathbf{e}_\alpha = \begin{cases} (0, 0) & \alpha = 0 \\ (\cos \varphi_\alpha, \sin \varphi_\alpha) c & \alpha = 1, 2, 3, 4 \\ (\cos \varphi_\alpha, \sin \varphi_\alpha) \sqrt{2} c & \alpha = 5, 6, 7, 8 \end{cases} \quad (28)$$

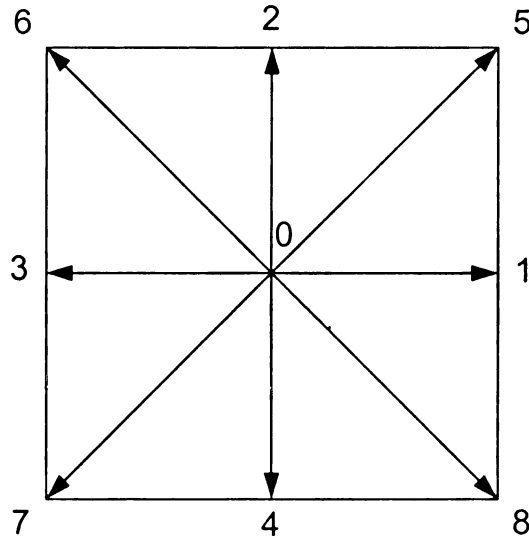


Figure 1 Schematic of D2Q9 square lattice. The two-dimensional continuous phase space is discretized by nine microscopic velocity components in a square lattice.

with

$$\begin{cases} \varphi_\alpha = (\alpha - 1)\pi/2 & \alpha = 1, 2, 3, 4 \\ \varphi_\alpha = (\alpha - 5)\pi/2 + \pi/4 & \alpha = 5, 6, 7, 8 \end{cases} \quad (29)$$

where $c = \sqrt{3}\theta$ is the lattice speed and is defined as $c \equiv \Delta x / \Delta t$. The schematic of the discrete velocities is shown in Figure 1.

Comparing Eq. (20) and Eq. (27), the weights W_α in Eq. (20) can be found as:

$$W_\alpha = 2\pi\theta^2 \exp\left(\frac{\mathbf{e}_\alpha^2}{2\theta^2}\right) \omega_\alpha \quad (30)$$

where

$$\omega_\alpha = \begin{cases} 4/9 & \alpha = 0 \\ 1/9 & \alpha = 1, 2, 3, 4 \\ 1/36 & \alpha = 5, 6, 7, 8 \end{cases} \quad (31)$$

Then the discretized equilibrium distribution function is:

$$f_\alpha^{eq} = W_\alpha f^{eq}(\mathbf{x}, \mathbf{e}_\alpha, t) = \omega_\alpha n \left\{ 1 + \frac{3(\mathbf{e}_\alpha \cdot \mathbf{u})}{c^2} + \frac{9(\mathbf{e}_\alpha \cdot \mathbf{u})^2}{2c^4} - \frac{3\mathbf{u}^2}{2c^2} \right\} \quad (32)$$

Note that in the above derivation, the phase space and the configuration space are discretized simultaneously through the relationship between the lattice speed and the spacing. Finally, the discretized Boltzmann equation, or lattice Boltzmann equation, takes the following form:

$$f(\mathbf{x} + \mathbf{e}_\alpha \Delta t, t + \Delta t) = f(\mathbf{x}, t) - \frac{f(\mathbf{x}, t) - f_\alpha^{eq}(\mathbf{x}, t)}{\tau} \quad (33)$$

In the practical implementation of standard LBM, there are always two steps involved: collision step and streaming step. In the collision step, the fluid particles collide with each other on the local node point to finish the momentum exchange and energy

exchange (if it exists in the physical problem). The particles then stream to the neighboring nodes along the directions of the discretized velocity vectors in the streaming step. These two steps can be illustrated mathematically by:

Collision step:

$$\tilde{f}_\alpha(\mathbf{x}, t) = f_\alpha(\mathbf{x}, t) - \frac{f_\alpha(\mathbf{x}, t) - f_\alpha^{eq}(\mathbf{x}, t)}{\tau} \quad (34)$$

Streaming step:

$$f_\alpha(\mathbf{x} + \mathbf{e}_\alpha \Delta t, t + \Delta t) = \tilde{f}_\alpha(\mathbf{x}, t) \quad (35)$$

where $\tilde{f}_\alpha(\mathbf{x}, t)$ represents the post-collision distribution function along the direction α . From Eqs. (34) and (35), we can see that the collision step is purely local and the streaming step is a uniform data shifting and only demands little computational effort. The two-step scheme is explicit, easy to implement and straightforward for parallel computation.

2.3 From Lattice Boltzmann Equation to Navier-Stokes Equation

The desired macroscopic conservation equations, such as the Navier-Stokes equation, can be recovered by the Chapman-Enskog expansion of the lattice Boltzmann equation as shown in Eq. (33). The significance of this derivation lies on the fact that some fluid properties, such as the kinematic viscosity, can be retrieved from this derivation.

Introduce the following multiscale expansions to the α -component distribution function and the time derivative:

$$f_\alpha = f_\alpha^{(0)} + \varepsilon f_\alpha^{(1)} + \varepsilon^2 f_\alpha^{(2)} + \dots = \sum_{n=0}^{\infty} \varepsilon^n f_\alpha^{(n)} \quad (36)$$

$$\frac{\partial}{\partial t} = \frac{\partial}{\partial t_0} + \varepsilon \frac{\partial}{\partial t_1} + \varepsilon^2 \frac{\partial}{\partial t_2} + \dots = \sum_{n=0}^{\infty} \varepsilon^n \frac{\partial}{\partial t_n} \quad (37)$$

where ε is the time step Δt .

By taking the Taylor expansion to $f_\alpha(\mathbf{x} + \mathbf{e}_\alpha \Delta t, t + \Delta t)$, we can have

$$f_\alpha(\mathbf{x} + \mathbf{e}_\alpha \Delta t, t + \Delta t) = f_\alpha(\mathbf{x}, t) + D_{t_1} f_\alpha(\mathbf{x}, t) + D_{t_1}^2 f_\alpha(\mathbf{x}, t) + O(\Delta t^3) \quad (38)$$

where $D_{t_1} = \frac{\partial}{\partial t} + \mathbf{e}_\alpha \cdot \nabla$. Substituting Eqs. (36), (37) and (38) into Eq. (33) and sorting the

resulted equation by the order of ε , we can get:

$O(\varepsilon^0)$:

$$f_\alpha^{(0)} = f_\alpha^{eq} \quad (39)$$

$O(\varepsilon^1)$:

$$D_{t_0} f_\alpha^{(0)} = -\frac{1}{\tau} f_\alpha^{(1)} \quad (40)$$

$O(\varepsilon^2)$:

$$\frac{\partial f_\alpha^{(0)}}{\partial t_1} + \frac{(2\tau - 1)}{2\tau} D_{t_0} f_\alpha^{(1)} = -\frac{1}{\tau} f_\alpha^{(2)} \quad (41)$$

where $D_{t_n} \equiv (\frac{\partial}{\partial t_n} + \mathbf{e}_\alpha \cdot \nabla)$. The distribution function in the above expansion is

constrained by:

$$\begin{aligned} \sum_{\alpha} f_\alpha^{(0)} \begin{bmatrix} 1 \\ \mathbf{e}_\alpha \end{bmatrix} &= \begin{bmatrix} n \\ n\mathbf{u} \end{bmatrix} \\ \sum_{\alpha} f_\alpha^{(n)} \begin{bmatrix} 1 \\ \mathbf{e}_\alpha \end{bmatrix} &= 0 \quad n > 0 \end{aligned} \quad (42)$$

Taking the zeroth and first order moments of Eq. (40), we get:

$$\frac{\hat{c}n}{\hat{c}t_0} + \nabla \cdot (n\mathbf{u}) = 0 \quad (43)$$

and

$$\frac{\hat{c}(n\mathbf{u})}{\hat{c}t_0} + \frac{1}{m} \nabla \cdot \mathbf{\Pi}^{(0)} = 0 \quad (44)$$

where $\mathbf{\Pi}^{(0)} = m \sum_{\alpha} \mathbf{e}_{\alpha} \mathbf{e}_{\alpha} f_{\alpha}^{(0)}$ is the zeroth order momentum flux dyad and

$\mathbf{\Pi}^{(0)} = mn(\theta^2 \mathbf{I} + \mathbf{u}\mathbf{u})$ according to the kinetic theory. Similarly, by taking the zeroth and first order moments of Eq. (41), we can get:

$$\frac{\hat{c}n}{\hat{c}t_1} = 0 \quad (45)$$

and

$$\frac{\hat{c}(n\mathbf{u})}{\hat{c}t_1} + \frac{(2\tau - 1)}{2\tau} \frac{1}{m} \nabla \cdot \mathbf{\Pi}^{(1)} = 0 \quad (46)$$

where $\mathbf{\Pi}^{(1)} = m \sum_{\alpha} \mathbf{e}_{\alpha} \mathbf{e}_{\alpha} f_{\alpha}^{(1)}$ is the first order momentum flux dyad. From Eq. (40), we

have $\mathbf{\Pi}^{(1)} = -\tau \sum_{\alpha} \mathbf{e}_{\alpha} \mathbf{e}_{\alpha} D_{t_0} f_{\alpha}^{(0)} = -\tau \left[\frac{\hat{c}\mathbf{\Pi}^{(0)}}{\hat{c}t_0} + \nabla \cdot \mathbf{e}_{\alpha} \mathbf{e}_{\alpha} f_{\alpha}^{(0)} \right]$, where the second term

on the right hand side reads $\nabla \cdot \mathbf{e}_{\alpha} \mathbf{e}_{\alpha} f_{\alpha}^{(0)} = mn\theta^2 [(\nabla \cdot \mathbf{u})\mathbf{I} + 2\nabla\mathbf{u}]$ [134]. By neglecting

the terms greater than the order of $O(\mathbf{u}^2)$ [134], we can get:

$$\frac{(2\tau - 1)}{2\tau} \nabla \cdot \mathbf{\Pi}^{(1)} = -\frac{(2\tau - 1)}{2} mn\theta^2 \nabla^2 \mathbf{u} \quad (47)$$

Letting the kinematic viscosity ν :

$$\nu = (\tau - 0.5)\theta^2 \Delta t \quad (48)$$

Eq. (46) can be rewritten as:

$$\frac{\hat{c}(n\mathbf{u})}{\hat{c}t_1} - \frac{\nu}{\Delta t} n \nabla^2 \mathbf{u} = 0 \quad (49)$$

Recalling that $\frac{\partial}{\partial t} = \frac{\partial}{\partial t_0} + \Delta t \frac{\partial}{\partial t_1}$ (as shown in Eq. (37) and truncated at the order of

$O(\Delta t^2)$) and using Eqs. (43), (44), (45) and (49), we can finally recover the continuity equation and the Navier-Stokes equation from the lattice Boltzmann equation (Eq. (33)) as:

Continuity equation:

$$\frac{\partial n}{\partial t} + \nabla \cdot (n\mathbf{u}) = 0 \quad (50)$$

Navier-Stokes equation:

$$\frac{\hat{c}(n\mathbf{u})}{\hat{c}t} + \nabla \cdot (n\mathbf{u}\mathbf{u}) = -\frac{1}{m} \nabla p + \nu n \nabla^2 \mathbf{u} \quad (51)$$

where $p = nk_B T$ is the scalar pressure.

From the above derivation, we can see that there is a modification of the fluid viscosity by 0.5 as illustrated in Eq. (48), which leads that the viscosity is not only dependent on the physics but also dependent on the lattice. This means that if the physical properties of fluid are used in the simulation, the resulted viscosity may not be equal to the physical one. This problem can be solved by using a rescaling scheme developed in this research. It will be explained in details in Chapter 4.

2.4 LBM Simulation of Two-dimensional Driven Cavity Flow

In order to illustrate the capability of the standard D2Q9 LBM as described above, a 2D incompressible driven cavity flow is simulated on a uniform 256×256 square grid

system. The driven cavity flow which is bounded by a square enclosure and driven by a uniform outer flow on the top shows rich vortex phenomena at many scales depending on the Reynolds number [135-137]. In this simulation, the no-slip conditions are applied at the left, right and bottom walls; that is, the macroscopic velocities at the boundary node points on the wall are equal to zero. Viewing from the microscopic point, the distribution functions just reverse their direction but keep their values on the wall. For the top boundary, since the outer flow remains unchanged physically, the equilibrium values with the outer flow speed u_x are set to the top nodes as the updated distribution function after each streaming step in the calculation. The simulation parameters are set as: $\Delta x = 1$, $\Delta t = 1$ and $\rho_0 = 1.0$. The driven velocity on the top of the cavity is $u_x = 0.1$ and the Reynolds number is defined as $Re = \frac{3u_x N_x}{(\tau - 0.5)}$ where N_x is the grid number along the top boundary and the viscosity used here is calculated from Eq. (48).

Figure 2 shows the streamlines of the cavity flow at different Reynolds numbers. The dependence of the vortex on the Reynolds number can be seen very clearly from the figure. Figure 3 illustrates the x- and y-component velocities through the geometric center of the cavity. Their patterns agree with those in the literatures very well. The detailed quantitative comparison with results in the literatures will be presented in Chapter 4.

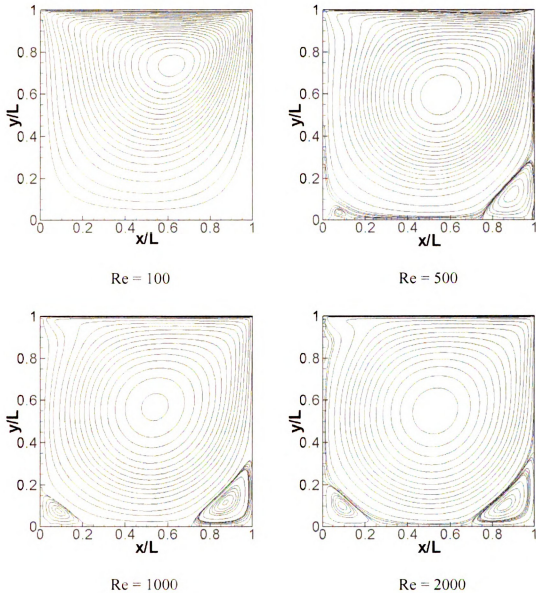
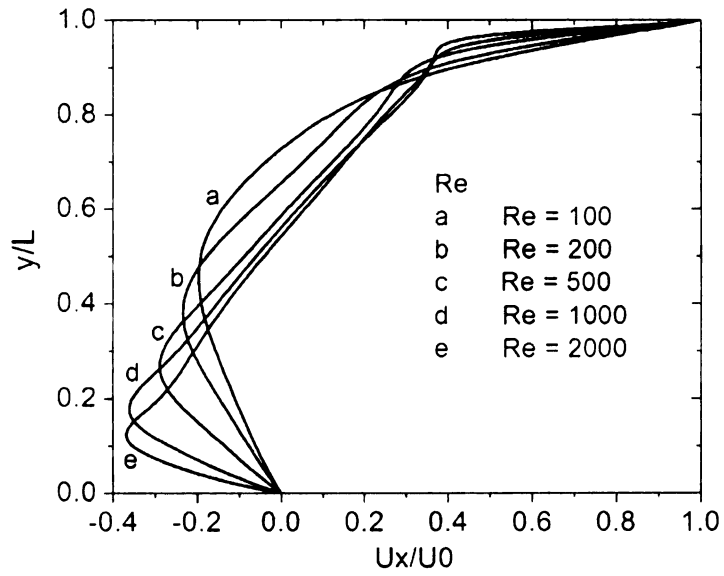
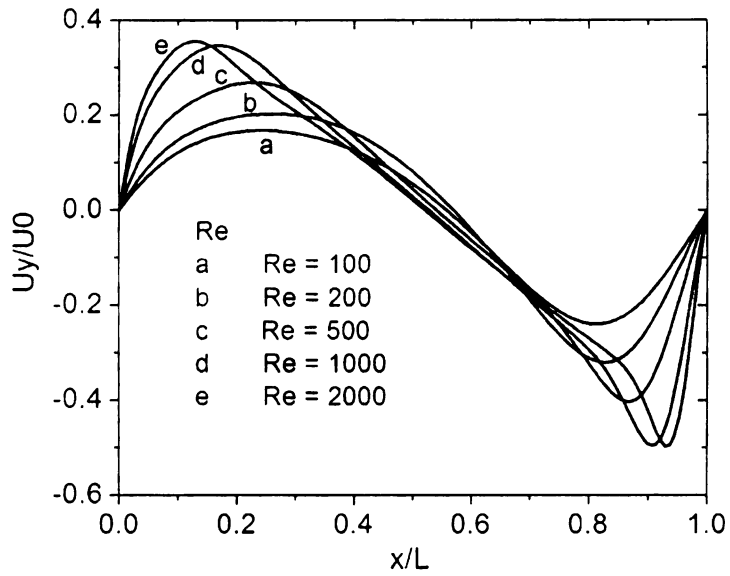


Figure 2 Streamlines of driven cavity flow with different Reynolds numbers. The flow pattern is strongly dependent on the Reynolds number. If the Reynolds number is sufficiently large, secondary vortices appear at the right and left lower corners.



(a)



(b)

Figure 3 Velocity profiles through the geometric center of the cavity (a) Profiles of x-component velocity; (b) Profiles of y-component velocity

Chapter 3

Evaluation of the External Force Term in Lattice Boltzmann Method

In the simulation of the driven cavity flow presented in the previous chapter, no external force exerts on the fluid particles. Accordingly, the lattice Boltzmann equation takes the form illustrated by Eq. (33). But in most practical cases, especially in the simulation of plasmas, there are always various types of external forces acting on the particles, affecting the rates of change of momentum and energy. It is very important to evaluate the external force term in the lattice Boltzmann equation accurately. However, the external force term $\mathbf{a} \cdot \nabla_{\mathbf{v}} f$ in the Boltzmann equation cannot be calculated directly because the dependence of the distribution function on the microscopic velocity \mathbf{v} is unknown. Thus, it is necessary to develop alternative methods to evaluate the external force term in the Boltzmann equation. In this chapter, five different external forcing models are compared through simulations of Poiseuille flow, Taylor vortex flow and free diffusion problem under a uniform externally applied force. Based upon the comparisons, He's model is selected to evaluate the external force term in this research. By using He's model, a new hybrid LBM model is developed to simulate magnetohydrodynamics (MHD) flows. This model is validated by Hartmann flow, Orszag-Tang vortex system and magnetic reconnection problem in this chapter.

3.1 Different External Force Models

The lattice Boltzmann equation with presence of an external force term can be written as [138]:

$$f_\alpha(\mathbf{x} + \mathbf{e}_\alpha \Delta t, t + \Delta t) = f_\alpha(\mathbf{x}, t) - \frac{f_\alpha(\mathbf{x}, t) - f_\alpha^{eq}(\mathbf{x}, t)}{\tau} + \Delta t F_\alpha \quad (52)$$

where F_α is the discretized external force term along the α -th direction of the discrete velocity vector. The corresponding equilibrium distribution function in Eq. (52) is defined as (in D2Q9 scheme):

$$f_\alpha^{eq} = \omega_\alpha n \left\{ 1 + \frac{3(\mathbf{e}_\alpha \cdot \mathbf{u}^*)}{c^2} + \frac{9(\mathbf{e}_\alpha \cdot \mathbf{u}^*)^2}{2c^4} - \frac{3\mathbf{u}^{*2}}{2c^2} \right\} \quad (53)$$

where \mathbf{u}^* is called the equilibrium velocity. Different formations of F_α and \mathbf{u}^* lead to different treatments of the external force term in the lattice Boltzmann equation.

The very first and simplest external force model was developed by He *et al.* [139] and is referred as to Method 1 in this research. In this model, the external force term F_α

takes the form as $F_\alpha = \frac{\omega_\alpha n \mathbf{e}_\alpha \cdot \mathbf{a}}{\rho^2}$ where \mathbf{a} is the acceleration of the fluid particle due to

the external force. The equilibrium velocity \mathbf{u}^* is equal to the fluid macroscopic velocity

\mathbf{u} ; that is, $\mathbf{u}^* = \mathbf{u} = \frac{1}{n} \sum_\alpha \mathbf{e}_\alpha f_\alpha$. This method is suitable for the case where the spatial and

temporal gradient of the external force is negligible. Thus, it is always applied for the flows under a constant body force, such as constant pressure gradient or gravity.

The second method to evaluate the external force term (which is referred as to Method 2 here) was originally developed to simulate nonideal fluids by the LBM [140-142]. It was originated independent by two groups within the frame of Hermite expansion, which is consistent with the derivation of the lattice Boltzmann equation, and with some constraints of different order moments. In this model, the external force term is written as

$F_\alpha = \omega_\alpha n \mathbf{a} \cdot \left[\frac{(\mathbf{e}_\alpha - \mathbf{u}^*)}{\theta^2} + \frac{(\mathbf{e}_\alpha \cdot \mathbf{u}^*) \mathbf{e}_\alpha}{\theta^4} \right]$ and the equilibrium velocity has the same

definition as the fluid macroscopic velocity, i.e. $\mathbf{u}^* = \mathbf{u} = \frac{1}{n} \sum_\alpha \mathbf{e}_\alpha f_\alpha$. In this model, the

contribution of the external force to the momentum flux is considered. But like Method 1, it is still only applicable for the case where the spatial and temporal gradient of the external force is sufficiently small. In a later research [143], this model is updated by

defining the fluid macroscopic velocity as $\mathbf{u} = \frac{1}{n} \sum_\alpha \mathbf{e}_\alpha f_\alpha + \frac{1}{2} \Delta t \mathbf{a}$ while the equilibrium

velocity keeps the same definition as before. This approach eliminates the temporal gradient constraint of the external force, but still cannot be applicable for the large spatially varying external force. This updated version of Method 2 was applied by Breyiannis and Valougeorgis [144] in a recent research to simulate 3D magnetohydrodynamics flows where the magnetic force $\mathbf{J} \times \mathbf{B}$ is treated as the external force.

Method 3 was proposed by Buick and Greated [145]. The external force term in their model is $F_\alpha = \left(1 - \frac{1}{2\tau}\right) \frac{\omega_\alpha n}{\theta^2} (\mathbf{e}_\alpha \cdot \mathbf{a})$. The equilibrium velocity and the fluid

macroscopic velocity have the definition as $\mathbf{u}^* = \mathbf{u} = \frac{1}{n} \sum_\alpha \mathbf{e}_\alpha f_\alpha + \frac{1}{2} \Delta t \mathbf{a}$. In a later

research, Guo *et al.* developed a model (which is referred as Guo's model) where the

external force term is defined as $F_\alpha = \left(1 - \frac{1}{2\tau}\right) \omega_\alpha n \mathbf{a} \cdot \left[\frac{(\mathbf{e}_\alpha - \mathbf{u}^*)}{\theta^2} + \frac{(\mathbf{e}_\alpha \cdot \mathbf{u}^*) \mathbf{e}_\alpha}{\theta^4} \right]$ and both

the equilibrium velocity and the fluid velocity have the same definition as Method 3.

The most popular external force model was developed by He *et al.* [146] (which is referred as to He's model here) and it has been widely adopted in many researches [147-149]. This model is based upon the fact that f^{eq} is the leading part of the expansion of the distribution function and the gradient of f^{eq} has the most important contribution to the gradient of f . Then the external force term can be written as:

$$\mathbf{a} \cdot \nabla_{\mathbf{v}} f \approx \mathbf{a} \cdot \nabla_{\mathbf{v}} f^{eq} = -\frac{\mathbf{a} \cdot (\mathbf{v} - \mathbf{u})}{\theta^2} f^{eq} \quad (54)$$

Accordingly, the Boltzmann equation with the external force term becomes:

$$\frac{\partial f}{\partial t} + \mathbf{v} \cdot \nabla_{\mathbf{x}} f = -\frac{f - f^{eq}}{\lambda} + \frac{\mathbf{a} \cdot (\mathbf{v} - \mathbf{u})}{\theta^2} f^{eq} \quad (55)$$

By following the similar discretization approach illustrated in Chapter 2, the lattice Boltzmann equation reads:

$$f_{\alpha}(\mathbf{x} + \mathbf{e}_{\alpha} \Delta t, t + \Delta t) = f_{\alpha}(\mathbf{x}, t) - \frac{f_{\alpha}(\mathbf{x}, t) - f_{\alpha}^{eq}(\mathbf{x}, t)}{\tau} + \frac{\Delta t \mathbf{a} \cdot (\mathbf{e}_{\alpha} - \mathbf{u})}{\theta^2} f_{\alpha}^{eq}(\mathbf{x}, t) \quad (56)$$

Note that the assumption that the momentum of fluid particles conserves at each collision [150-152] has been applied in derivation of the above equation.

In summary, Table 1 lists the external force term F_{α} and the equilibrium velocity \mathbf{u}^* in different models. The fluid macroscopic velocity \mathbf{u} has the same form as the equilibrium velocity in all the five models and thus has not been listed in the table.

In order to select an accurate external force model for simulation of plasmas, the above described five models have been applied to simulate the same physical problems and the results are compared. In all the simulations, the external force term takes the form listed in Table 1. The discretized equilibrium distribution function follows Eq. (53) where

the equilibrium velocity is evaluated according to the form shown in Table 1. Correspondingly, the lattice Boltzmann equation shown in Eq. (52) is used.

Model	F_α	\mathbf{u}^*
Method 1	$\frac{\omega_\alpha n \mathbf{e}_\alpha \cdot \mathbf{a}}{\theta^2}$	$\frac{1}{n} \sum_\alpha \mathbf{e}_\alpha f_\alpha$
Method 2	$\omega_\alpha n \mathbf{a} \cdot \left[\frac{(\mathbf{e}_\alpha - \mathbf{u}^*)}{\theta^2} + \frac{(\mathbf{e}_\alpha \cdot \mathbf{u}^*) \mathbf{e}_\alpha}{\theta^4} \right]$	$\frac{1}{n} \sum_\alpha \mathbf{e}_\alpha f_\alpha$
Method 3	$\left(1 - \frac{1}{2\tau}\right) \frac{\omega_\alpha n}{\theta^2} (\mathbf{e}_\alpha \cdot \mathbf{a})$	$\frac{1}{n} \sum_\alpha \mathbf{e}_\alpha f_\alpha + \frac{1}{2} \Delta t \mathbf{a}$
Guo's Model	$\left(1 - \frac{1}{2\tau}\right) \omega_\alpha n \mathbf{a} \cdot \left[\frac{(\mathbf{e}_\alpha - \mathbf{u}^*)}{\theta^2} + \frac{(\mathbf{e}_\alpha \cdot \mathbf{u}^*) \mathbf{e}_\alpha}{\theta^4} \right]$	$\frac{1}{n} \sum_\alpha \mathbf{e}_\alpha f_\alpha + \frac{1}{2} \Delta t \mathbf{a}$
He's Model	$\frac{\mathbf{a} \cdot (\mathbf{e}_\alpha - \mathbf{u})}{\theta^2} f_\alpha^{eq}(\mathbf{x}, t)$	$\frac{1}{n} \sum_\alpha \mathbf{e}_\alpha f_\alpha$

Table 1 F_α and \mathbf{u}^* in different external force models

The first simulation example is the Poiseuille flow between two parallel placed plates which are located at $y = 0$ and $y = 2H$ respectively. The analytical solution of the fluid velocity is:

$$\mathbf{u}^A = \left[\frac{g}{\rho\nu} y \left(H - \frac{y}{2}\right), 0 \right] \quad (57)$$

where ρ is the mass density of the fluid, ν is the kinematic viscosity which can be determined by Eq. (48) and $g = -dp/dx$ is the constant pressure gradient from the inlet

to the outlet. In this simulation, g is treated as the external force term in the lattice

Boltzmann equation and thus, the acceleration term in F_α can be written as $\mathbf{a} = \left[\frac{g}{\rho}, 0 \right]$.

The simulation was taken on a 256×32 grid system. The length and height of the computational domain are 1.0 and 0.125 respectively. The lattice speed c is set as 1.0 and the dimensionless relaxation time τ is 0.6. No gradient boundary condition was applied at the inlet and the outlet while no-slip boundary condition was implemented on the top and bottom walls. The fluid is initially stationary and is accelerated by the pressure gradient when $t > 0$. The calculation is terminated if the flow reaches its steady state. The convergence criterion is:

$$\max_{\alpha,i,j} \left| \frac{f_\alpha^{n+1}(i,j) - f_\alpha^n(i,j)}{f_\alpha^n(i,j)} \right| \leq 1 \times 10^{-8} \quad (58)$$

where the superscript $n+1$ denotes the values at the next time step. Different values of g were used in the calculation as long as the low Mach number approximation is retained. The relative errors between the simulation results and the analytical solution are listed in Table 2 where the error is defined as:

$$error = \frac{\sqrt{\sum_j [u_x^{LB}(128, j) - u_x^A(x_c, j\Delta y)]^2}}{\sqrt{\sum_j [u_x^A(x_c, j\Delta y)]^2}} \quad (59)$$

where u_x^{LB} represents the x-component velocity obtained from the simulation while u_x^A is the analytical solution from Eq. (57). The error is only calculated at the center cross section along the x-axis ($i = 128$) because the flow is in the steady state and u_x is not dependent upon x . The relative errors listed in Table 2 show that, although the

performances of Method 3 and Guo’s model are slightly better, the five external force models almost have the same accuracy for simulation of Poiseuille flow which is driven by a constant external force. Without surprise, the error grows with the increase of the magnitude of the force because a larger Mach number is resulted by a bigger external force. Figure 4 shows the profile of x-component velocity obtained by He’s model with $g = 5.774 \times 10^{-2}$. It is apparent that even with the largest error in Table 2, the simulation result is still in a good agreement with the analytical solution.

$g (\times 10^2)$	1.155	2.309	3.464	4.619	5.774
Models					
Method 1	4.499	4.888	6.314	8.414	11.043
Method 2	4.500	4.888	6.315	8.416	11.046
Method 3	3.672	3.931	5.116	7.057	9.596
Guo’s Model	3.672	3.931	5.116	7.058	9.597
He’s Model	4.500	4.888	6.315	8.416	11.046

Table 2 Relative errors ($\times 10^4$) of Poiseuille flow

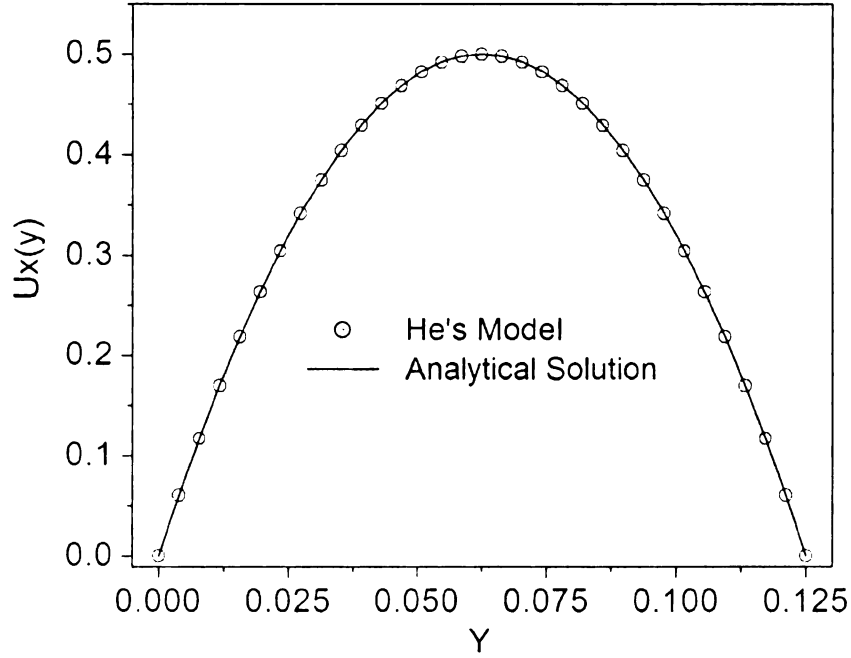


Figure 4 Profile of x-component velocity obtained by He's model ($g = 5.774 \times 10^{-2}$). The simulation results agree very well with the analytical solution.

As the second simulation example, an unsteady 2D Taylor vortex flow was simulated by all the five external force models aforementioned. The simulation was carried on a 129×129 grid system with the dimensions of the computation domain of $-\pi \leq x, y \leq \pi$. The space- and time-dependent acceleration due the external force is:

$$\mathbf{a} = \begin{bmatrix} -\frac{k_1 u_0^2}{2} \sin(2k_1 x) \exp[-2\nu(k_1^2 + k_2^2)t] \\ -\frac{k_1^2 u_0^2}{2k_2} \sin(2k_2 y) \exp[-2\nu(k_1^2 + k_2^2)t] \end{bmatrix} \quad (60)$$

where u_0 is the magnitude of the flow velocity and it is set as $u_0^2 = 0.001$ so that the compressibility of the flow can be neglected, ν is the fluid viscosity, k_1 and k_2 are the

wave numbers and $k_1 = k_2 = 1.0$ in the calculation. With the external force shown in Eq. (60), the analytical solution of the velocity field can be found as [138]:

$$\mathbf{u}^A = \begin{bmatrix} u_x \\ u_y \end{bmatrix} = \begin{bmatrix} -u_0 \cos(k_1 x) \sin(k_2 y) \exp[-\nu(k_1^2 + k_2^2)t] \\ u_0 \frac{k_1}{k_2} \sin(k_1 x) \cos(k_2 y) \exp[-\nu(k_1^2 + k_2^2)t] \end{bmatrix} \quad (61)$$

In the practical simulation, the time step Δt is set equal to the spacing step Δx . Then the dimensionless relaxation time τ can be retrieved from Eq. (48) with the value of $\nu = 0.005$. The initial velocity field is set as Eq. (61) with $t = 0$. The periodic boundary condition [153] is applied for all the four boundaries of the computational domain.

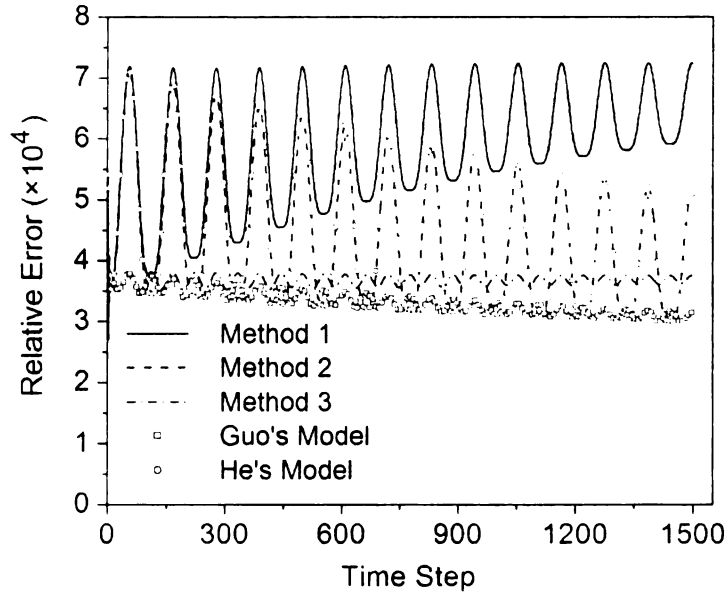


Figure 5 Evolution of relative errors of simulation of Taylor vortex flow obtained by the five external force models. All the errors are in the same order of values.

Figure 5 shows the relative errors of the simulation versus the time steps where the error is defined as:

$$error = \frac{\sqrt{\sum_{i,j} [\mathbf{u}^{LB}(i,j) - \mathbf{u}^A(i\Delta x, j\Delta y)]^2}}{\sqrt{\sum_{i,j} \mathbf{u}^A(i\Delta x, j\Delta y)^2}} \quad (62)$$

where $\mathbf{u}^{LB}(i,j)$ represents the velocity at the node point of (i,j) obtained by the LBM and $u^A(i\Delta x, j\Delta y)$ is the analytical solution according to Eq. (61) at the corresponding position $(i\Delta x, j\Delta y)$. It is clear from Figure 5 that all the relative errors are in the same order of magnitude. Although Method 3 and Guo's model present better performance in

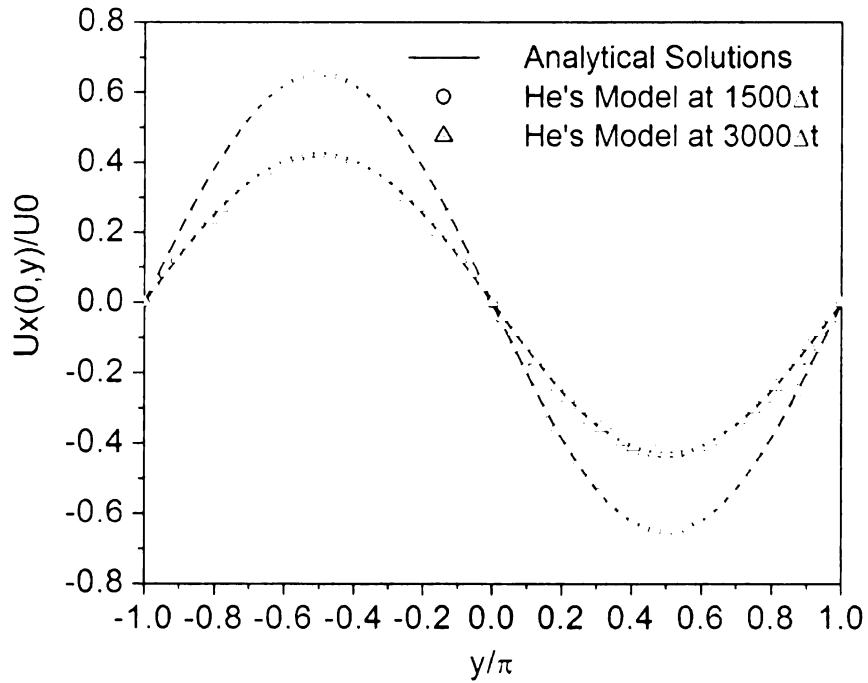


Figure 6 Profiles of x-component velocity along the center line of x-axis at time steps of 1500 and 3000 by using He's model. The simulation results are in good agreement with the analytical solutions.

simulate temporally and spatially varying force as illustrated in Figure 5, other methods also can give highly satisfactory results. For example, Figure 6 shows the profiles of x-component velocity along the center line of x-axis by using He's model at different time moments. Comparing with the analytical solutions which are represented by the solid lines in the plot, He's model can reproduce excellent results with respect to the analytical ones.

Finally, let's check the external force models by simulating a simple free diffusion problem with a constant force pointing to the positive x-direction. Initially, the fluid density has a Gaussian distribution centered in the computational domain with the maximum perturbation of the density as $0.01\rho_0$. With a constant external force acting along the positive x-direction, the analytical solution of the fluid density is:

$$\rho^A(x, y, t) = \rho_0 + \frac{0.01\rho_0}{(1+t/t_0)} \exp\left[-\frac{(x-x_c - v_d t)^2 + (y-y_c)^2}{r^2(1+t/t_0)}\right] \quad (63)$$

where (x_c, y_c) represents the center point of the computational domain, $r = 20\Delta x$ and $t_0 = r^2/4D$ where D is the diffusivity which can be recovered from the lattice Boltzmann equation as:

$$D = (\tau - 0.5)\theta^2\Delta t \quad (64)$$

In Eq. (63), v_d is the magnitude of the drift velocity \mathbf{v}_d due to the external force, which is calculated as follows [154]:

$$\mathbf{v}_d = -\mathbf{a}\tau\Delta t \quad (65)$$

The simulation was taken on a 129×129 grid system with the dimension of the computational as 1.0. The time step is set equal to the spacing and consequently the lattice speed $c = 1.0$. Different amplitudes of the acceleration were used in the calculation.

Table 3 lists the relative errors of the diffusion problem with different amplitudes of the external force. The relative error in this case has a similar definition as shown in Eq. (62) where the velocity is replaced by the fluid density:

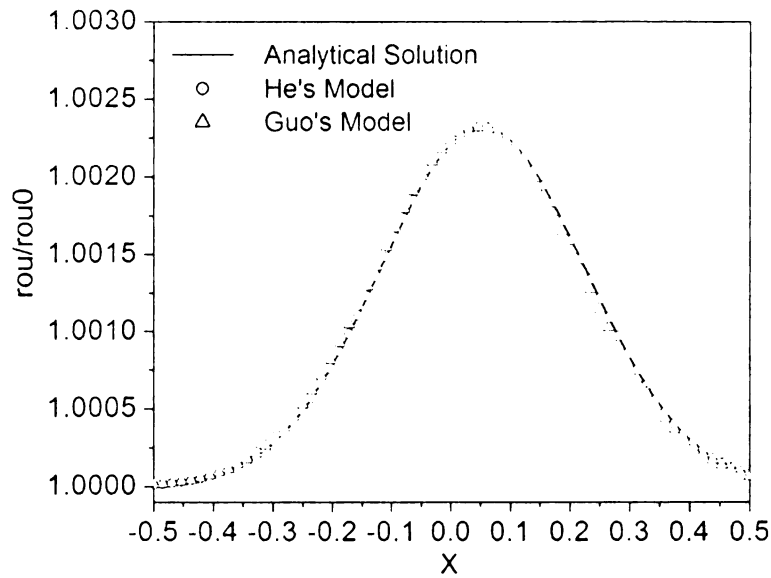
$$error = \frac{\sqrt{\sum_{i,j} [\rho^{LB}(i,j) - \rho^A(i\Delta x, j\Delta y)]^2}}{\sqrt{\sum_{i,j} \rho^A(i\Delta x, j\Delta y)^2}} \quad (66)$$

We can see from the table that the errors increase with the enlargement of the external force as expected. However, Method 3 and Guo's model show larger errors with respect to Method 1, Method 2 and He's model.

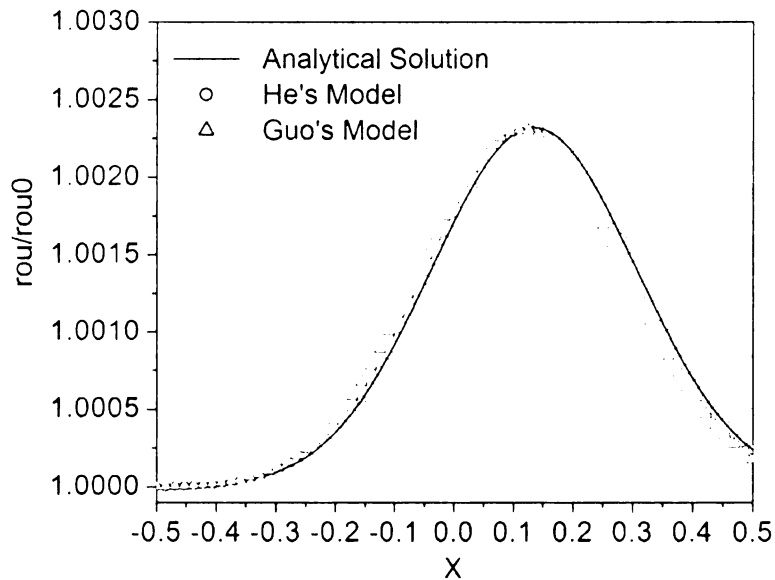
Figure 7 shows the fluid density distribution at 200 time steps with different amplitudes of the external force. The solid lines represent the analytical solutions. It can

a_x Models	0.5	2.0	4.0	6.0	8.0	10.0
Method 1	1.223	1.240	1.297	1.389	1.515	1.673
Method 2	1.223	1.250	1.335	1.471	1.650	1.864
Method 3	1.261	1.755	2.799	3.968	5.172	6.385
Guo's Model	1.271	1.862	3.060	4.371	5.705	7.033
He's Model	1.223	1.251	1.336	1.469	1.641	1.840

Table 3 Relative errors ($\times 10^5$) of free diffusion problem with different amplitudes of the external force



(a)



(b)

Figure 7 Fluid density distribution obtained by He's model and Guo's model at 200 time steps with different magnitudes of the external force: (a) $a_x = 4.0$ (b) $a_x = 10.0$. Both Guo's model and He's model can produce good results if the external force is small (as shown in (a)). However, if the external force is relatively large, Guo's model induces larger error than dose He's model (as shown in (b)).

be seen that the Guo's model can give relatively good results if the external force is small (Figure 7 (a)). However, if the external force is large to some level, e.g. the case of $a_x = 10.0$, Guo's model cannot reproduce the satisfactory results, as shown in Figure 7 (b). Meanwhile, as illustrated by Table 3 and Figure 7, the results obtained by He's model have good agreement with the analytical solutions even with a relatively large external force.

In conclusion, although Method 3 and Guo's model behave better in the simulations of Poiseuille flow and Taylor vortex flow, they show poor performance in the simulation free diffusion problem, especially when the amplitude of the external force is large. Method 1 possess higher accuracy for Poiseuille flow and the diffusion problem, but it gives large errors in simulation of Taylor vortex flow. Method 2 and He's model have the same accuracies for the Poiseuille flow and the Taylor vortex flow, but He's model is better in diffusion problem. Comprehensively considering the above observation from the results obtained by the five external force models, He's model is chosen in this research for all the simulations thereafter.

3.2 LBM Simulation of Magnetohydrodynamics Flows

By using He's model to evaluate the external force term, a hybrid lattice-Boltzmann finite-difference method is proposed in this research to simulate incompressible, resistive magnetohydrodynamic (MHD) flows. In recent years, many attempts have been made to develop LBM algorithms for MHD problems. Chen *et al.* [155] and Martinez *et al.* [156] employed the bidirectional streaming for 2-D MHD problems where the distribution is propagated into two different directions associated with the velocity and magnetic field. The former used 37 discrete velocities while the

latter reduced it to 13. Schaffenberg and Hansmeier [157] later reduced the number of velocities even further to nine by employing the standard streaming rule on a 2-D square lattice. Dellar [158] developed a new method, where two distribution functions are utilized to represent the hydrodynamic momentum and the magnetic induction. The hydrodynamic part is simulated using the conventional low Mach number LBM, and the magnetic field is represented by a separate vector-valued magnetic distribution function, which obeys the vector Boltzmann-BGK equation. This method has been later extended to 3-D by Breyannis and Valougeorgis [144].

In all the afore-mentioned methods, both the magnetic induction problem and the flow problem are dealt with by a lattice kinetic approach. However, while employing LBM for the Boltzmann equation is natural, the use of a kinetic approach for solving the magnetic induction equation is not quite intuitive because, after all, the Boltzmann equation and the magnetic induction equation constitute a set of governing equations for MHD. In other words, a lattice kinetic approach does not need to be used for the magnetic induction problem even though it is a more consistent approach and has many advantages in many cases. In fact, other numerical methods, such as the finite difference method, can be easily employed to solve the magnetic induction equation with equal or better accuracy because those methods are well established.

In this proposed hybrid model, the lattice Boltzmann equation with the Lorentz force term is solved to update the flow field while the magnetic induction equation is solved using the finite difference method to calculate the magnetic field. This approach is methodologically intuitive because the governing equations for MHD are solved in their respective original forms. In addition, the extension to 3D is straightforward. To validate

this newly developed model, the Hartmann flow, the Orszag-Tang vortex system (2D and 3D) and the magnetic reconnection driven by doubly periodic coalescence instability are simulated. The obtained results agree well with analytical solutions and simulation results available in the literature.

In the present model, the governing equation is the BGK-type Boltzmann equation as shown in Eq. (8), where the equilibrium distribution function f^{eq} is described by the Maxwell-Boltzmann distribution as follows:

$$f^{eq} = \frac{\rho}{(2\pi\theta^2)^{D/2}} \exp\left[-\frac{(\mathbf{v} - \mathbf{u})^2}{2\theta^2}\right] \quad (67)$$

where ρ and D are mass density and dimension of space, respectively. For MHD flows, the acceleration \mathbf{a} can be written as:

$$\mathbf{a} = \frac{1}{\rho\mu} (\nabla \times \mathbf{B}) \times \mathbf{B} \quad (68)$$

Here, \mathbf{B} is magnetic induction and μ is magnetic permeability. The evolution of magnetic field is obtained by solving the magnetic induction equation, which is derived from Maxwell's equations with the assumption of $\partial\mathbf{E}/\partial t = 0$ [129]:

$$\frac{\partial\mathbf{B}}{\partial t} = \eta\nabla^2\mathbf{B} + (\mathbf{B} \cdot \nabla)\mathbf{u} - (\mathbf{u} \cdot \nabla)\mathbf{B} \quad (69)$$

where η is magnetic diffusivity and is expressed as $\eta = (\mu\sigma)^{-1}$, where σ is the electrical conductivity.

For 2D problems, the Boltzmann equation can be discretized by D2Q9 scheme as described in Chapter 2. The external force term is evaluated by He's model. Then the resulted lattice Boltzmann equation follows the form of Eq. (52) where the discretized

equilibrium distribution function takes the form Eq. (32). The mass density and momentum then can be calculated through:

$$\rho = \sum_{\alpha} f_{\alpha} \quad (70)$$

$$\rho \mathbf{u} = \sum_{\alpha} \mathbf{e}_{\alpha} f_{\alpha} \quad (71)$$

The magnetic induction equation (Eq. (69)) is solved by the conventional finite difference method. In two dimensions, for example, the x -component of Eq. (69) is written as:

$$\frac{\partial B_x}{\partial t} = \frac{1}{\mu\sigma} \left(\frac{\partial^2 B_x}{\partial x^2} + \frac{\partial^2 B_x}{\partial y^2} \right) + B_x \frac{\partial u_x}{\partial x} + B_y \frac{\partial u_x}{\partial y} - u_x \frac{\partial B_x}{\partial x} - u_y \frac{\partial B_x}{\partial y} \quad (72)$$

Then the following discretized equation is obtained if the central difference scheme is employed.

$$\begin{aligned} \frac{\partial (B_x)_{i,j}}{\partial t} = \frac{1}{\mu\sigma} & \left[\frac{(B_x)_{i+1,j}^n - 2(B_x)_{i,j}^n + (B_x)_{i-1,j}^n}{(\Delta x)^2} \right. \\ & \left. + \frac{(B_x)_{i,j+1}^n - 2(B_x)_{i,j}^n + (B_x)_{i,j-1}^n}{(\Delta y)^2} \right] \\ & + (B_x)_{i,j}^n \frac{(u_x)_{i+1,j}^n - (u_x)_{i-1,j}^n}{2\Delta x} + (B_y)_{i,j}^n \frac{(u_x)_{i+1,j}^n - (u_x)_{i,j-1}^n}{2\Delta y} \\ & - (u_x)_{i,j}^n \frac{(B_x)_{i+1,j}^n - (B_x)_{i-1,j}^n}{2\Delta x} - (u_y)_{i,j}^n \frac{(B_x)_{i,j+1}^n - (B_x)_{i,j-1}^n}{2\Delta y} \end{aligned} \quad (73)$$

Note that all the terms on the right hand side are evaluated at time step n using the fluid velocity calculated by the lattice Boltzmann solver. Eq. (73) can be re-written as follows:

$$\frac{\partial (B_x)_{i,j}}{\partial t} = R \left((B_x)^n \right) \quad (74)$$

In this study, the time derivative on the left hand side is discretized by the second-order Runge-Kutta method:

$$\begin{aligned}(B_x)^{n+1/2} &= (B_x)^n + \frac{\Delta t}{2} R\left((B_x)^n\right) \\ (B_x)^{n+1} &= (B_x)^n + \Delta t R\left((B_x)^{n+1/2}\right)\end{aligned}\tag{75}$$

For validation purposes, the 2D Hartmann flow is simulated because its analytical solution can be easily obtained. Hartman flow is a channel flow induced by a uniform magnetic field (B_0) applied perpendicular to the flow direction. For 2D Hartmann flows, velocity has only one component in the channel direction $\mathbf{u} = (u_x, 0)$ and this flow induces additional magnetic field in the flow direction. Therefore, magnetic field can be written as $\mathbf{B} = (B_x, B_0)$. The magnetic induction equation and the hydrodynamic momentum equation can be simplified as follows:

$$\frac{1}{\mu\sigma} \frac{d^2 B_x}{dy^2} + B_0 \frac{du_x}{dy} = 0\tag{76}$$

$$\rho\nu \frac{d^2 u_x}{dy^2} + \frac{B_0}{\mu} \frac{dB_x}{dy} = g\tag{77}$$

where $g = \frac{dp}{dx}$ is the constant pressure gradient used to drive the flow along the x -

direction. By using the following boundary conditions

$$\begin{cases} u_x = 0 & \text{at } y = \pm L \\ B_x = 0 & \text{at } y = \pm L \end{cases}\tag{78}$$

the analytical solutions to Eqs. (76) and (77) are obtained as:

$$u_x(y) = \frac{gM}{\sigma B_0^2} \coth(M) \left[\frac{\cosh(My/L)}{\cosh(M)} - 1 \right]\tag{79}$$

$$B_x(y) = -\frac{g\mu L}{B_0} \left[\frac{\sinh(My/L)}{\sinh(M)} - \frac{y}{L} \right] \quad (80)$$

where $M = B_0 L \sqrt{\sigma/\rho\nu}$ is the Hartmann number. If there is no external magnetic field, the Hartmann number becomes zero and the flow reduces to the Poiseuille flow, which has solutions of $u_x(y) = g(L^2 - y^2)/2\rho\nu$ and $B_x = 0$.

For the LBM simulation of the Hartmann flow, the initial distribution function is set to the equilibrium distribution function with constant density, $\rho = 1.0$; u_x and B_x are set to zero. A uniform magnetic field B_0 is applied in the y -direction. The bounce-back condition is used for wall boundaries while the periodic boundary condition is used at the inlet and the outlet. The simulation is terminated until a steady state is reached. To drive the flow, the driving pressure $g\mathbf{x}$ is added to the external force as follows:

$$\rho\mathbf{a} = \frac{1}{\mu}(\nabla \times \mathbf{B}) \times \mathbf{B} + g\hat{\mathbf{e}}_x \quad (81)$$

In Eq. (81), $\hat{\mathbf{e}}_x$ is the unit vector in the x -direction.

Figure 8 and Figure 9 present simulation results of u_x and B_x respectively, where solid lines denote analytical solutions given by Eqs. (79) and (80). As clearly seen, the simulation results agree well with the analytical solutions for all Hartmann numbers considered. In this simulation, a 200×20 grid is used and the parameters of $\tau = 0.635$, $\sigma = 10$ and $g = 2.5 \times 10^{-5}$ are adopted. The Hartmann numbers of 0, 1, 2, 5, 10 and 20 are considered. Note that the Hartmann number can be changed by varying the magnitude of the applied magnetic field B_0 . In Figure 8, it is shown that as the Hartmann number increases the velocity profile becomes flatter, which can be explained by Eq. (80).

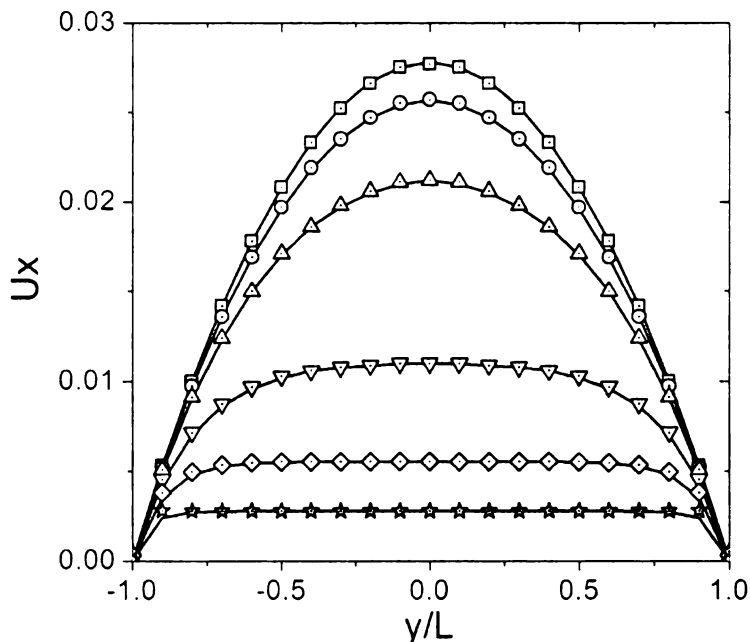


Figure 8 Profiles of x-component velocity with different Hartmann numbers: $M=0$ (squares), $M=1$ (circles), $M=2$ (upper triangles), $M=5$ (lower triangles), $M=10$ (diamonds), $M=20$ (stars). The solid lines show the analytical solutions. The simulation results agree very well with the analytical solutions.

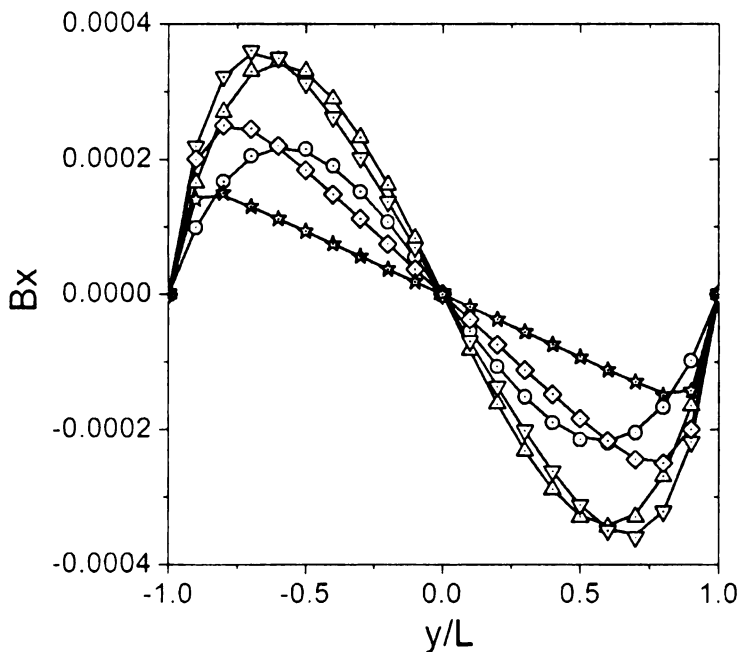


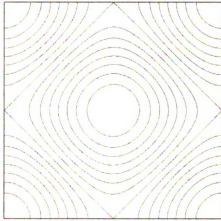
Figure 9 Profiles of x-component magnetic field for different Hartmann numbers: $M=0$ (squares), $M=1$ (circles), $M=2$ (upper triangles), $M=5$ (lower triangles), $M=10$ (diamonds), $M=20$ (stars). The solid lines show the analytical solutions. The simulation results agree very well with the analytical solutions.

Clearly, the applied magnetic field (B_0) tends to reduce the magnitude of x -component velocity. If the Hartmann number is finite, the velocity profile cannot be entirely flat even for very large Hartmann numbers and there must be a region with a large velocity gradient because velocity is forced to be zero due to the no slip boundary conditions. Figure 9 presents the magnetic field induced by the flow for a variety of Hartmann numbers, the simulation results agree with the analytical solutions very well.

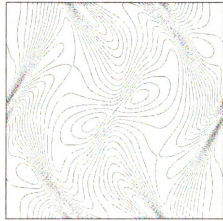
As the second test problem, the Orszag-Tang vortex system (which is an unsteady, nonlinear MHD flow problem) was chosen. Since Orszag and Tang [159] first studied this problem, it has become a popular benchmark problem because many aspects of MHD turbulent flows appear in this problem, such as the dynamic alignment, selective decay and magnetic reconnection [160]. In this study, a 2D Orszag-Tang vortex problem is simulated with the following simple nonrandom deterministic initial conditions:

$$\begin{aligned}\mathbf{u}_0 &= -u_0(\sin y, -\sin x) \\ \mathbf{B}_0 &= -B_0(\sin y, -\sin(2x))\end{aligned}\tag{82}$$

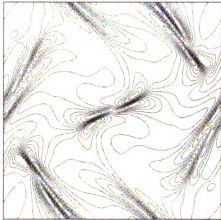
where $u_0 = 2.0$ and $B_0 = 2.0$ are the initial velocity and magnetic induction, respectively. The simulation is performed on a square domain of $0 \leq x, y \leq 2\pi$. A 512×512 uniform grid is used and the periodic boundary conditions are applied on all boundaries. Kinetic fluid viscosity and magnetic diffusivity are assumed to be the same ($\nu = \eta = 0.02$), which leads to the same Reynolds number (Re) and magnetic Reynolds number (Rem) at the initial stage. With the initial conditions shown in Eq. (82), the evolution of the vorticity of fluid ($\boldsymbol{\omega} = \nabla \times \mathbf{u}$) and the current density ($\mathbf{j} = \nabla \times \mathbf{B} / \mu_0$) are demonstrated in Figure 10 and Figure 11, respectively. As shown in Figure 10 and Figure 11, initially both velocity field and magnetic field have symmetric structures. As time elapses, the initial flow



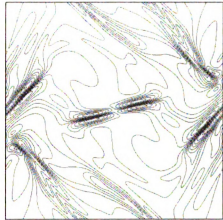
$t = 0$



$t = 0.369$

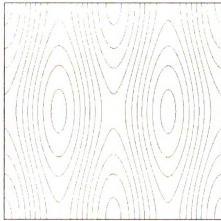


$t = 0.738$

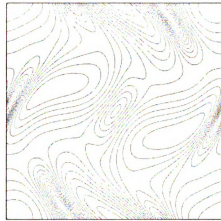


$t = 1.00$

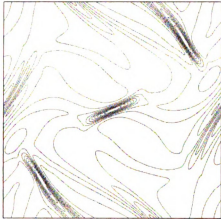
Figure 10 Evolution of vorticity for the 2-D Orszag-Tang vortex. The flow pattern becomes complicated due to the nonlinear interactions between the velocity field and the magnetic field. A flat quadrupole-like configuration emerges with time lapse.



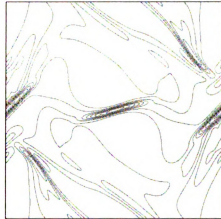
$t = 0$



$t = 0.369$



$t = 0.738$



$t = 1.00$

Figure 11 Evolution of current density for the 2-D Orszag-Tang vortex. The existing current sheet at the center of the figure is enhanced and eventually, a thin elliptic structure establishes due to the magnetic reconnection occurring there.

pattern becomes complicated due to the nonlinear interactions between the velocity field and the magnetic field. In Figure 11, the existing current sheet at the center of the figure is enhanced and eventually, a thin elliptic structure establishes due to the magnetic reconnection occurring there. At the same time, a region of sheared flow coexists with the current sheet, which is shown as the flat quadrupole-like configuration in Figure 10. The contours of the vorticity and the current density agree well qualitatively with the simulation results available in the literature [160].

In order to validate this model quantitatively, this problem was simulated by using the same parameters used in the paper by Dellar [158] ($u_0 = 2.0$, $\nu = \eta = 0.02$, and a 512×512 grid). The maximum vorticity value at $t = 0.5$ predicted by this model is 6.764 while Dellar's result gives a values of 6.758. At $t = 1.0$, the values are 14.457 and 14.20 respectively. The maximum current densities are also compared and the values are given in Table 4. In order to check if these two models satisfy the divergence-free property of the magnetic field, the values of $|\nabla \cdot \mathbf{B}|$ are calculated. The presented model gives 0.00463 at $t = 0.5$ and 0.00922 at $t = 1.0$ while Dellar's results indicate 0.0062 and 0.0415 at the corresponding times. Therefore, the presented model is validated not only qualitatively, but also quantitatively.

	Time (sec)	Max vorticity	Max current	$ \nabla \cdot \mathbf{B} $
Present results	0.50	6.764	18.129	0.00463
	1.0	14.457	45.963	0.00922
Dellar's results	0.50	6.758	18.24	0.0062
	1.0	14.20	46.59	0.0415

Table 4 Quantitative comparison of simulation results with Dellar's work

To show that this model can be easily extended to 3D, the D3Q19 lattice model [161] has been employed to solve the 3D Orszag-Tang vortex problem with the following initial conditions [162]:

$$\begin{aligned} \mathbf{u}_0 &= (-2 \sin y, 2 \sin x, 0) \\ \mathbf{B}_0 &= 0.8(-2 \sin(2y) + \sin z, 2 \sin x + \sin z, \sin x + \sin y) \end{aligned} \quad (83)$$

A cubic domain of $2\pi \times 2\pi \times 2\pi$ is used and simulations are conducted on a $64 \times 64 \times 64$ grid. Periodic boundary conditions are used for all boundary surfaces and edges. Figure 12 (a-b) shows the initial contours of the magnitudes of vorticity ($|\boldsymbol{\omega}|$) and current density ($|\mathbf{j}|$). In Figure 12 (c-d), $|\boldsymbol{\omega}|$ and $|\mathbf{j}|$ at $t = 0.598$ are shown and the slices of $|\boldsymbol{\omega}|$ and $|\mathbf{j}|$ at $z = 0$ are presented. The patterns of the current sheet and the corresponding vorticity resemble Figure 11 and Figure 10 closely because initially, the variations of current density and vorticity in z -directions are relatively smaller in values than those in the x - and y -direction.

Magnetic reconnection is the third example simulated by the present model. It is the process where magnetic field lines from different magnetic domains merge into one another, changing the overall topology of the magnetic field. Meanwhile, the stored

magnetic energy is released in heat and kinetic energy forms. The magnetic reconnection can be driven by different forms of coalescence instability, for example, by the merging of a chain of magnetic islands [163] or by doubly periodic coalescence instability [164]. In this study, a magnetic reconnection problem driven by the doubly periodic coalescence instability is simulated using the present model. As the initial distribution of magnetic flux, a checkerboard pattern [165] represented by Eq. (84) is employed.

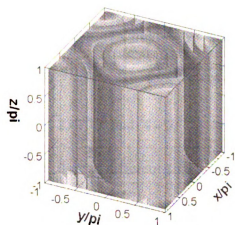
$$\psi_0(x, y) = B_0 \sin(\pi(x + y)) \sin(\pi(x - y)) \quad (84)$$

The symmetric initial perturbation of the kinetic stream function is:

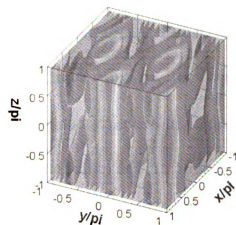
$$\varphi_0(x, y) = u_0 \exp(-10(x^2 + y^2)) \quad (85)$$

where $B_0 = 0.5/\pi$, $u_0 = 0.05$ and the initial magnetic and velocity fields are obtained as follows:

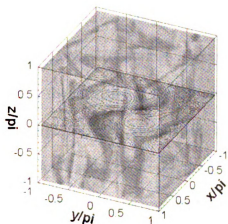
$$\begin{aligned} \mathbf{B}_0 &= \hat{\mathbf{e}}_z \times \nabla \psi_0 = \left(-\frac{\partial \psi_0}{\partial y}, \frac{\partial \psi_0}{\partial x} \right) \\ \mathbf{u}_0 &= \hat{\mathbf{e}}_z \times \nabla \varphi_0 = \left(-\frac{\partial \varphi_0}{\partial y}, \frac{\partial \varphi_0}{\partial x} \right) \end{aligned} \quad (86)$$



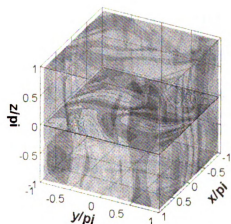
(a) $|\omega|$ at $t = 0$



(b) $|j|$ at $t = 0$



(c) $|\omega|$ at $t = 0.598$ with a 2D contour at $z=0$



(d) $|j|$ at $t = 0.598$ with a 2-D contour at $z=0$

Figure 12 Iso-surface contours of magnitudes of vorticity and current density at $t=0$ and $t=0.598$ sec for the 3-D Orszag-Tang vortex. The patterns of the current sheet and the corresponding vorticity resemble Figure 11 and Figure 10 closely because initially, the variations of current density and vorticity in z -directions are relatively smaller in values than those in the x - and y -direction.

The simulation is conducted on a square domain of $-1 \leq x, y \leq 1$ and a 256×256 grid is used. Periodic boundary conditions are used on all boundaries. A fixed viscosity of $\nu = 4 \times 10^{-3}$ is used; five values of magnetic diffusivity ($\eta = 0.5 \times 10^{-3}$, 0.8×10^{-3} , 1×10^{-3} , 2×10^{-3} and 4×10^{-3}) are considered. Figure 13 presents the evolution of magnetic flux at different times with the magnetic diffusivity of 1×10^{-3} . Note that the position of the magnetic current sheets does not change with time because the initial perturbation of the kinetic stream function has a mirror symmetry with respect to x and y directions. It can be seen from Figure 13 that the magnetic islands with currents of the same sign move towards each other. The two corners coalesce into one and the original two square cells become two adjacent pentagons. A current sheet forms between the two cells and the intensity of the current sheet increases. Eventually, the neighboring square cells merge together, simplifying the topology structure of the magnetic field to four square-like islands. Figure 14, presenting the dependence of maximum current density on magnetic diffusivity, is a quantitative evidence of the present model. As seen from the plot, the temporal maximum of current density can be approximated as $j_{\max} \propto \eta^{-1/2}$ as illustrated by the dashed line in Figure 14, which can be compared with Fig. 3 in [165].

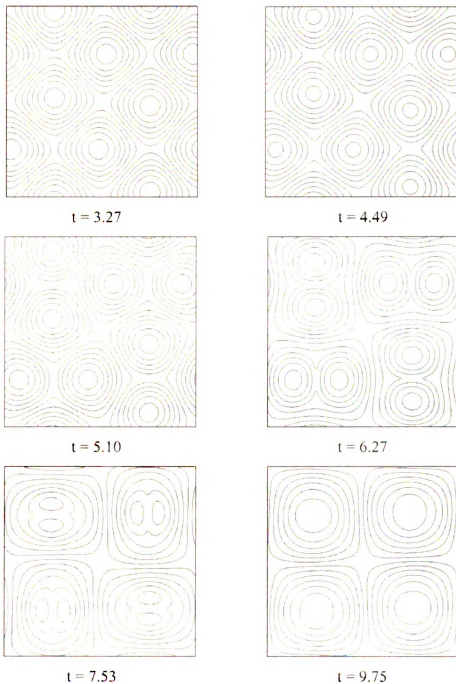


Figure 13 Evolution of magnetic flux function for doubly periodic coalescence instability. The position of the magnetic current sheets does not change with time. The magnetic islands move towards each other. The two corners coalesce into one and the original two square cells become two adjacent pentagons. A current sheet forms between the two cells and the intensity of the current sheet increases. Eventually, the neighboring square cells merge together, simplifying the topology structure of the magnetic field to four square-like islands.

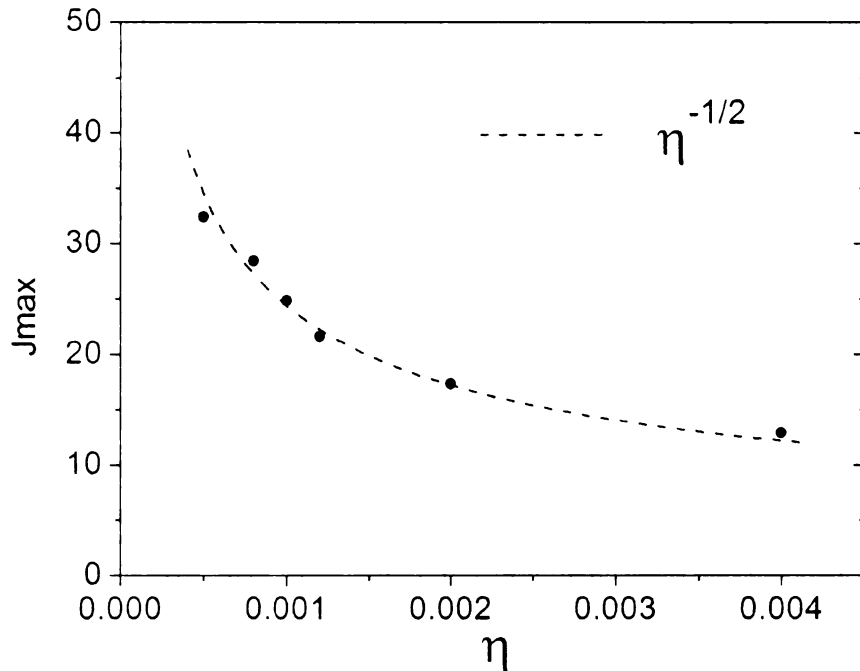


Figure 14 Maximum value of current density vs. magnetic diffusivity. The temporal maximum of current density can be approximated as $j_{\max} \propto \eta^{-1/2}$.

In conclusion, three classic problems in MHD flows were solved in this study and the obtained results agreed well with the data available in the literature. This newly developed hybrid LBM model has the following advantages: first, its implementation is relatively simple compared to other LBMs and Navier-Stokes equation based methods; second, the extension to 3-D is straightforward. We believe that this approach can be a good alternative to other MHD-LBMs that are fully based on the lattice kinetic algorithms.

Chapter 4

Lattice Boltzmann Simulation of Isothermal Weakly Ionized Plasmas

As the governing equation for all transport phenomena, the Boltzmann transport equation describes the evolution of the distribution function of each species of particles in the plasma. All macroscopic variables of the plasma, such as number density and macroscopic velocity, can be retrieved through proper moments of the distribution function. Many achievements of LBM development (especially multi-component models [166-170]) can be inherited in the plasma simulation, since plasmas are mixtures of different types of particles. Among those models, the finite difference lattice Boltzmann (FDLB) models [168, 169] can be used for asymmetric system, which is the system in which the composite particles have different properties. However, the direct use of the FDLB models for plasma simulation is not sufficient due to some exclusive characteristics of plasmas. For example, if the physical plasma parameters are used, a very large dimensionless relaxation time will result. This relaxation time will significantly reduce the effects of the collision term on the evolution of the distribution function and thus lead to an ill-favored transport behavior of the electrons. Therefore, to overcome this problem, the LBM simulation parameters should be selected in such a way that the dimensionless relaxation time is in a valid value range. In this chapter, a new LBM model is proposed to simulate weakly ionized isothermal helium plasmas. The simulation parameters used in LBM are selected according to a rescaling scheme developed in this research to match the physical properties of the plasma. For the purpose

of validation, the electron diffusion problem and the electrostatic wave phenomena are simulated by this new model and the results show good agreement with the analytical solutions.

4.1 Mathematical Model

The proposed LBM model in this chapter is based upon the following assumptions:

- 1) Inelastic collisions, such as ionization and recombination, are not considered.
- 2) The plasma is isothermal, but different species can have different temperatures.
- 3) The plasma consists of electrons, neutrals, and singly ionized ions (three species).

Then the Boltzmann transport equation for the three species of particles in a weakly ionized helium plasma can be written:

$$\frac{\partial f_s}{\partial t} + \mathbf{v}_s \cdot \nabla f_s + \mathbf{a}_s \cdot \nabla_{\mathbf{v}_s} f_s = \left(\frac{\delta f_s}{\delta t} \right)_{coll} \quad (87)$$

The subscript s denotes the type of particles and can take e , i , and n for electrons, ions, and neutrals, respectively. In this equation, \mathbf{v}_s is the microscopic velocity, $f_s = f_s(\mathbf{x}, \mathbf{v}, t)$ is the number density distribution function, and \mathbf{a}_s is the acceleration due to the Lorentz force, which is expressed as

$$\mathbf{a}_s = \frac{q_s \mathbf{E}}{m_s} \quad (88)$$

if electrostatic behaviors of plasmas are considered. Here, \mathbf{E} is electric field, q_s and m_s are charge and mass of species s , respectively.

By only considering the binary collisions in the plasma and applying the similar splitting technique adopted for binary gas mixture [166], the collision term for species s can be written as:

$$\left(\frac{\delta f_s}{\delta t} \right)_{coll} = J^{se} + J^{si} + J^{sn} \quad (89)$$

where J^{se} , J^{si} and J^{sn} are the terms that represent the collisions with electrons, ions, and neutrals, respectively. It is well known that if the plasma is weakly ionized, the elastic collision with neutral particles is the dominant collision mechanism for all species. Therefore, J^{se} and J^{si} are negligible in the weakly-ionized plasmas. For the collisions with neutral particles, the Bhatnagar-Gross-Krook (BGK) model is used, which assumes that the particles relax to their equilibrium states during the characteristic time period, which is called the relaxation time λ_s . Then, the Boltzmann equations for electrons, ions, and neutrals can be written as

$$\frac{\partial f_e}{\partial t} + \mathbf{v}_e \cdot \nabla f_e + \mathbf{a}_e \cdot \nabla_{\mathbf{v}_e} f_e = -\frac{f_e - f_{en}^{eq}}{\lambda_{en}} \quad (90)$$

$$\frac{\partial f_i}{\partial t} + \mathbf{v}_i \cdot \nabla f_i + \mathbf{a}_i \cdot \nabla_{\mathbf{v}_i} f_i = -\frac{f_i - f_{in}^{eq}}{\lambda_{in}} \quad (91)$$

$$\frac{\partial f_n}{\partial t} + \mathbf{v}_n \cdot \nabla f_n = -\frac{f_n - f_{nn}^{eq}}{\lambda_{nn}} \quad (92)$$

where λ_{en} , λ_{in} , λ_{nn} are the relaxation times for electron-neutral, ion-neutral, and neutral-neutral collisions, respectively; f_{en}^{eq} , f_{in}^{eq} , f_{nn}^{eq} are the equilibrium distribution functions of electrons, ions, neutrals, respectively, due to the collisions with neutrals and can be written as

$$f_{sn}^{eq}(\mathbf{u}_{sn}) = \frac{n_s}{2\pi\theta_s^2} \exp\left(-\frac{(\mathbf{v}_s - \mathbf{u}_{sn})^2}{2\theta_s^2}\right) \quad (93)$$

Note that the collisions with the species other than neutral particles can be easily added in the model. In Eq. (93), $\theta_s = \sqrt{k_B T_s / m_s}$ is the sound speed of species s where T_s is the temperature of species s ; \mathbf{u}_{sn} is the barycentric velocity of the binary collision with the neutral particle:

$$\mathbf{u}_{sn} = \frac{m_s \mathbf{u}_s + m_n \mathbf{u}_n}{m_s + m_n} \quad (94)$$

where \mathbf{u}_s is macroscopic velocity of species s (\mathbf{u}_n : macroscopic velocity of neutrals). Note that $\mathbf{u}_{nn} = \mathbf{u}_n$ but $\mathbf{u}_{en} \neq \mathbf{u}_e$ and $\mathbf{u}_{in} \neq \mathbf{u}_i$. That is due to the fact that the frequency of self-collisions between charged particles is very low in weakly ionized plasmas and the charged particles cannot relax to their macroscopic velocity during the relaxation time period (λ_{en} or λ_{in}) when they collide with neutral particles.

Similar with the concept of density dependent relaxation time [171], λ_{sn} in Eqs. (90) – (92) are written as [129]:

$$\lambda_{sn} = \frac{1}{\sigma_{sn} n_n \langle \bar{v}_s \rangle} \quad (95)$$

Here, σ_{sn} is the cross section of the elastic collision between species s and neutrals and calculated as $\sigma_{sn} = \pi(r_s + r_n)^2$, where r_s and r_n are the radii of species s and n respectively; $\langle \bar{v}_s \rangle$ is the average speed of species s , and $\langle \bar{v}_s \rangle = \left(\frac{8}{\pi} \frac{k_B T_s}{m_s} \right)^{1/2}$ [129]. Note

that the relaxation time presented in Eq. (95) is independent of temperature because only isothermal plasmas are considered in this chapter.

Now the Boltzmann equations shown in Eqs. (90) – (92) can be discretized by a traditional D2Q9 scheme and the external force term follows He's model:

$$f_e^\alpha(\mathbf{x} + \mathbf{e}_e^\alpha \Delta t, t + \Delta t) = f_e^\alpha(\mathbf{x}, t) - \frac{1}{\tau_{en}} (f_e^\alpha(\mathbf{x}, t) - f_{en}^{eq, \alpha}(\mathbf{x}, t)) + \frac{\Delta t \mathbf{a}_e \cdot (\mathbf{e}_e^\alpha - \mathbf{u}_e)}{\theta_e^2} f_e^{eq, \alpha} \quad (96)$$

$$f_i^\alpha(\mathbf{x} + \mathbf{e}_i^\alpha \Delta t, t + \Delta t) = f_i^\alpha(\mathbf{x}, t) - \frac{1}{\tau_{in}} (f_i^\alpha(\mathbf{x}, t) - f_{in}^{eq, \alpha}(\mathbf{x}, t)) + \frac{\Delta t \mathbf{a}_i \cdot (\mathbf{e}_i^\alpha - \mathbf{u}_i)}{\theta_i^2} f_i^{eq, \alpha} \quad (97)$$

$$f_n^\alpha(\mathbf{x} + \mathbf{e}_n^\alpha \Delta t, t + \Delta t) = f_n^\alpha(\mathbf{x}, t) - \frac{1}{\tau_{nn}} (f_n^\alpha(\mathbf{x}, t) - f_{nn}^{eq, \alpha}(\mathbf{x}, t)) \quad (98)$$

where Δt is time step; τ_{en} , τ_{in} , τ_{nn} are dimensionless relaxation times; superscript α denotes the α^{th} component in the phase space; \mathbf{e}_s^α is the α^{th} component of discretized microscopic velocity of species s as defined by Eq. (28). The discretized equilibrium distribution functions f_{ss}^{eq} as well as the weights ω_α are in similar forms defined in Chapter 2. Note that the self-collision distribution functions of the charged particles are used in evaluation of the external force term by using He's model. This selection will be justified later.

In multi-component LBM, if the same grid is used for all species, the time steps for different species are all different because time step is determined by $\Delta t = \Delta x / c_{ls}$, where Δx is the spacing and c_{ls} is the lattice speed of particle species s . Using several different time steps are very undesirable for a number of reasons, so in this model we use a single time step based on the lattice speed of electrons. Then, during a time step Δt ,

electrons travel a distance of $\mathbf{e}_e^\alpha \Delta t$ to the neighboring node while ions and neutrals travel a distance of $\mathbf{e}_i^\alpha \Delta t$ and $\mathbf{e}_n^\alpha \Delta t$, respectively. Since the lattice speeds of ions and neutrals are significantly smaller than that of electrons, the travel distance of those heavy particles will be very small compared to the electron travel distance. As a result, if the same grid is used for all species, ions and neutrals cannot reach the same node point as the electrons do and an interpolation scheme [124, 172-175] needs to be used for heavier particles. In this study, similar to the interpolation scheme used in [173, 174], a second-order interpolation method is introduced to find the on-node values of the discretized distribution functions for ions and neutrals. In Figure 15, q and o denote two neighboring nodes of p along the α^{th} direction (pointing from o to p). The ions (neutrals) that are originally located at o , p , q arrive at o' , p' , q' after a streaming step. The distribution function at p can be obtained by using $f_s^\alpha(o')$, $f_s^\alpha(p')$ and $f_s^\alpha(q')$ as follows:

$$f_s^\alpha(p) = f_s^\alpha(p') - \frac{f_s^\alpha(q') - f_s^\alpha(o')}{2} \frac{|\mathbf{e}_s^\alpha|}{|\mathbf{e}_e^\alpha|} + \frac{f_s^\alpha(q') - 2f_s^\alpha(p') + f_s^\alpha(o')}{2} \frac{|\mathbf{e}_s^\alpha|^2}{|\mathbf{e}_e^\alpha|^2} \quad (99)$$

where s can be e , i or n and

$$\begin{aligned} f_s^\alpha(o') &= \tilde{f}_s^\alpha(o) \\ f_s^\alpha(p') &= \tilde{f}_s^\alpha(p) \\ f_s^\alpha(q') &= \tilde{f}_s^\alpha(q) \end{aligned} \quad (100)$$

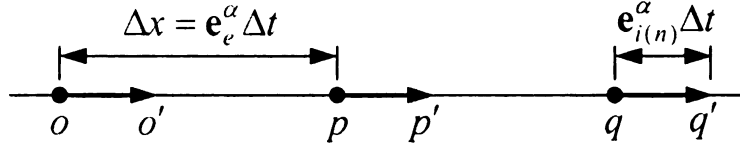


Figure 15 Schematic of second order interpolation method for ion (neutral) distribution function. The value of distribution function of the heavy particles at p can be found by using the post-collision values at o' , p' and q' .

where \tilde{f}_s^α is the post-collision distribution function after the collision step according to the lattice Boltzmann equations shown in Eqs. (96) - (98). If we define

$$\beta = \left| \mathbf{e}_s^\alpha \right| / \left| \mathbf{e}_e^\alpha \right| = \sqrt{T_s m_e / T_e m_s}, \text{ then:}$$

$$f_s^\alpha(p) = (1 - \beta^2) f_s^\alpha(p') - 0.5\beta(1 - \beta) f_s^\alpha(q') + 0.5\beta(1 + \beta) f_s^\alpha(o') \quad (101)$$

Note that if $s = e$, $\beta = 1$ and $f_e^\alpha(p) = f_e^\alpha(o') = \tilde{f}_e^\alpha(o)$ which is just the result of the ordinary streaming step.

Once distribution functions are updated, the number density and velocity of each species and charge density can be obtained as follows:

$$n_s(\mathbf{x}) = \sum_{\alpha} f_s^\alpha(\mathbf{x}) \quad (102)$$

$$n_s(\mathbf{x}) \mathbf{u}_s(\mathbf{x}) = \sum_{\alpha} f_s^\alpha(\mathbf{x}) \mathbf{e}_s^\alpha(\mathbf{x}) \quad (103)$$

$$\rho_v(\mathbf{x}) = e(n_i(\mathbf{x}) - n_e(\mathbf{x})) \quad (104)$$

The electric field \mathbf{E} is updated by solving the following equation:

$$\nabla^2 \phi = -\frac{\rho_v}{\epsilon_0} \quad (105)$$

where ε_0 is electric permittivity of vacuum; ϕ is the electric potential, and $\nabla\phi = -\mathbf{E}$. Eq. (105) is solved by a Poisson solver.

4.2 Rescaling Scheme

The governing Boltzmann equation of the present model is discretized by the traditional D2Q9 scheme. In this standard procedure, there are three parameters that can be chosen freely: dimensionless relaxation time τ , grid spacing Δx and time step Δt . Then, the sound speed $\tilde{\theta}$, in the D2Q9 model, is determined as $\tilde{\theta} = \Delta x / \sqrt{3} \Delta t$ and the viscosity is recovered by the Chapman-Enskog expansion of the lattice Boltzmann equation as follows [134, 137]:

$$\tilde{\nu} = (\tau - 0.5) \tilde{\theta}^2 \Delta t = \frac{(\tau - 0.5) \tilde{\theta} \Delta x}{\sqrt{3}} \quad (106)$$

Note that a tilde is used for the viscosity and the sound speed to distinguish themselves from the physical kinematic viscosity and the physical sound speed. We will call $\tilde{\nu}$ and $\tilde{\theta}$ the *lattice kinematic viscosity* and the *lattice sound speed* respectively in this dissertation. For some flow problems, such as driven cavity flow, the fluid flow is characterized solely by the Reynolds number and the value of viscosity is not important as long as the same flow pattern is obtained. In such a case, the lattice kinematic viscosity need not be identical to the physical one, and the three lattice parameters can be selected freely as just mentioned. In some cases, other dimensionless numbers, such as Peclet number and Froude number, can be used to scale LB simulations. But for certain flow problems, actual physical properties need to be used for the simulation because a particular dimensionless number (such as Reynolds number) does not characterize the flow and/or the flow depends strongly on some properties of a fluid. For example, in the

plasma diffusion problem, the Reynolds number is not important and the diffusion characteristic is governed by the diffusivity. Therefore, the diffusivity (in this case kinematic viscosity) must be matched explicitly. If the physical properties are used, the number of parameters that can be chosen freely decreases due to the restrictions imposed when matching the physical properties and the lattice properties. For example, only two properties (grid spacing and time step) were selected freely in the fluctuation lattice Boltzmann model [176], where the authors matched mass density, temperature, and viscosity.

In the implementation of the parameter selection procedure based on physical properties, some problems may arise. Let's consider the following procedure to choose the lattice parameters in standard LBM without an external force. First, grid spacing Δx can be determined from the spatial resolution requirement, and then time step is obtained

from $\Delta t = \Delta x / \sqrt{3}\theta$, where θ is the physical sound speed $\theta = \sqrt{\frac{k_B T}{m}}$. After that,

dimensionless relaxation time τ is calculated by equating ν with ν :

$$\tau = \frac{\sqrt{3}\nu}{\theta\Delta x} + 0.5 \quad (107)$$

where the physical viscosity is

$$\nu = \frac{8\theta^2\lambda}{3\pi} \quad (108)$$

according to kinetic theory [126], and λ is the physical relaxation time, $\lambda = 1/\sigma n \langle v \rangle$ [126], where σ is the collision cross section, and n is the number density of the fluid particles. Apparently, only the grid spacing can be selected freely in this parameter selection procedure by using physical properties of the fluid. Now, two problems are

expected depending on the value of τ that is calculated from Eq. (107) because, as well known, τ must be in the range of (0.5,3.0) [147]. Firstly, if the viscosity is very small (which is the case for most gases under normal conditions), then τ is very close to 0.5 and the standard LBM schemes diverge. For example, for air at 1 atm and 300 K, ν is $1.8245 \times 10^{-5} \text{ m}^2/\text{s}$ and θ is 293.36 m/s . If the domain size is $1\text{m} \times 1\text{m}$ and a 128×128 grid is used, the grid spacing Δx is 0.0078125 m . In this case, τ is calculated as 0.500014 from Eq. (107), which causes LBM to diverge. Note that this lower limitation of τ is only applicable to the standard LBM. In the past 5-7 years, a newly developed entropic LBM [177, 178] eliminates the instability caused by small values of τ and the algorithm is stable with arbitrary small viscosities. Secondly, if the viscosity is very large (which is the case for a gas with low density and high temperature), LBM becomes very inaccurate. For instance, for air at 0.00001 atm and 1500 K , ν and θ are $20.399 \text{ m}^2/\text{s}$ and 655.97 m/s from kinetic theory, respectively, which lead to $\tau = 7.394$ with the same grid described above. This value falls outside the valid range of τ and generates a large simulation error.

The problem of having too large τ becomes aggravated in the simulation of weakly-ionized plasmas because a low degree of ionization and the corresponding low electron temperature of weakly-ionized plasmas lead to a large relaxation time and subsequently result in a large value of τ . For an example, an electron free diffusion problem is simulated by using the LBM model described in the previous section. In this simulation, a helium plasma with 1% degree of ionization in a $3.71 \times 3.71 \text{ mm}^2$ domain is considered, and a 256×256 grid is used. The number densities of three species are set as

$n_e = n_i = 10^{16} (m^{-3})$ and $n_n = 10^{18} (m^{-3})$. Then the temperature of electrons is calculated as 0.8008 eV according to the Saha equation [129]:

$$\frac{n_e}{n_n} \approx 3.00 \times 10^{27} T_e^{3/2} \frac{1}{n_e} \exp\left(-\frac{U_i}{T}\right) \quad (109)$$

where U_i is the first ionization energy of helium ($U_i = 24.59$ eV) and T_e is electron temperature in eV. By using the above physical parameters of the plasma, the dimensionless relaxation time τ is calculated as about 1.034×10^6 according to Eq. (107). The initial distribution of the electron number density is in the following Gaussian distribution:

$$n_e(\mathbf{x}, t = 0) = n_{e0} \left(1 + 0.01 \exp\left[-\frac{(x-x_c)^2 + (y-y_c)^2}{r^2}\right] \right) \quad (110)$$

where $r = 0.290$ mm and (x_c, y_c) represents the center point of the computational domain.

This free diffusion problem can be described by the Fick's law:

$$\frac{\partial n_e}{\partial t} = D_{en} \nabla^2 n_e \quad (111)$$

where D_{en} is the diffusivity of electrons due to the elastic collisions between electron and neutral and it is calculated as [154]:

$$D_{en} = \frac{8\theta_e^2 \lambda_{en}}{3\pi} \quad (112)$$

It is easy to find the analytical solution of Eq. (111):

$$n_e(x, y, t) = n_{e0} + \frac{0.01 n_{e0}}{(1+t/t_0)} \exp\left[-\frac{(x-x_c)^2 + (y-y_c)^2}{r^2(1+t/t_0)}\right] \quad (113)$$

where $t_0 = r^2/4D_{en}$.

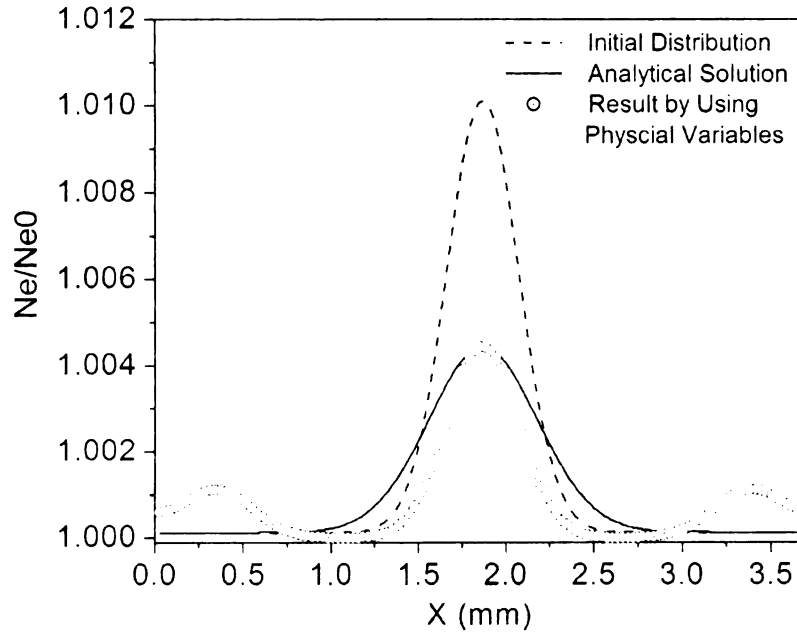


Figure 16 Distribution of electron number density at $t = 3.5$ ns. Non-physical peaks appear if the physical variables of electrons are used.

Figure 16 shows the distribution of electron number density at $t = 3.5$ ns obtained from Eq. (113) and from the simulation. Clearly, by using the physical variables, the result is very inaccurate and non-physical peaks appear in the solution. The appearance of these non-physical peaks can be explained as follows. In the case of electrons, the large non-dimensional relaxation time leads to a near-zero collision term in the lattice Boltzmann equation, and therefore, the effect of collision step is almost negligible. In other words, virtually only the streaming step is left in the implementation of LBM.

Figure 17 shows the electron number densities at two time moments with different ionization degrees. It can be seen that the sub-peaks move with the constant lattice speeds and the magnitudes do not change. We can also see that the sub-peaks of higher ionization degree move faster than those of lower ionization degree because the sound

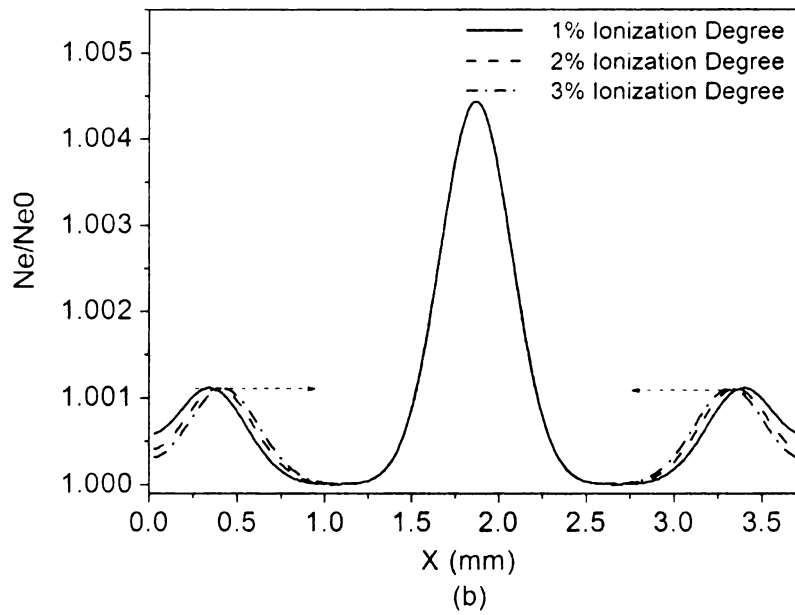
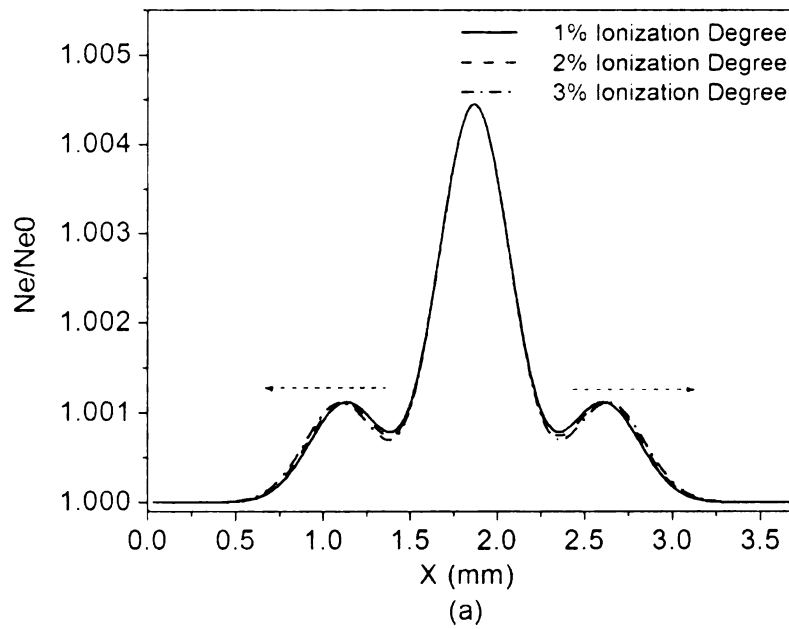


Figure 17 Electron number density distribution at (a) $t = 1.116$ ns and (b) $t = 3.347$ ns with different ionization degrees. Non-physical sub-peaks caused by using the physical variables travel with the constant lattice speed. A higher ionization degree leads to a higher lattice speed. The ratio of the magnitude of the sub-peaks to that of the primary peak corresponds to the value of the ratio of the weight coefficients.

speed is higher in the former case. The magnitudes of all three sub-peaks are also checked: the ratio of the magnitude of a sub-peak to that of the primary peak is 1:4, which is the ratio of weight coefficients in the D2Q9 model employed in this study. Figure 18 is the contour plot of electron number density at $t = 1.116$ ns. The dashed lines in the plot represent the discretized phase space and the particles stream to their neighboring nodes along the directions denoted by the numbers. The numbers in the brackets are the weight coefficients used in the discretization of the equilibrium distribution function. Figure 18 clearly illustrates the evolution of the electron number density along with the vector directions in the discretized phase space if the LBM simulation was conducted without the collision step.

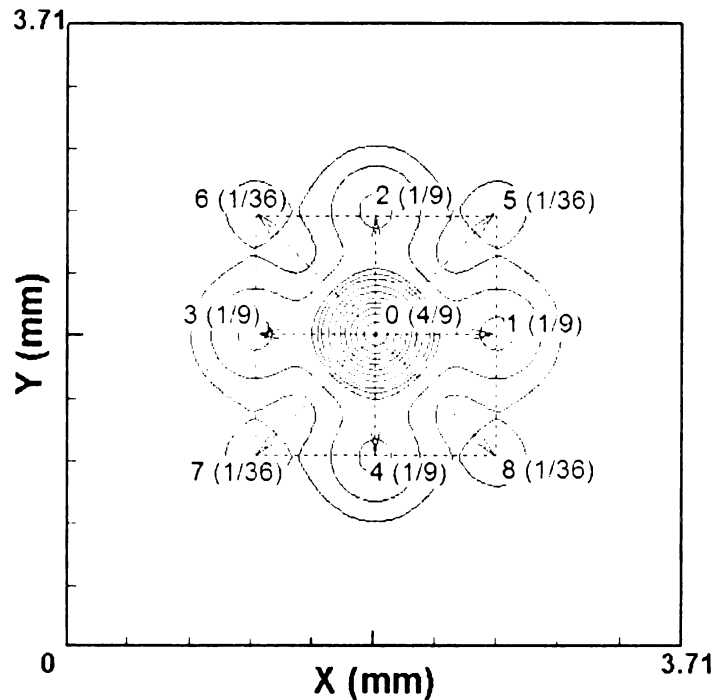


Figure 18 Contour plot of electron number density at $t = 1.116$ ns. The distribution of electrons is along with the discretized velocity directions if the effects of collisions are not included in LBM.

In conclusion, the usage of physical properties of the fluid will probably deduce an invalid value of the dimensionless relaxation time and thus lead to large simulation errors. To overcome this problem, a rescaling scheme is presented in this research that can be used with physical properties of fluids for a wide range of particle number density in the simulation of fluid flows and weakly-ionized plasmas. The key idea is to design a scheme in such a way that the kinematic viscosity of the fluid and the characteristic velocity due to the external force are matched in the implementation of LBM because, after all, the Boltzmann transport equation solves convection diffusion problems.

First of all, to preserve the diffusion characteristic of the problem, it is assumed that the lattice kinematic viscosity $\tilde{\nu}$ (Eq. (48)) is identical to the real kinematic viscosity ν (Eq. (108)). Then the lattice sound speed $\tilde{\theta}$ can be calculated as:

$$\tilde{\theta} = \frac{8\theta^2\lambda}{\sqrt{3\pi\Delta x(\tau - 0.5)}} \quad (114)$$

From Eq. (114) the rescaling parameter γ is obtained as:

$$\gamma \equiv \frac{\theta}{\tilde{\theta}} = \frac{\sqrt{3\pi\Delta x(\tau - 0.5)}}{8\theta\lambda} \quad (115)$$

Then the lattice sound speed is expressed as a function of the rescaling parameter as follows:

$$\tilde{\theta} = \frac{\theta}{\gamma} \quad (116)$$

Note that the rescaling parameter γ is a function of Δx , λ and θ , and therefore is fixed once the type and condition of fluid (λ and θ) and grid spacing (Δx) are determined.

Next, the lattice relaxation time $\tilde{\lambda}$ is determined from the dimensionless relaxation time,

$\tilde{\lambda} = \tau dt$, where the time step is $\Delta t = \Delta x / \sqrt{3}\tilde{\theta}$. Using Eq. (115), the lattice relaxation time $\tilde{\lambda}$ is calculated as follows:

$$\tilde{\lambda} = \frac{8\tau\gamma^2}{3\pi(\tau - 0.5)} \lambda \quad (117)$$

Secondly, the convective property of the flow when an external force exists must not be altered by the LBM scheme. If the flow is affected by an external force (such as an electromagnetic force), depending on the nature of the force we may need another rescaling to obtain accurate velocity fields. So, we propose the second rescaling rule: the characteristic velocity of the flow should not be changed by the rescaling, i.e.,

$$\mathbf{U}_0 = \tilde{\mathbf{U}}_0 \quad (118)$$

where \mathbf{U}_0 is the characteristic velocity of the flow. From this rule, we can obtain the rescaled acceleration $\tilde{\mathbf{a}}$, which we call the lattice acceleration in this article.

As mentioned earlier, dimensionless relaxation time τ and grid spacing Δx are the two parameters that can be chosen freely in this rescaling scheme. Once Δx is determined, τ can be selected considering the Mach number (Ma) and the Reynolds number (Re) of the problem. The following equation is the relationship between the Re and Ma obtained from the definition of Re:

$$\text{Re} = \frac{\sqrt{3}\text{Ma}N}{\tau - 0.5} \quad (119)$$

where N is the number of grid points along the characteristic length L_0 ; $\text{Ma} = U_0 / \tilde{\theta}$,

where U_0 is the magnitude of the characteristic velocity. From Eq. (119), we obtain:

$$\tau = \frac{\sqrt{3}\text{Ma}N}{\text{Re}} + 0.5 \quad (120)$$

which must lie in the valid range. Note that according to Hou *et al.* [135], there exists a critical value of τ below which simulation results show unphysical patterns or the code diverges even though τ is greater than 0.5. Eq. (120) is especially useful when the fluid flow is characterized by the Reynolds number, such as driven cavity flow. Given Ma and Re, τ can be determined from Eq. (120). Also, the Mach number of the problem must be small enough to meet the low Ma requirement. In the mean time, as will be shown later, LBM converges faster with a higher τ .

In cases where Re is not important or is hard to be defined, the definition of Ma can be used to choose τ :

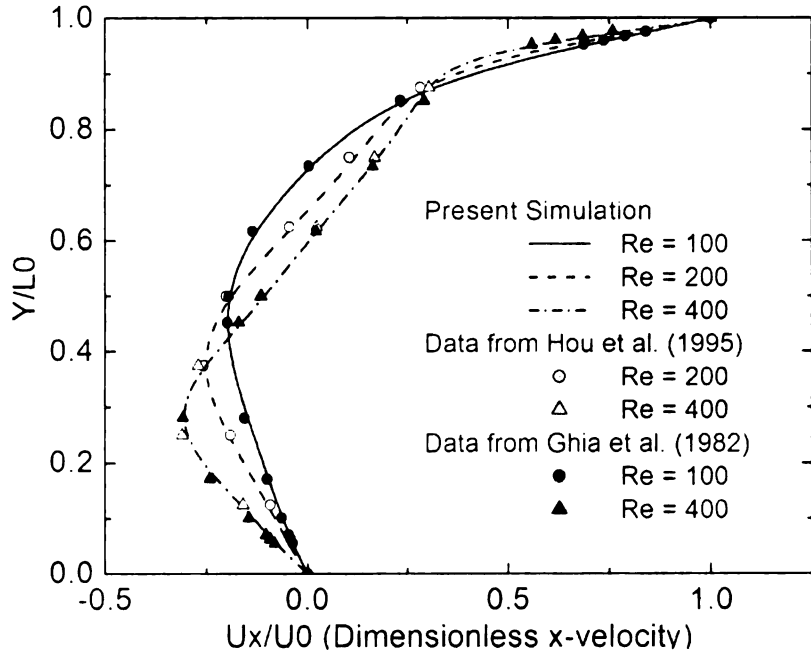
$$\text{Ma} = \frac{\sqrt{3}\pi\Delta x U_0(\tau - 0.5)}{8\theta^2\lambda} \quad (121)$$

from which the following is obtained:

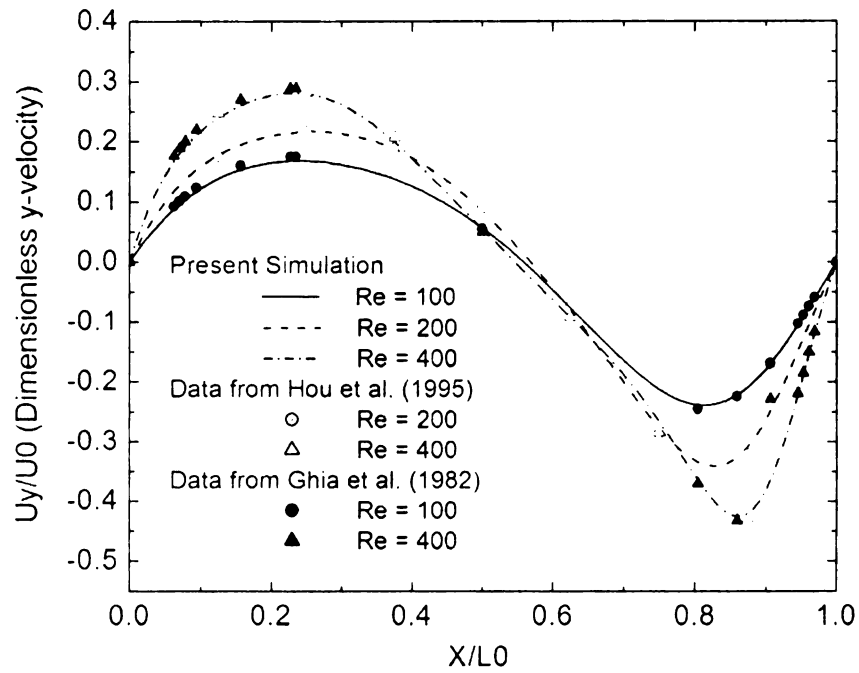
$$\tau = \frac{8\theta^2\lambda\text{Ma}}{\sqrt{3}\pi\Delta x U_0} + 0.5 \quad (122)$$

In the practical implementation of this rescaling scheme, the first step is to determine the grid spacing Δx and the dimensionless relaxation time τ (following the method described above) and then the rescaling parameter γ according to Eq. (115) with physical properties of a fluid. Then the lattice sound speed $\tilde{\theta}$ and the lattice acceleration $\tilde{\mathbf{a}}$ are determined from Eqs. (116) and (118), respectively. Once these lattice parameters are obtained, the remaining steps are same as the standard LBM.

To validate the present rescaling scheme, the two-dimensional driven cavity flow is simulated with and without the rescaling. In this flow problem, no external force appears in the lattice Boltzmann equation, and therefore, only the first rescaling rule is



(a)



(b)

Figure 19 Velocity profiles along the central lines of the computational domain obtained by using the physical properties of air without the rescaling when the dimensionless relaxation time is in the valid range. (a) dimensionless x -velocity (b) dimensionless y -velocity

employed to obtain the lattice sound speed and the acceleration is not rescaled. The cavity is $1\text{m}\times 1\text{m}$ in size and a 128×128 grid is used. We terminated the computation when the maximum relative error of the distribution function between two successive time steps is less than 1×10^{-6} .

Firstly, air at 300 K and 0.0001 atm is considered. At this state, kinematic viscosity ν is $0.18245\text{ m}^2/\text{s}$ and the dimensionless relaxation time from Eq. (107) is $\tau = 0.638$, which happens to fall in the valid range of τ . Therefore, this problem can be simulated with this physical τ value. Note that if τ calculated from Eq. (107) is used, γ becomes 1 and no rescaling takes place for the sound speed. In Figure 19, the velocity profiles along the central lines of the computational domain are compared with the data from [135] and [179]. Apparently, the simulation results agree with the results in [135] and [179] very well. As expected, if the dimensionless relaxation time is valid, LBM can be used with physical properties of air without the rescaling.

	$\tau = 0.6$	$\tau = 0.638$	$\tau = 0.8$	$\tau = 1.0$
γ	0.7252	1.0	2.1757	3.6262
Re	400	400	400	400
Ma	0.1804	0.2490	0.5413	0.9021
Error in u_x (%)	0.27	1.53	3.08	6.58
Error in u_y (%)	0.99	1.42	2.56	7.28

Table 5 Simulation parameters and simulation errors for different values of τ in the simulation of two-dimensional driven cavity flows

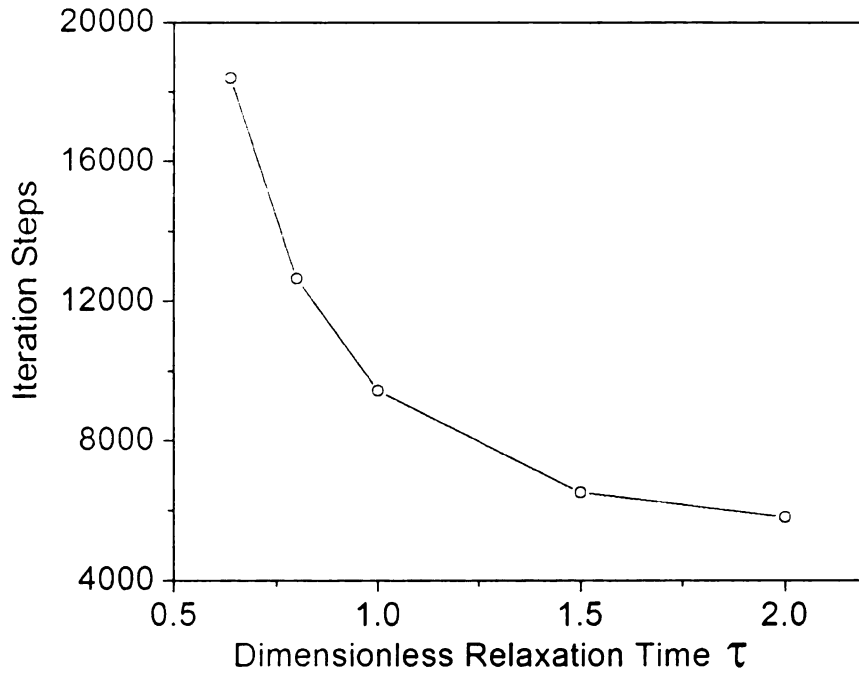


Figure 20 Number of iterations until convergence vs. τ (Re = 200). A larger τ leads to a quicker convergence.

Now, the same problem (Re = 400) is simulated by using the presented rescaling scheme. In this example, we select four different values of τ using Eq. (122) and the corresponding values of γ are presented in Table 5. The errors in u_x and u_y , listed in Table 5 are the maximum relative errors with respect to the results in [179]. Note that as mentioned earlier no rescaling takes place when $\tau = 0.638$. As seen from Table 5, this scheme gives reasonably good results for small values of τ but as τ increases this method becomes more inaccurate. This increase in error with increasing τ can be explained by Eq. (119): at fixed Re, a higher value of τ leads to a higher Ma. Because the standard LBM is formulated based on the low Ma assumption, a higher Ma tends to make the algorithm less accurate. On the other hand, as seen in Figure 20, the code

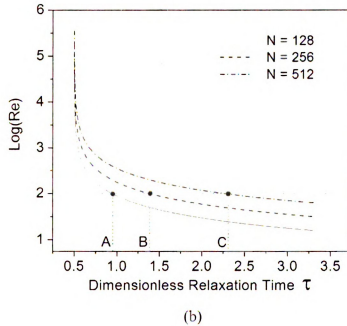
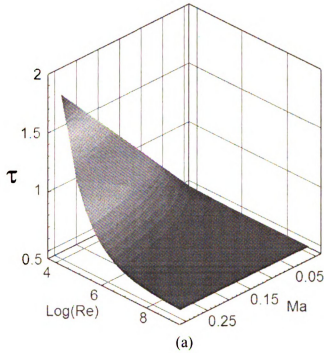


Figure 21 (a) τ as a function of Re and Ma ($N=128$). It is apparent that τ needs to be close to 0.5 if a high Ma and/or a high Re are desired. (b) Re vs. τ at different grid densities. Increasing grid density is an effective way to increase Re if the other simulation parameters are kept unchanged.

converges faster as τ increases. In Figure 21 (a), the dimensionless relaxation time τ is plotted as a function of Re and Ma (when $N = 128$) following Eq. (120); Figure 21 (b) presents the relationship between τ and Re at three different grid densities when Ma is chosen to be 0.2. The points marked by A, B and C are the dimensionless relaxation times calculated from Eq. (120) when Re=100. At such condition, the dimensionless relaxation times for N=128, 256 and 512 are found to be 0.943, 1.387 and 2.274, respectively.

	$T(K)$	$p(atm)$	$\nu(m^2/s)$	τ	Ma	Re	Result
Case 1	300	1	1.8245×10^{-5}	0.500014	1.24×10^{-4}	200	Unstable
Case 2	1500	1×10^{-5}	20.399	7.394	6.22	200	Unstable

Table 6 Two examples of the air state that give invalid dimensionless relaxation time

	Re	Ma	τ	γ	# of iterations
Case 1	200	9.021×10^{-2}	0.6	7252.43	20380
Case 2	200	9.021×10^{-2}	0.6	1.45×10^{-2}	20380

Table 7 Rescaled simulation parameters and # of iterations until convergence

Re	Ma	τ	γ
100	0.1	0.72	15955.35
200	0.0902	0.6	7252.43
500	0.113	0.55	3626.22
1000	0.113	0.525	1813.11
2000	0.225	0.525	1813.11
5000	0.564	0.525	1813.11

Table 8 Simulation parameters for air at 300 K and 1 atm (Case 1)

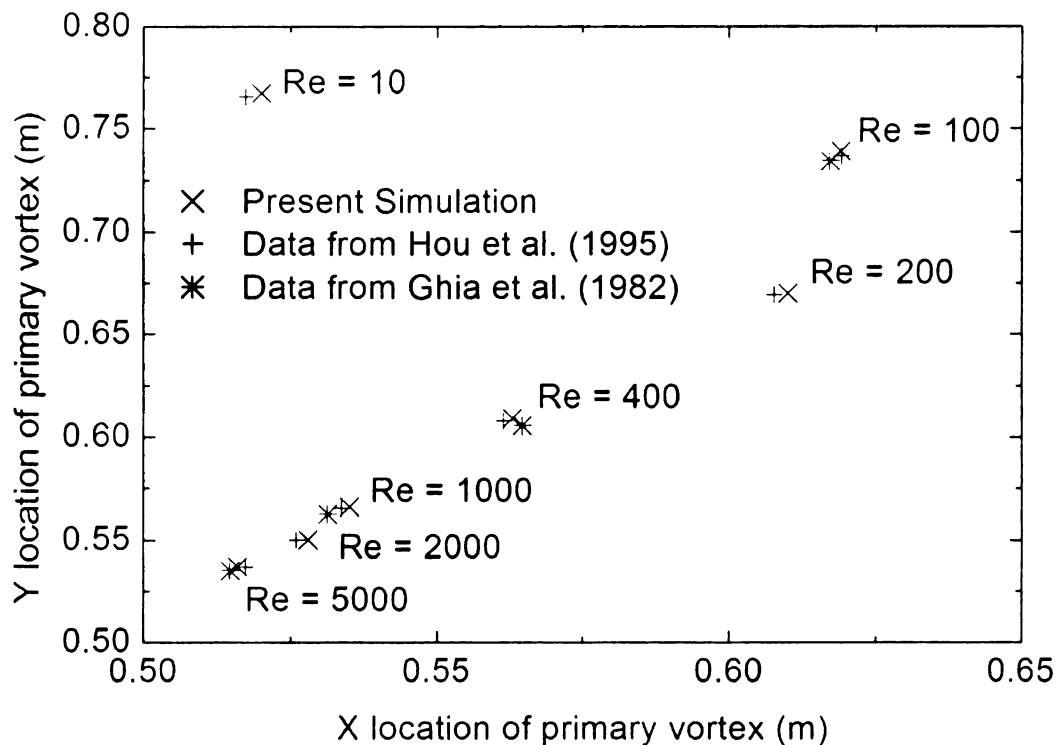
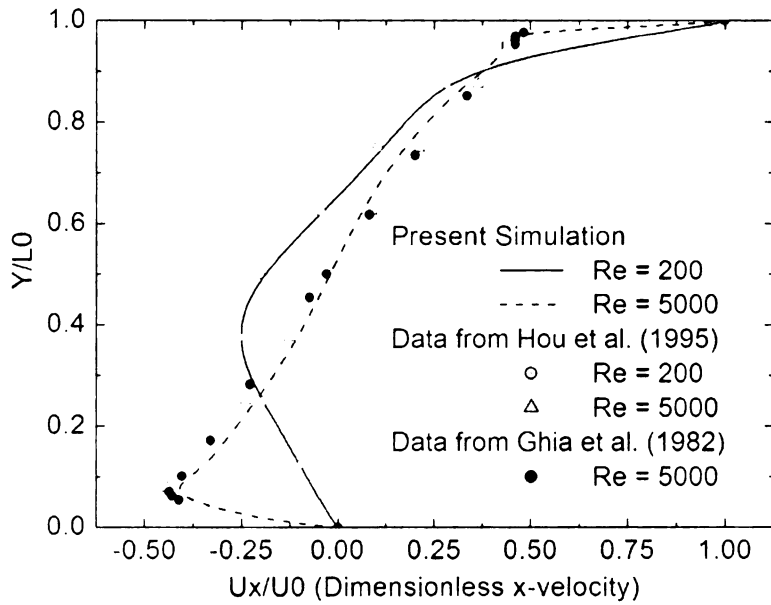
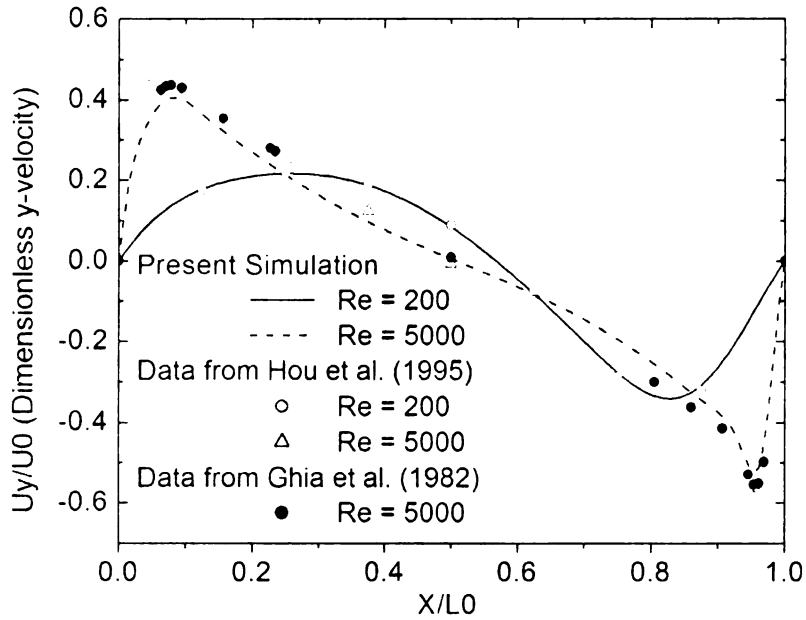


Figure 22 Locations of the primary vortices at different Reynolds numbers. The simulation results obtained by the rescaling scheme agree well with other researchers' results.

To show the capabilities of the rescaling scheme, the driven cavity flow is now simulated for two different conditions of air, under which the dimensionless relaxation times that satisfy Eq. (107) are outside the valid range. Table 6 shows the properties of air, and Re is selected to be 200 for both cases. As expected, LBM fails in both cases without the rescaling. However, both cases are simulated correctly by using the rescaling scheme. Table 6 lists the parameters used in the simulations with the rescaling and the numbers of iterations until convergence. Note that Ma and τ are in the reasonable range. Next, we simulate the driven cavity flow problem at several different Re using the properties used in Case 1 (in Table 6) with the rescaling. The main simulation parameters are listed in Table 7. Figure 22 presents the locations of the primary vortices at different Re , and Figure 23 shows the velocity profiles along the central lines at two different Reynolds numbers (200, 5000). As seen, the flow patterns are in good agreement with the ones shown in [135] and [179]. In Figure 23, we can see that the error at $Re = 5000$ is relatively large, which can be explained by the high Ma ($Ma = 0.564$) resulting from $Re = 5000$ and $\tau = 0.525$ as shown in Table 7. According to Eq. (119), there are two ways to reduce the Ma when Re is large. One way is to decrease τ . But unfortunately, there is a lower limit of τ due to the nature of LBM. The closer the value of τ is to 0.5, the more likely the code will be unstable. The other way is to increase the grid density for the simulation. This is the most straightforward way to solve this problem in a moderate range of Re but of course will increase the computational expense. Besides these two methods, there is another way to reduce Ma , i.e., the use of an interpolation scheme after the collision-streaming steps in LBM [180].



(a)



(b)

Figure 23 Velocity profiles along the central lines of the computational domain (a) dimensionless x-velocity (b) dimensionless y-velocity. The simulation errors are relatively large if the Reynolds number is high. It is due to the high Mach number resulted by the high Reynolds number according to Eq. (119).

4.3 Simulation Results

To illustrate the capability of the present LBM model with the rescaling scheme, two problems of weakly ionized helium plasma are simulated here. First, we simulate the electron diffusion problem under an externally applied electric field by neglecting the internally generated electric field because, in this case, the analytical solution is available. The details on the problem, such as domain size and grid density, are identical with those in Section 4.1. If the initial electron distribution is Gaussian and the maximum degree of ionization is 1%, the temporal and spatial distribution of the electron number density is calculated analytically as:

$$n_e^A(x, y, t) = \frac{0.01n_{n0}}{(1+t/t_0)} \exp\left[-\frac{(x-x_c - v_d t)^2 + (y-y_c)^2}{r^2(1+t/t_0)}\right] \quad (123)$$

where r and t_0 have the same definitions and values as in Eqs. (110) and (113). The electron diffusivity can be calculated by Eq. (112). In Eq. (123), v_d is the magnitude of the electron drift velocity \mathbf{v}_d due to the external electric field, which is calculated as follows [154]:

$$\mathbf{v}_d = -\frac{e\mathbf{E}_0}{m_e} \lambda_{en} = \mathbf{a}_e \lambda_{en} \quad (124)$$

In this problem, the second rule must be applied to rescale the acceleration term. Because the drift velocity is the characteristic velocity due to the electric field in this case, i.e., $\mathbf{U}_0 = \mathbf{v}_d$, from Eq. (118) and Eq. (124) the following equation can be obtained:

$$\mathbf{a}_e \lambda_{en} = \tilde{\mathbf{a}}_e \tilde{\lambda}_{en} \quad (125)$$

from which the acceleration due to the external force is rescaled as follows:

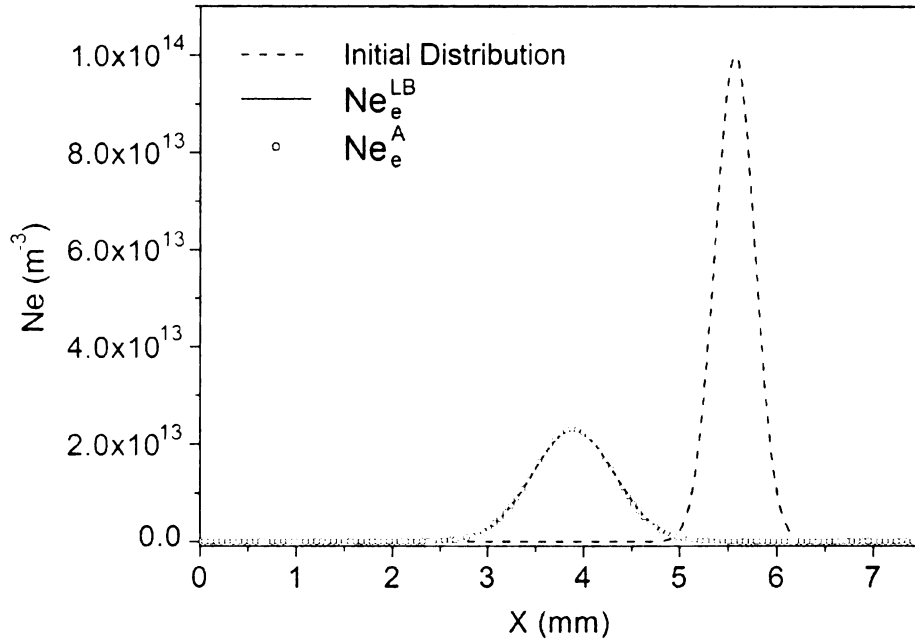
$$\tilde{\mathbf{a}}_e = \frac{3\pi(\tau - 0.5)}{8\tau\gamma^2} \mathbf{a}_e \quad (126)$$

where Eq. (117) is used to replace $\tilde{\lambda}_{en}$.

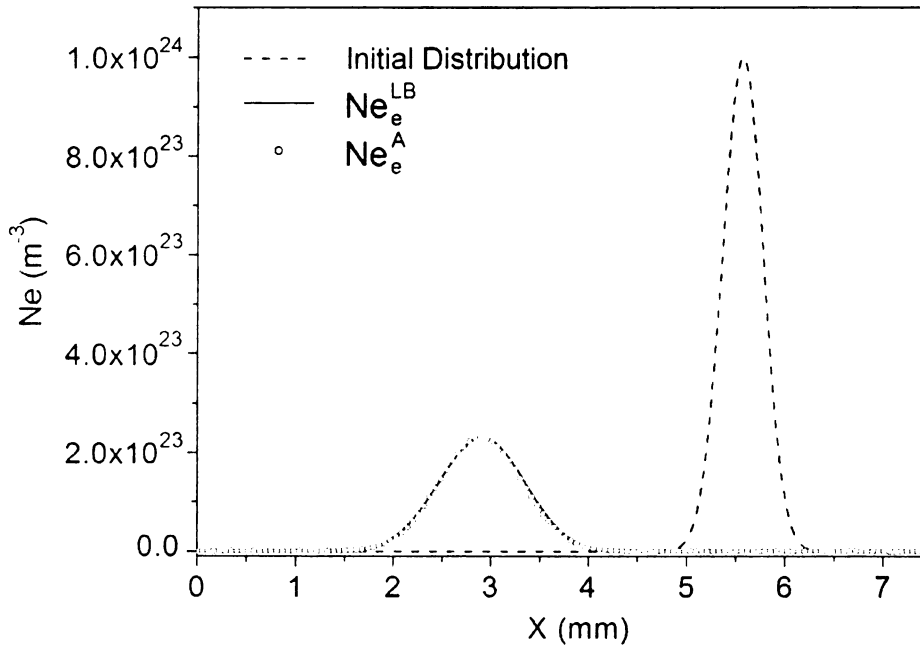
$n_{n0}(m^{-3})$	$T_e(eV)$	τ	γ	$E_0(V/m)$	error
1×10^{16}	0.7005	1.5	9.686×10^{-9}	14226.72	2.815×10^{-8}
1×10^{18}	0.8008	1.5	9.686×10^{-7}	16270.90	3.465×10^{-8}
1×10^{20}	0.9343	1.5	9.686×10^{-5}	18975.84	2.815×10^{-8}
1×10^{22}	1.1186	1.5	9.686×10^{-3}	22731.20	2.817×10^{-8}
1×10^{24}	1.3891	1.5	0.9686	28288.26	2.825×10^{-8}
1×10^{26}	1.820	1.5	96.86	58822.30	5.360×10^{-8}

Table 9 Simulation parameters used for the electron diffusion problem

Table 9 lists neutral number density (n_{n0}), electron temperature (T_e) and other parameters used for the simulation. Here, T_e is obtained from the Saha equation [129] corresponding to the 1% ionization degree and the electric field \mathbf{E}_0 directs from left to right. The dimensionless relaxation time τ is set 1.5 for all the calculations. In this research, a wide range of neutral number density (from 1×10^{16} to $1 \times 10^{26} \text{ m}^{-3}$) is considered. In Figure 24, electron number density distributions at later times are plotted together with the analytical solution (Eq. (123)) for two different neutral number density values (1×10^{16} and $1 \times 10^{26} \text{ m}^{-3}$). The simulation errors for six different initial number density values are listed in Table 9 using the following formula [181]:



(a) $n_{n0} = 1 \times 10^{16} m^{-3}$ at $t = 2.31 \times 10^{-16} s$



(b) $n_{n0} = 1 \times 10^{26} m^{-3}$ at $t = 1.433 \times 10^{-6} s$

Figure 24 Electron number density distributions with different initial number densities of neutrals. The simulation results obtained by the rescaling scheme are in good agreement with the analytical solutions.

$$\text{error} = \sqrt{\sum_{i,j} \left[\frac{n_e^{LB}(i,j,t) - n_e^A(x_i, y_j, t)}{n_e^A(i,j,t)} \right]^2} / mn \quad (127)$$

where m and n are numbers of grid points in x and y directions, respectively; $n_e^{LB}(i, j, t)$ is the electron number density at node point (i, j) obtained by the simulation; and $n_e^A(x_i, y_j, t)$ is the electron number density at the corresponding space point by Eq. (123). As clearly shown from Figure 24 and Table 9, the presented LBM model and the rescaling scheme give good results for the electron diffusion problem for a wide range of electron number density.

Next, the electron diffusion problem is simulated again by taking into account the internal electric field generated by the charge density. The computational domain as well as the grid density is the same as before. The initial number densities of the heavy particles are uniform in the space while the initial distribution of the electron number density is in the Gaussian form as shown in Eq. (110). The initial neutral number density of $n_{n0} = 1 \times 10^{18} m^{-3}$ and 1% ionization degree are considered in this calculation. Figure 25 presents the effect of internal electric field on the diffusion process. In this case, the external electrical field is not applied and only the internally generated electric field is considered during the diffusion process. It can be seen that the diffusion process is enhanced since the internal electric field generates outward forces which make the electrons escape from the center quickly. The dynamics of electrons under both external and internal electric fields is also simulated. Figure 26 shows electron number density and ion number density at $t = 1.116$ ns. The dashed line in the plot represents the number density contours of ions while the solid line stands for electrons. Under the effects of the

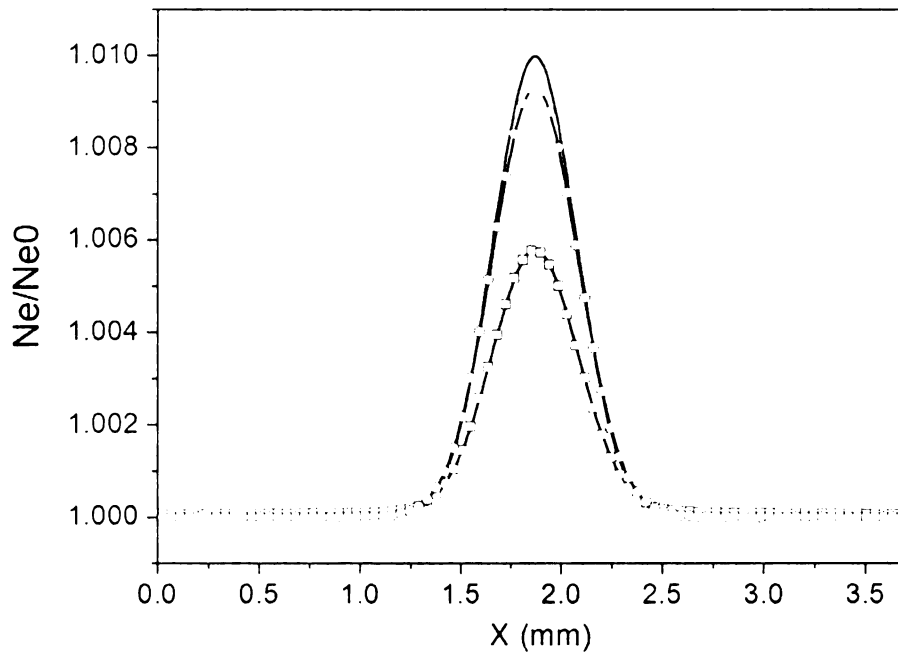


Figure 25 Electron number density distribution (Circle: without internal electric field, Squares: with internal electric field, both at 0.223 ns. Solid line shows the initial distribution). The internal electric field generated by the charge density largely enhances the electron diffusion process.

external applied electric field, the electrons will move along the inverse direction of the electric field. Note that the ions respond to the electric fields very slowly because they are much heavier than electrons and their temperature is much lower in this simulation. That is why the contour of ion number density seems to stay at its original position in the figure.

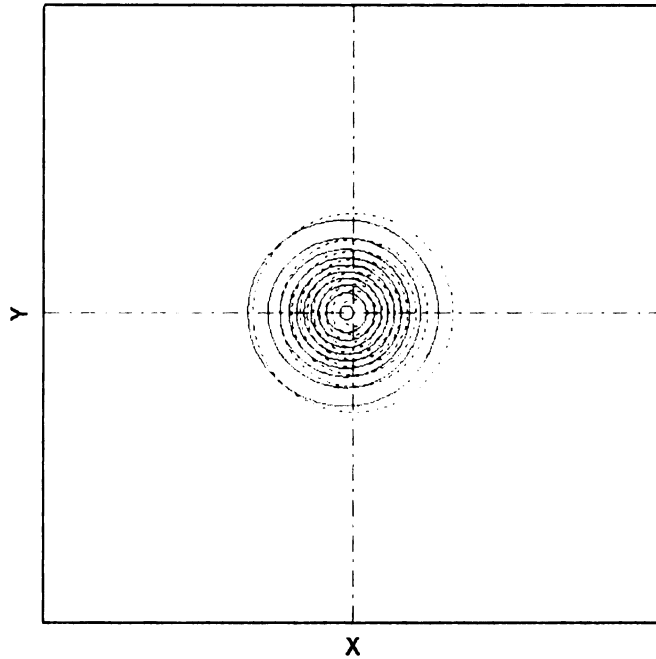


Figure 26 Snapshot of electron number density (solid lines) and ion number density (dashed lines) at $t = 1.116$ ns. The electrons and ions move along opposite directions because they have opposite charges. The ions travel much more slowly than the electrons since the ions have much heavier mass.

One thing to recall at this point is the fact that the external force in lattice Boltzmann equation (Eqs. (96) and (97)) is evaluated by using self-collision equilibrium distribution function (SCEDF) rather than cross-collision distribution function (CCEDF). To justify this we used both CCEDF and SCEDF for the same simulation and the results are shown in Figure 27 (without considering of the internal electric field). Since it is a simple convection-diffusion problem, the ratio n_e/n_{e0} cannot be smaller than 1. However, it is seen that when CCDEF is used the number density away from the peak can take values smaller than the initial value. As shown in Figure 27, the minimum value is roughly 0.9997, which means that the number density drops by about 3% of the initial

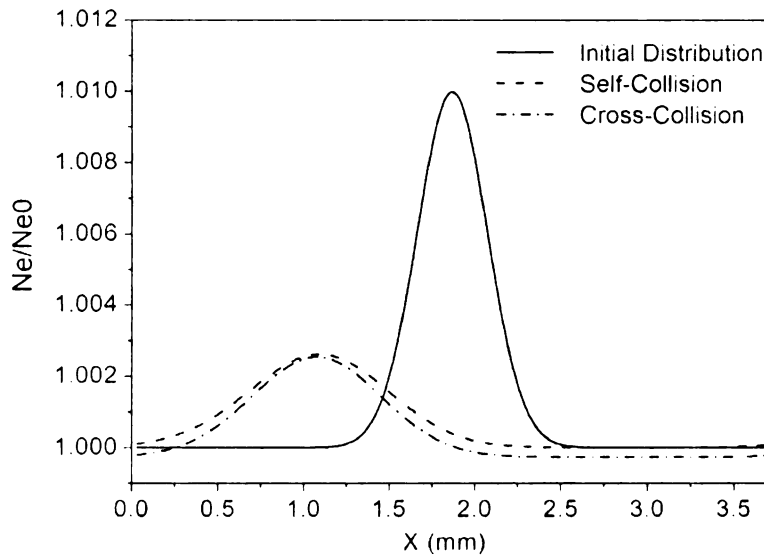


Figure 27 Electron number density distribution (at $t = 6.69$ ns) obtained by using different equilibrium distribution functions for the external force term. Apparent simulation errors would be resulted by using the cross-collision equilibrium distribution function in He's external force model.

perturbation of electron number density. On the other hand, physically realistic results were obtained with the used of SCEDF.

The grid independency and computational efficiency of the model are also studied by conducting the same simulation on three different grids (64×64 , 128×128 and 256×256). The error at time t was calculated by Eq. (127) (no internal electric field is considered). Figure 28 shows that, as expected, second order convergence is observed from the simulation results. In order to test the computational efficiency of the multi-component model, CPU times per time step are measured on a single-CPU PC for the present three-component model with the interpolation and a simple LBE model for electrons only. The electrostatic equation is not considered in the test. Test results show that the three-component model takes 4.07 times more CPU time than the electron-only model.

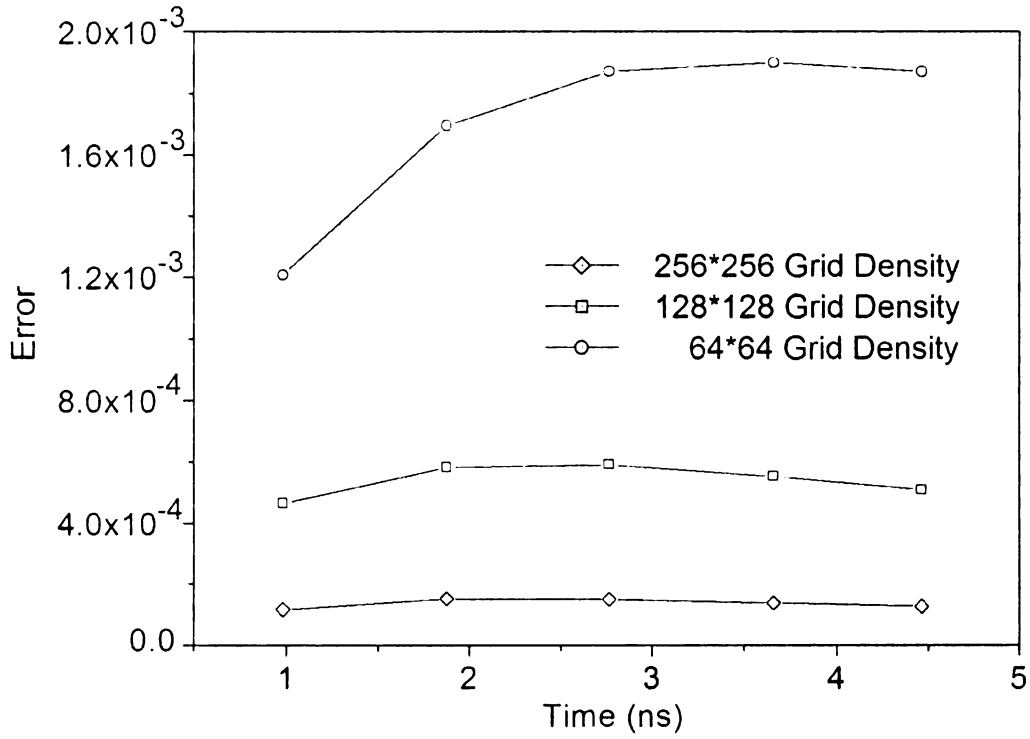


Figure 28 Relative errors in electron number density vs. time for three different grids. The errors are calculated at the center of the domain with comparison to the analytical solution. Second order accuracy in space discretization can be seen from the figure.

As a second validation of the model, we consider the electrostatic wave problem by neglecting all collision terms in Eqs. (96) to (98). If the collision term in the Boltzmann equation is neglected, the Boltzmann equation becomes the Vlasov equation for collisionless plasmas. The initial spatial distribution of electron number density is perturbed slightly as follows:

$$n_e(\mathbf{x}, t = 0) = n_{e0} \left(1 - 0.01 \cos \left(\frac{2\pi x}{l_x} \right) \right) \quad (128)$$

where l_x is the length of the physical domain (3.71 mm). The periodic boundary condition is employed for both the streaming step for the LBM and the Poisson equation

for the electric potential. For this problem, we used both with and without the rescaling. It is possible because all the collision terms are neglected. Figure 29 shows the evolution of electron number density and x -component velocity at the center point of the domain. It is clear that the results obtained with the rescaling scheme agree very well with the ones obtained using original variables. In addition, the wave period measured from the figure agrees well with the theoretical value of electron oscillation period ($2\pi / \omega_{pe}$ [129]). The maximum relative error between the theoretical and simulation results is 0.22 %. Therefore, both the standard LBM and the rescaled LBM can be used for the collisionless Vlasov equation.

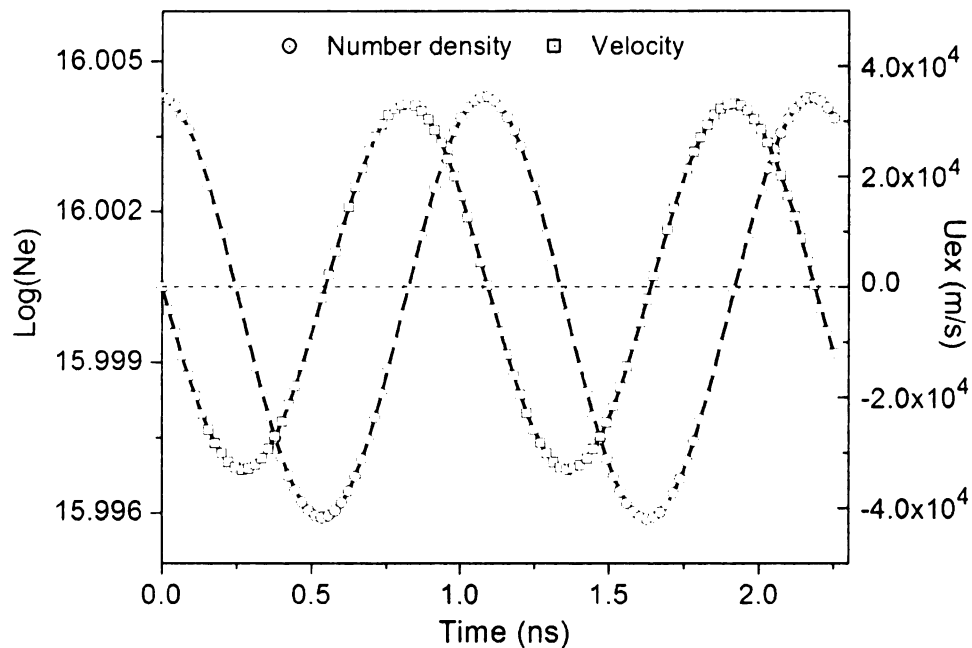


Figure 29 Time evolution of number density and x -component velocity of electrons at the center of the computational domain. (Solid lines: simulation results obtained without the rescaling scheme, circles and squares: simulation results obtained with the rescaling scheme)

In summary, a lattice Boltzmann method for weakly-ionized isothermal plasmas has been presented. A rescaling scheme has been proposed by which the LBM with an external force term can be used with physical properties of fluids, so that effects of collisions are taken into account correctly in LBM. This scheme only rescales the sound speed and the acceleration term due to external forces based on the following two rules: (1) the physical viscosity is equal to the lattice viscosity, and (2) the characteristic velocity due to the external force is not affected by the rescaling scheme. The 2D driven cavity flow is simulated to validate the rescaling scheme. Finally, the newly developed LBM model for weakly ionized plasmas with the rescaling scheme has been applied to simulate the electron diffusion problem and the electrostatic wave problem. Simulation results agree well with the data available in literature and the analytical solutions. Especially, this scheme can be applied to a wide range of number densities in plasma simulations.

Chapter 5

Lattice Boltzmann Simulation of Weakly Ionized Helium Plasma with Ionization and Recombination

A new LBM model is developed in this chapter to simulate laser interaction with weakly ionized plasmas. Comparing to the model proposed in the previous chapter, the present mode has the following features. First, ionization of neutral particles in the plasma and its inverse process, three-body recombination, have been taken into account in this model, which is achieved by adding an additional term in the Boltzmann equation; Secondly, the evolution of temperatures of the three species of particles are resolved by solving a set of energy equations derived directly from the Boltzmann transport equation; and thirdly, the Lorentz force is evaluated in this model as the external force term and the finite-difference time-domain (FDTD) method is adopted to solve the full set of Maxwell's equation to obtain the time- and space-dependent electromagnetic field. The interaction between a continuous laser beam and a weakly ionized helium plasma is simulated by using this newly developed model in this chapter. The preliminary results that show ionization and recombination dynamics of the weakly ionized plasma are presented following the detailed description of the model.

5.1 Mathematical Model

As the governing equations of the present model, the Boltzmann equations are listed based upon the following assumptions:

1) The plasma is weakly ionized. Therefore, the long range Coulomb interactions are not considered.

2) Only electrons at the outmost shell are ionized. Consequently, there are only three species of particles in the plasma: electrons, ions and neutrals.

3) Only electron impact ionization and three-body recombination are included in the present model. Other inelastic collisions, such as excitation, de-excitation, and charge attachment are neglected.

Based upon the above assumptions, the Boltzmann transport equations for electron, ions and neutrals in a weakly ionized plasma can be written as:

$$\frac{\partial f_e}{\partial t} + \mathbf{v}_e \cdot \nabla f_e = -\frac{f_e - f_{en}^{eq}}{\lambda_{en}} + R_e f_e^{eq} + \frac{\mathbf{a}_e \cdot (\mathbf{v}_e - \mathbf{u}_e)}{\theta_e^2} f_e^{eq} \quad (129)$$

$$\frac{\partial f_i}{\partial t} + \mathbf{v}_i \cdot \nabla f_i = -\frac{f_i - f_{in}^{eq}}{\lambda_{in}} + R_i f_i^{eq} + \frac{\mathbf{a}_i \cdot (\mathbf{v}_i - \mathbf{u}_i)}{\theta_i^2} f_i^{eq} \quad (130)$$

$$\frac{\partial f_n}{\partial t} + \mathbf{v}_n \cdot \nabla f_n = -\frac{f_n - f_{nn}^{eq}}{\lambda_{nn}} - R_n f_n^{eq} \quad (131)$$

where the external force term $\mathbf{a}_{e(i)} \cdot \nabla_{\mathbf{v}} f_{e(i)}$ has been evaluated by He's model as described in Chapter 3.

There are two main differences between the above Boltzmann equations and Eqs. (90) to (92). First, one term is added on the right hand side of the above equations to represent the rate of change of the particle distribution due to ionization of neutral particles and recombination of charged particles. In this model, only electron impact ionization and three-body recombination are considered. Then the physical ionization and recombination (IR) coefficient for electrons can be expressed as:

$$R_e = R_e^i - R_e^r \quad (132)$$

where R_e^i and R_e^r represent the electron impact ionization rate and the recombination rate, respectively. The electron impact ionization rate can be expressed as:

$$R_e^i = \sigma_i n_n \langle \bar{v}_e \rangle \quad (133)$$

where $\langle \bar{v}_e \rangle$ is the average value of the thermal speed of electrons and $\langle \bar{v}_e \rangle = \sqrt{8k_B T_e / \pi m_e}$ according to kinetic theory [126] and σ_i is the cross section of electron impact ionization which is dependent on the electron energy $m_e v_e^2 / 2$. The data of σ_i for helium as a function of electron energy can be found in many literatures [182-184]. For the three-body recombination, the formula in [185] is adopted in this simulation:

$$R_e^r = \frac{0.822 \times 10^{-33}}{T_e^{4.5}} n_e n_i \quad (134)$$

where the electron temperature T_e is in the unit of eV. Once R_e is calculated by Eqs.

(133) and (134), the IR coefficients of ions and neutrals can be found by $R_i = \frac{n_e}{n_i} R_e$ and

$R_n = \frac{n_e}{n_n} R_e$, respectively.

The second difference is the definition of the cross-collision equilibrium distribution function. f_{en}^{eq} is defined in this model as:

$$f_{en}^{eq} = \frac{n_e}{2\pi\theta_{en}^2} \exp\left[-\frac{(\mathbf{v}_e - \mathbf{u}_{en})^2}{2\theta_{en}^2}\right] \quad (135)$$

Comparing to Eq. (93), a new defined sound speed θ_{en} replaces the original electron sound speed:

$$\theta_{en} = \sqrt{\frac{k_B T_{en}}{m_e}} \quad (136)$$

where T_{en} is the electron temperature after elastic collisions with neutrals in the time period of λ_{en} . From the kinetic theory [126] and considering the ionization and recombination process, T_{en} can be found as:

$$T_{en} = T_e + \frac{2m_{en}(T_n - T_e)}{m_e + m_n} + \frac{m_n m_{en} (\mathbf{u}_n - \mathbf{u}_e)^2}{3k_B(m_e + m_n)} - \frac{2\lambda_{en} R_e U_i e}{3k_B} \quad (137)$$

where $m_{en} = \frac{m_e m_n}{m_e + m_n}$ is the reduced mass of electron and neutral, U_i is the first ionization potential of helium ($U_i = 24.59 eV$) and e is the unit electronic charge ($1e = 1.6 \times 10^{-19} C$). The T_{en} is adopted here because, to correctly describe the ionization and recombination dynamics, it is necessary to describe the post-collision states of the particles in the plasma, including both the self-collisions and cross-collisions. It can be seen later that the adoption of T_{en} in the equilibrium distribution function just describes the heat transfer between electrons and neutrals due to the collisions, which is significant for the energy evolutions between different species of particles in a system where the composing particles have far different properties. Similarly, the cross-collision equilibrium distribution function f_{in}^{eq} has the following definition:

$$f_{in}^{eq} = \frac{n_i}{2\pi\theta_{in}^2} \exp\left[-\frac{(\mathbf{v}_i - \mathbf{u}_{in})^2}{2\theta_{in}^2}\right] \quad (138)$$

where $\theta_{in} = \sqrt{\frac{k_B T_{in}}{m_i}}$ and T_{in} is calculated as:

$$T_{in} = T_i + \frac{2m_{in}(T_n - T_i)}{m_i + m_n} + \frac{m_n m_{in} (\mathbf{u}_n - \mathbf{u}_i)^2}{3k_B(m_i + m_n)} \quad (139)$$

where the reduced mass of ions and neutrals is $m_{in} = \frac{m_i m_n}{m_i + m_n}$. Note that there is no ionization term in the above equation. That is natural because there is no ionization happening during the collisions between ions and neutrals in the plasma.

The Boltzmann equations shown in Eqs. (129) to (131) can be discretized by the traditional D2Q9 scheme. However, in such a case, only particle number densities and momentums can be retrieved correctly from the lattice Boltzmann equation. Thus, a supplemental set of energy equations are included in this model to describe the heating patterns of the particles. Starting from the Boltzmann equation, the corresponding energy equation can be obtained by taking proper moments of the distribution functions with respect to the microscopic velocity. Taking electrons as the example, the distribution function f_e has the following property:

$$n_e \langle \chi(\mathbf{v}_e) \rangle = \int_{\mathbf{v}} \chi(\mathbf{v}_e) f_e d\mathbf{v}_e \quad (140)$$

where $\chi(\mathbf{v}_e)$ is a function only dependent on \mathbf{v}_e . By setting different expressions of $\chi(\mathbf{v}_e)$, we can have the following macroscopic quantities listed in Table 10. In Table 10, $\mathbf{c}_e = \mathbf{v}_e - \mathbf{u}_e$ is the random velocity of electron which is closely related to the temperature.

Multiplying $\chi(\mathbf{v}_e) = \frac{1}{2} m_e \mathbf{v}_e^2$ on every term in Eq. (129) and integrating each term with respect to \mathbf{v}_e from the negative infinity to positive infinity, we can get:

$$\begin{aligned}
\int_{\mathbf{v}} \chi(\mathbf{v}_e) \frac{\partial f_e}{\partial t} d\mathbf{v}_e + \int_{\mathbf{v}} \chi(\mathbf{v}_e) \mathbf{v}_e \cdot \nabla f_e d\mathbf{v}_e = & -\frac{1}{\lambda_{en}} \int_{\mathbf{v}} \chi(\mathbf{v}_e) (f_e - f_e^{eq}) d\mathbf{v}_e \\
& + R_e \int_{\mathbf{v}} \chi(\mathbf{v}_e) f_e^{eq} d\mathbf{v}_e + \frac{\mathbf{a}_e}{\theta_e^2} \cdot \int_{\mathbf{v}} \chi(\mathbf{v}_e) (\mathbf{v}_e - \mathbf{u}_e) f_e^{eq} d\mathbf{v}_e
\end{aligned} \tag{141}$$

Macroscopic Quantity	$\chi(\mathbf{v}_e)$	Expression
Number Density	1	$n_e = \int_{\mathbf{v}} f_e d\mathbf{v}_e$
Macroscopic Velocity	\mathbf{v}_e	$n_e \langle \mathbf{v}_e \rangle = \int_{\mathbf{v}} \mathbf{v}_e f_e d\mathbf{v}_e = n_e \mathbf{u}_e$
Kinetic Pressure Dyad	$\mathbf{c}_e \mathbf{c}_e$	$m_e n_e \langle \mathbf{c}_e \mathbf{c}_e \rangle = m_e \int_{\mathbf{v}} \mathbf{c}_e \mathbf{c}_e f_e d\mathbf{v}_e = \mathbf{P}_e$
Momentum Dyad	$\mathbf{v}_e \mathbf{v}_e$	$m_e n_e \langle \mathbf{v}_e \mathbf{v}_e \rangle = m_e \int_{\mathbf{v}} \mathbf{v}_e \mathbf{v}_e f_e d\mathbf{v}_e = \mathbf{P}_e + m_e n_e \mathbf{u}_e \mathbf{u}_e$
Temperature	$\frac{1}{2} m_e \mathbf{c}_e \cdot \mathbf{c}_e$	$n_e \left\langle \frac{1}{2} m_e \mathbf{c}_e^2 \right\rangle = \frac{1}{2} m_e \int_{\mathbf{v}} \mathbf{c}_e^2 f_e d\mathbf{v}_e = \frac{3}{2} n_e k_B T_e$
Total Energy	$\frac{1}{2} m_e \mathbf{v}_e \cdot \mathbf{v}_e$	$n_e \left\langle \frac{1}{2} m_e \mathbf{v}_e^2 \right\rangle = \frac{1}{2} m_e \int_{\mathbf{v}} \mathbf{v}_e^2 f_e d\mathbf{v}_e = \frac{3}{2} n_e k_B T_e + \frac{1}{2} m_e n_e \mathbf{u}_e^2$

Table 10 Macroscopic Quantities from Moments of Distribution Function

Using the expressions listed in Table 10 and following the similar derivation procedure in [129], we can finally find the energy equation of electrons as:

$$\begin{aligned} \frac{\partial \mathcal{E}_e}{\partial t} + \nabla \cdot (\varepsilon_e \mathbf{u}_e) = & -\nabla \cdot (\mathbf{P}_e \cdot \mathbf{u}_e) - \nabla \cdot \mathbf{q}_e + m_e n_e \mathbf{a}_e \cdot \mathbf{u}_e \\ & - \frac{3n_e k_B (T_e - T_{en})}{2\lambda_{en}} - \frac{m_e n_e}{2\lambda_{en}} (\mathbf{u}_e^2 - \mathbf{u}_{en}^2) + R_e \mathcal{E}_e \end{aligned} \quad (142)$$

where $\varepsilon_e = \frac{3}{2} n_e k_B T_e + \frac{1}{2} m_e n_e \mathbf{u}_e^2$ is the total energy of electrons; and \mathbf{q}_e is the electron

heat flux and $\mathbf{q}_e = -\kappa_e \nabla T_e$ where $\kappa_e = \frac{1}{2} n_e k_B \langle \bar{v}_e \rangle \lambda_{en}$ is the electron thermal

conductivity. Recalling that $\mathbf{a}_e = -\frac{e(\mathbf{E} + \mathbf{u}_e \times \mathbf{B})}{m_e}$ where \mathbf{E} and \mathbf{B} are the electric field

and magnetic field respectively, the third term on the right hand side of Eq. (142) can be rewritten as:

$$m_e n_e \mathbf{a}_e \cdot \mathbf{u}_e = -en_e (\mathbf{E} + \mathbf{u}_e \times \mathbf{B}) \cdot \mathbf{u}_e \quad (143)$$

Noting that $(\mathbf{u}_e \times \mathbf{B}) \cdot \mathbf{u}_e = 0$ and defining the electron current density as $\mathbf{J}_e = -en_e \mathbf{u}_e$, the above equation becomes:

$$m_e n_e \mathbf{a}_e \cdot \mathbf{u}_e = \mathbf{J}_e \cdot \mathbf{E} \quad (144)$$

which can be interpreted as the Joule heating term for electrons. Further, substituting T_{en} (Eq. (137)) into Eq. (142) and after some manipulations, the energy equation of electrons can be expressed as:

$$\begin{aligned} \frac{\partial \mathcal{E}_e}{\partial t} + \nabla \cdot (\varepsilon_e \mathbf{u}_e) = & -\nabla \cdot (\mathbf{P}_e \cdot \mathbf{u}_e) + \nabla \cdot (\kappa_e \nabla T_e) + \mathbf{J}_e \cdot \mathbf{E} \\ & - \frac{3k_B n_e m_{en} (T_e - T_n)}{\lambda_{en} (m_e + m_n)} + \frac{m_e n_e}{\lambda_{en}} \mathbf{u}_{en} \cdot (\mathbf{u}_{en} - \mathbf{u}_e) - R_e n_e U_1 e + R_e \mathcal{E}_e \end{aligned} \quad (145)$$

Similarly, the energy equations of ions and neutrals are:

$$\begin{aligned} \frac{\partial \varepsilon_i}{\partial t} + \nabla \cdot (\varepsilon_i \mathbf{u}_i) = & -\nabla \cdot (\mathbf{P}_i \cdot \mathbf{u}_i) + \nabla \cdot (\kappa_i \nabla T_i) + \mathbf{J}_i \cdot \mathbf{E} \\ & - \frac{3k_B n_i m_{in} (T_i - T_n)}{\lambda_{in} (m_i + m_n)} + \frac{m_i n_n}{\lambda_{in}} \mathbf{u}_{in} \cdot (\mathbf{u}_{in} - \mathbf{u}_i) + R_i \varepsilon_i \end{aligned} \quad (146)$$

and

$$\begin{aligned} \frac{\partial \varepsilon_n}{\partial t} + \nabla \cdot (\varepsilon_n \mathbf{u}_n) = & -\nabla \cdot (\mathbf{P}_n \cdot \mathbf{u}_n) + \nabla \cdot (\kappa_n \nabla T_e) \\ & + \frac{3k_B n_e m_{en} (T_e - T_n)}{\lambda_{en} (m_e + m_n)} + \frac{m_n n_e}{\lambda_{en}} \mathbf{u}_{en} \cdot (\mathbf{u}_{en} - \mathbf{u}_n) \\ & + \frac{3k_B n_i m_{in} (T_i - T_n)}{\lambda_{in} (m_i + m_n)} + \frac{m_n n_i}{\lambda_{in}} \mathbf{u}_{in} \cdot (\mathbf{u}_{in} - \mathbf{u}_n) + R_n \varepsilon_n \end{aligned} \quad (147)$$

Eqs. (145) to (147) constitute a full set of the energy equations of the three species of particles in a weakly ionized plasma. The temperatures can be solved from the above equations by using the hydrodynamics quantities calculated from the Boltzmann equations. However, evaluation of the Joule heating term in the energy equation as well as the external force term in the Boltzmann equation requires an accurate solution of the Maxwell's equations. In this model, the finite-difference time-domain (FDTD) is adopted to directly solve the full set of Maxwell's equations.

5.2 Finite-Difference Time-Domain Method

The external force term in the Boltzmann equation is generally the Lorentz force in plasma simulation. This external force essentially governs the dynamics of the individual species of charged particles and thereby influences the macroscopic quantities of the plasma. Inversely, the variation of charge density in the plasma affects the electromagnetic field which determines the Lorentz force together with the macroscopic velocities. Meanwhile, the Joule heating term in the energy equation can also be interpreted as the work done by the Lorentz force on the charged particle. Conclusively,

the most detailed information about the evolution of the electromagnetic field is needed so that the Lorentz force in LBM solver can be evaluated accurately. As the most exact governing equations for all electromagnetic phenomena, Maxwell's equations are solved directly in this research to obtain the field quantities. Maxwell's equations consist of the following four equations:

$$\nabla \cdot \mathbf{D} = \rho_v \quad (148)$$

$$\nabla \cdot \mathbf{B} = 0 \quad (149)$$

$$\nabla \times \mathbf{E} = -\frac{\partial \mathbf{B}}{\partial t} - \mathbf{M} \quad (150)$$

$$\nabla \times \mathbf{H} = \mathbf{J} + \frac{\partial \mathbf{D}}{\partial t} \quad (151)$$

where ρ_v is the free charge density, $\rho_v = e(n_i - n_e)$; \mathbf{J} is the electric current density, $\mathbf{J} = e(n_i \mathbf{u}_i - n_e \mathbf{u}_e)$; \mathbf{M} is the equivalent magnetic current density which is neglected in this study; \mathbf{E} is the electric field; \mathbf{H} is the magnetic field; \mathbf{D} is the electric flux density; and \mathbf{B} is the magnetic flux density.

To solve the Maxwell's equations, the finite-difference time-domain (FDTD) method [186] is adopted in this research. Figure 30 shows the positions of the electric and magnetic field vectors about a cubic unit cell of the Yee space lattice. This configuration ensures Eq. (149) to hold. Accordingly, the Maxwell's equations can be discretized by using the central-difference scheme upon both space and the time domain. The concrete expressions of discretized Maxwell's equations for different cases can be found in Taflove and Hagness's book [186]. Then the new value of an electromagnetic field vector component at any lattice point can be calculated from its previous value and the previous values of the components of the other field vector at adjacent points.

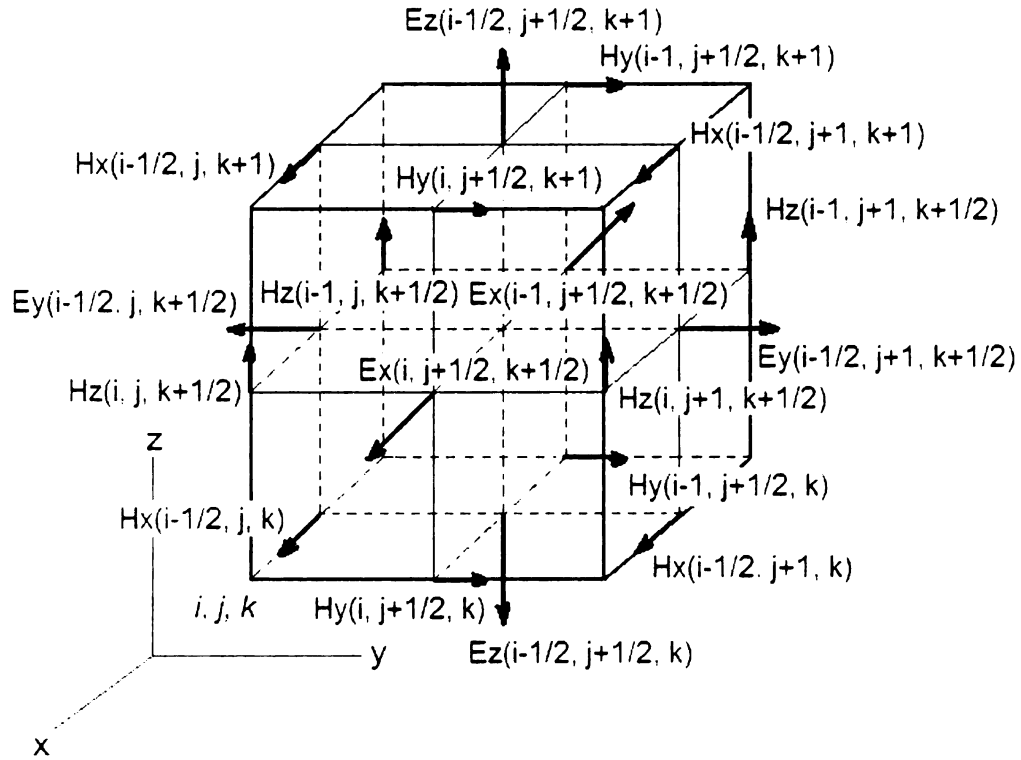


Figure 30 Position of the electric and magnetic field vector components about a cubic unit cell of the Yee space lattice

Since the electromagnetic waves in nature can reflect back into the computational domain at the computational boundaries, a proper boundary condition must be applied to terminate the computational domain if a physical problem with open boundaries is of interest, such as an electromagnetic wave propagation in an infinite medium. In order to eliminate the fake waves caused by the reflection of the incoming wave at the boundaries, Berenger introduced a highly effective absorbing boundary condition called the perfectly matched layer (PML) in 1994 [187]. However, this PML boundary condition is a hypothetical medium based on a mathematical model. Indeed, a physical model based on an anisotropic perfectly matched medium can be formulated. This was first discussed by Sacks *et al.* [188]. For a single interface, the anisotropic medium is uniaxial and is

composed of both electric and magnetic permittivity tensors. This kind of boundary condition is called UPML (uniaxial PML).

To illustrate the capabilities of FDTD for simulation of laser-plasma interaction, a femtosecond laser pulse interaction with a target silicon substrate is simulated here. The laser-induced ionization is included in this calculation by using an ionization model based upon local energy balance analysis of electrons at successive time steps. The current density is modeled by Ohm's law, i.e. $\mathbf{J} = \sigma \mathbf{E}$ where σ is the conductivity of silicon at a given point, in using the FDTD. A two-temperature model developed by Kaganov *et al.* [189] is used to calculate the heating pattern of the electrons and lattices in this simulation.

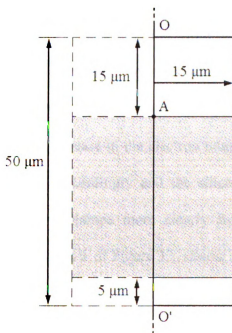
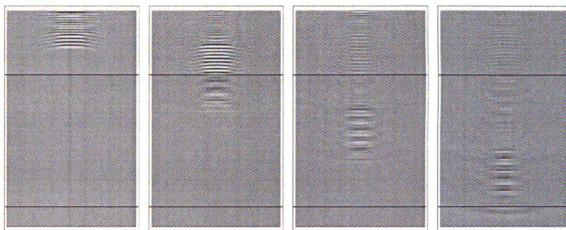


Figure 31 Schematic of computational domain for simulation of a femtosecond laser pulse interaction with a silicon substrate.

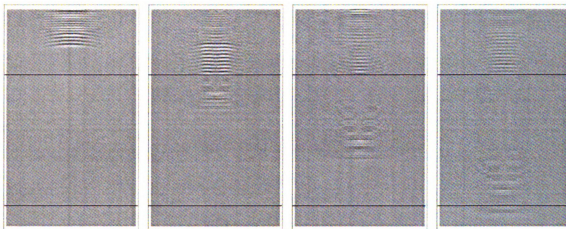
In this simulation, a femtosecond laser with the wavelength of 800 nm and the pulse width of 80 fs is used. The beam is assumed radially polarized (TEM₀₀ mode) and

is focused through a numerical lens located at the top of the computational domain. Four pulse energies (7.5 μJ , 15 μJ , 30 μJ and 60 μJ) are used for the calculation. The target silicon with the electrical conductivity of 1.4 Ω^{-1}/m is assumed. Figure 31 illustrates the computational domain used in this study.

Figure 32 and Figure 33 are the time histories of the radial component of the electric field (E_r) and the corresponding energy absorption patterns in the silicon substrate respectively. The pulse energy is 30 μJ ; and the pulse width is 80 fs. The top row in each figure shows the results obtained without the ionization model; and the bottom rows are the results after incorporating the developed ionization model. As shown clearly, the major difference is that the laser beam is blocked significantly near the interface when the ionization process is accounted for while the laser beam propagates through the silicon freely when the ionization is not considered. In fact, the laser pulse is blocked almost completely except near the rim of the laser pulse. This is because the ionization process leads to a sudden increase in the electron number density. As a result, the electrical conductivity increases accordingly and the silicon substrate can behave almost like a metal. This can be explained more clearly from the energy balance viewpoint. As illustrated in the bottom row of Figure 33, almost all the energy carried by the laser pulse is dissipated in a very thin layer near the interface due to the very high electron number density. The thickness of this energy absorption layer is called the skin depth (for metals) and it is believed to be closely related to the ablation thickness. As clearly seen from these figures, the thickness is very well defined even for a



(A) Without the ionization model



(B) With the ionization model

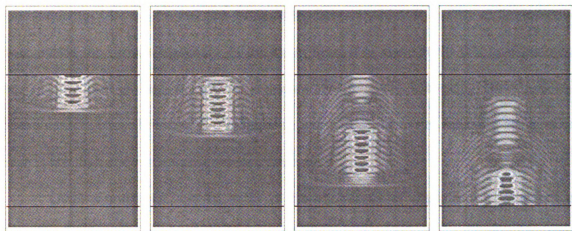
(1) $t = -11.6$ fs

(2) $t = 65.2$ fs

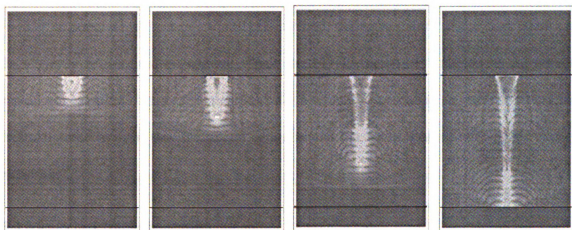
(3) $t = 140.2$ fs

(4) $t = 218.8$ fs

Figure 32 Time history of laser pulse propagation. (In these plots, the radial component of the electric field (E_r) is used.)



(A) Without the ionization model



(B) With the ionization model

(1) $t = 65.2$ fs

(2) $t = 103.6$ fs

(3) $t = 180.4$ fs

(4) $t = 257.2$ fs

Figure 33 Time history of laser energy absorbed by electrons

semiconductor like silicon and this explains the superior ablation quality of femtosecond laser pulses for various materials. In the mean time, it is also shown that near the outer rim of the laser pulse, the EM wave penetrates into the substrate. This “leaking” phenomenon occurs because, for a Gaussian laser beam, the laser intensity at the outer edge is not high enough to induce strong ionization.

Other simulations results, such as the evolutions of the electron temperature, electron number density, electrical conductivity and the absorption coefficient of the target silicon are also obtained through the simulation and they are discussed in detailed in [89]. In conclusion, by using the FDTD method, the wave nature of the laser beam can be retrieved to the greatest content. Thus, the FDTD method is adopted in the present model to calculate the electromagnetic field which is essential in evaluation of the external force term in the Boltzmann equation and the Joule heating term in the energy equation.

5.3 Numerical Implementation

In the practical implementation of the present LBM model to simulate laser interactions with weakly ionized plasmas, there are several points worthy to be noted numerically.

1) Selection of the time step. Because the present model is actually a hybrid model in which three sub-models involve, the time step should be selected as:

$$\Delta t = \min(\Delta t_{LBM}, \Delta t_{FDTD}, \Delta t_{ENG}) \quad (152)$$

where Δt_{LBM} is the time step determined merely by lattice Boltzmann method,

$$\Delta t_{LBM} = \frac{\Delta x}{\sqrt{3}\theta_{\max}} \quad (\text{where } \theta_{\max} \text{ denotes the maximum sound speed of the three different}$$

species of particles in the weakly ionized plasma and θ_{\max} is usually equal θ_e in the most cases); Δt_{FDTD} is time step merely decided by FDTD method, $\Delta t_{FDTD} \leq \frac{\Delta x}{c}$ (where c is the speed of light) and Δt_{ENG} is the time step required by the solution of the energy equation, $\Delta t_{ENG} \leq \frac{0.5C_e\Delta x^2}{\kappa_e}$, where C_e and κ_e are the volumetric heat capacity and thermal conductivity of electrons respectively. Through preliminary quantitative probe, we can find that Δt_{FDTD} is the usually the smallest one among the above three mentioned time steps. Thus, we choose the time step as:

$$\Delta t = \Delta t_{FDTD} = \frac{\Delta x}{\delta c} \quad (153)$$

where the constant $\delta \geq 2$ in our simulation without loss of generality.

2) Rescaling scheme. Although the basic idea of the rescaling scheme used in this model is the same as the one described in Chapter 4, there is a little difference in the practical implementation. Besides the two free parameters, the spacing Δx and the dimensionless relaxation time τ , there is another free parameter which can be prescribed here; that is, the time step Δt as described above. The lattice viscosity recovered from the LBM has the same form as before (taking the electrons as the example):

$$\tilde{\nu}_e = (\tau_e - 0.5)\tilde{\theta}_e^2\Delta t \quad (154)$$

where the time step is determined by Eq. (153). By equating the physical viscosity to the lattice viscosity, we can easily have:

$$\gamma_e = \sqrt{\frac{3\pi(\tau_e - 0.5)\Delta t}{8\lambda_{en}}} \quad (155)$$

following the same definition of the rescaling parameter γ as shown in Eq. (115). It can be seen that once the physical properties of the electron, the dimensionless relaxation time τ_e and the time step Δt are determined, the lattice sound speed of electrons can be determined accordingly as:

$$\tilde{\theta}_e = \frac{\theta_e}{\gamma_e} \quad (156)$$

The rescaling of the relaxation time λ_{en} is straightforward, i.e. $\tilde{\lambda}_{en} = \tau_e \Delta t$. Then the rescaled acceleration can be found as:

$$\tilde{\mathbf{a}}_e = \frac{\lambda_{en}}{\tilde{\lambda}_{en}} \mathbf{a}_e \quad (157)$$

according to the second rule of the rescaling scheme introduced in Chapter 4. The rescaled parameters for ions and neutrals can be found in a similar way.

3) Interpolation scheme. The distance traveled by electrons in a time step Δt is $\Delta x_e = \sqrt{3} \tilde{\theta}_e \Delta t$. Comparing to the spacing Δx , it is apparent that the ratio $\Delta x_e / \Delta x = \sqrt{3} \tilde{\theta}_e \Delta t / \Delta x = \sqrt{3} \tilde{\theta}_e / \delta c$ is less than one because the lattice sound speed is impossible to be greater than the speed of light. In another word, during a time step Δt , the electrons cannot stream to the adjacent node points, so do the ions and neutrals. Thus, it is necessary to apply the interpolation scheme to find the on-node value of the distribution functions after the streaming step in LBM. The interpolation scheme applied here is similar to the one described in Chapter 4. However, since the lattice sound speed $\tilde{\theta}_e$ is dependent on the temperature, and consequently, dependent on both time and space, the interpolation formula used here is different with the one shown in Eq. (101). Instead, by referring Figure 34, the formula takes the following form:

$$f_e(p) = \frac{nkf_e(p')}{(n-m)(k-m)} - \frac{mf_e(o')}{(k-m)(n-k)} + \frac{kf_e(q')}{(n-m)(n-k)} \quad (158)$$

where $m = \beta_e(p)$, $n = \beta_e(q) + 1$ and $k = \beta_e(o) - 1$. Note that the interpolation parameter now is dependent on both time and space and it is defined as $\beta_e(\mathbf{x}, t) = \sqrt{3}\tilde{\theta}_e(\mathbf{x}, t)\Delta t/\Delta x$. It is easy to see that if β_e is uniform throughout the whole domain, Eq. (158) becomes Eq. (101). Further, if $\beta_e = 1$, $f_e(p) = f_e(o')$ which means no interpolation exists.

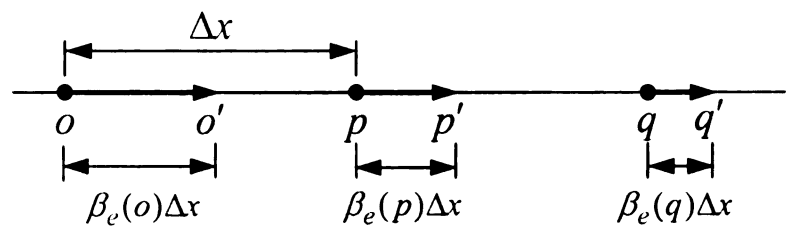


Figure 34 Schematic of the rescaling scheme. The value of distribution function at p can be found by using the post-collision values at o' , p' and q' .

4) Positions of simulation variables in the grid system. Unlike the isothermal plasma model developed in Chapter 4, the present model also has the temperature as a variable. The primary variables used in the calculation are listed in Table 11. All the variables listed in Table 11 are dependent on both space and time. But in the actual simulation, not all the variables are located on the same position in the grid system. That is due to the staggered scheme of the field vectors used in FDTD method. In order to satisfy the divergence free law $\nabla \cdot \mathbf{B} = 0$, the electric field and magnetic field are discretized on staggered node points as shown in Figure 30. The grid system as well as the positions of the primary variables is shown in Figure 35. As illustrated, magnetic field,

number density, macroscopic velocity and temperature are located at the primary nodes which are denoted by the white knots while the x- and y-component of electric field are located at the staggered grid nodes which are denoted by the solid knots respectively.

Number density	n_s
Macroscopic velocity	\mathbf{u}_s
Temperature of electron	T_s
Electric field	\mathbf{E}
Magnetic field	\mathbf{H}

Table 11 Primary simulation variables

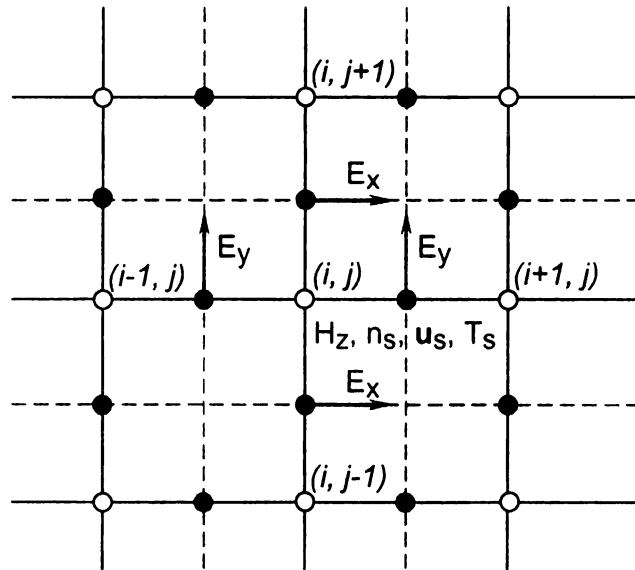


Figure 35 Positions of the simulation variables. H_z , n_s , u_s and T_s are calculated at the white node points while E_x and E_y are staggered in space and evaluated at the black node points.

Besides the above mentioned primary variables, there are also many secondary variables which depend on the primary variables used in the simulation. They are listed in Table 12.

Speed of sound	θ_s
Current density	\mathbf{J}
Relaxation times	λ_{sn}
Field ionization rates	R_s^f
Impact ionization rates	R_s^i
Recombination rates	R_s^r
Volumetric heat capacity	C_s
Thermal conductivity	κ_s
Interpolation factors	β_s

Table 12 Secondary simulation variables

Note that in the evaluation of the variables which involve electric field, such as current density and Lorentz force, the value of electric field should be calculated at the primary node point (i, j) . In the practical simulation, we just use the average value of the electric field neighboring the node point (i, j) :

$$\begin{aligned} E_x &= 0.5(E_x(i, j) + E_x(i, j+1)) \\ E_y &= 0.5(E_y(i, j) + E_y(i+1, j)) \end{aligned} \tag{159}$$

Besides the space discretization, the electric field is also staggered in time. Thus, the value of electric field should be used at the same time level in the time marching process:

$$\begin{aligned} E_x^{n-1} &= 0.5(E_x^{n-3/2} + E_x^{n-1/2}) \\ E_y^{n-1} &= 0.5(E_y^{n-3/2} + E_y^{n-1/2}) \end{aligned} \quad (160)$$

In conclusion, the Boltzmann equations, Maxwell's equations and energy equations are coupled to establish the present model. The Boltzmann equations are solved by using the traditional D2Q9 lattice Boltzmann method. In order to match the physical properties of the plasma, the rescaling scheme is applied to select the simulation parameters used in LBM. Besides the standard collision step and streaming step, an interpolation step is needed in this LBM model to find the on-node values of the distribution functions of the plasma particles. As the governing equation of the evolution of the temperatures, a set of particle energy equations are derived directly from the Boltzmann equations by taking the proper moments of the distribution functions. The energy equations are solved by the finite volume method. The FDTD method is adopted here to solve the Maxwell's equations where the UPML boundary condition is applied to terminate the outgoing electromagnetic waves. Figure 36 shows the flowchart of the present model. It can be seen that there are complicated correlations among those three equations. The external force in the Boltzmann equation is calculated by using the solutions of Maxwell's equation. The sound speeds, relaxation times, ionization and recombination rates are evaluated by using the results of the energy equation. When using FDTD method to solve the Maxwell's equations, the current density needs to be attained from the Boltzmann equation. In solving the energy equation, the Joule heating term is calculated by using the results from both Boltzmann equation and Maxwell's equations

while the other transport coefficients are evaluated from the results of Boltzmann equation. Figure 37 shows the correlations among the three equations. The elements through which one equation affects another are illustrated in the figure.

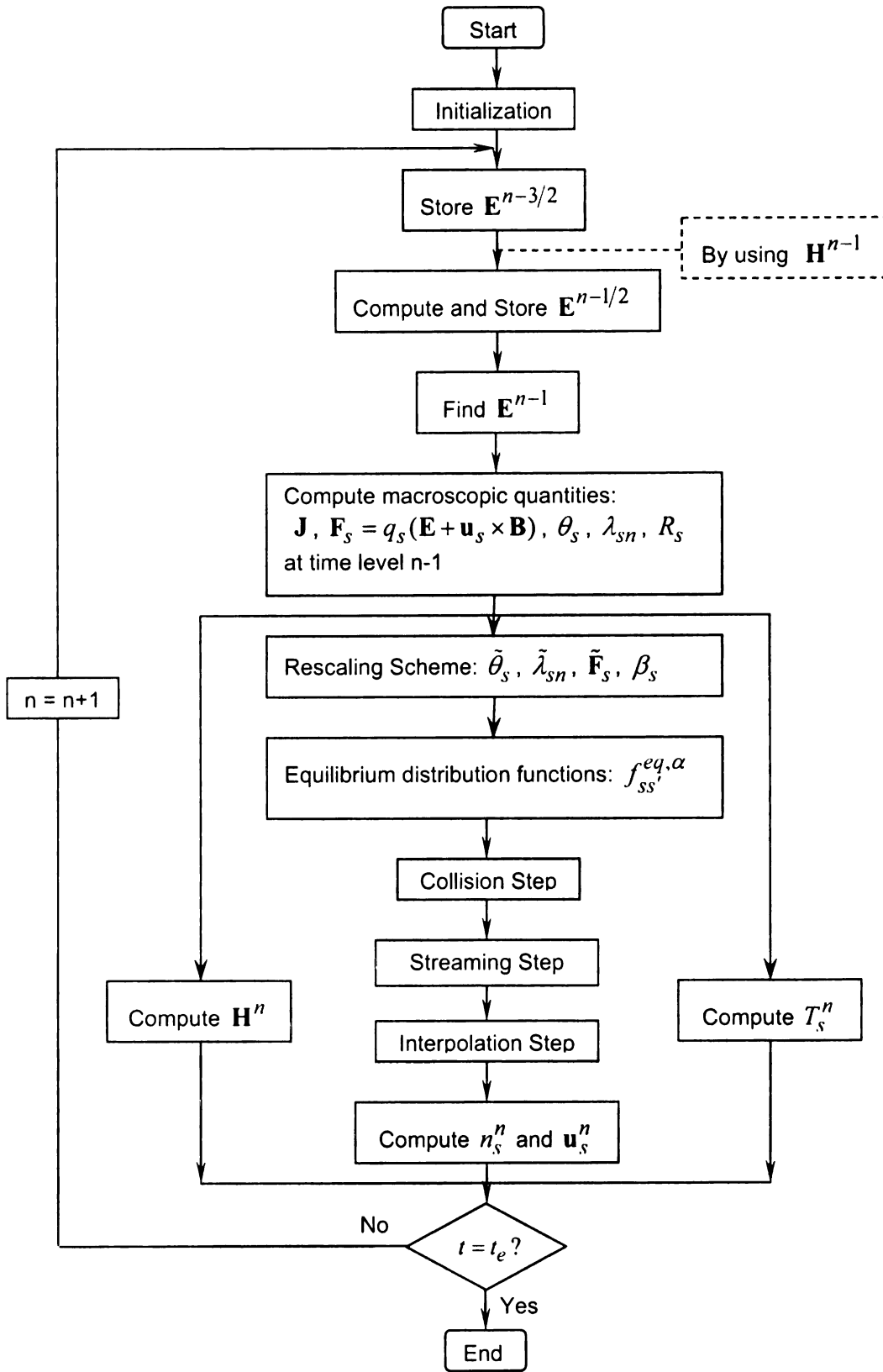


Figure 36 Flowchart of the present model

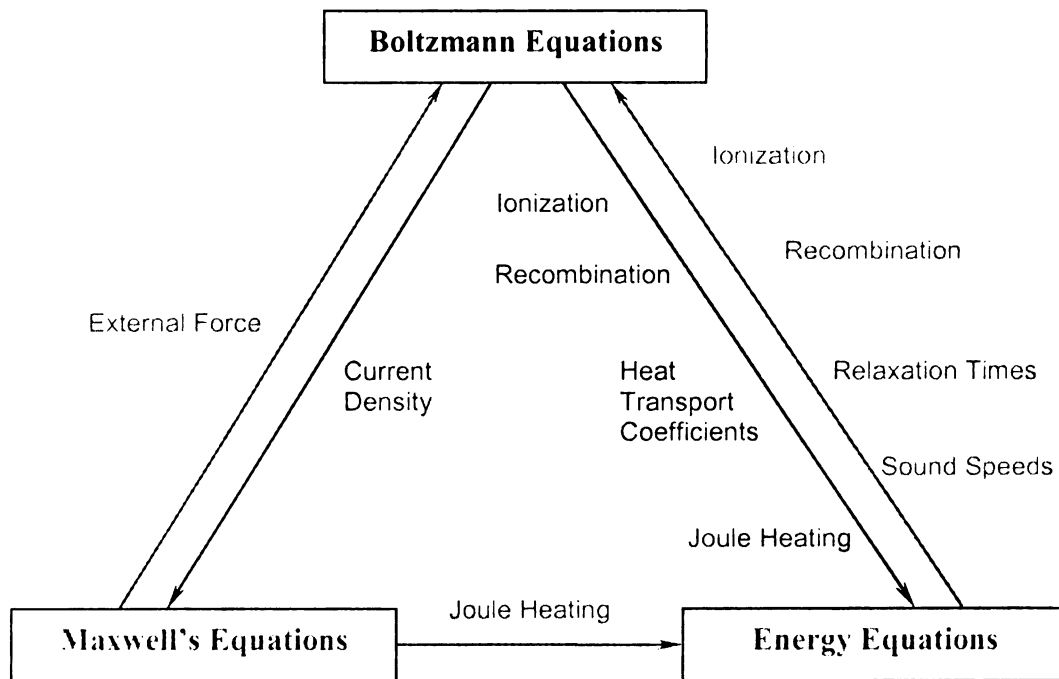


Figure 37 Correlation among three equations

5.4 Simulation Results

The interaction between a continuous CO₂ laser beam and a weakly ionized helium plasma is simulated by using the model developed here. The computational domain is a $135.68 \times 135.68 \mu\text{m}^2$ square which is discretized by a uniform 256×256 grid system. As illustrated in Figure 38, the computational domain is surrounded by a PML layer used as the boundary condition in the FDTD solver. The PML thickness is 30 grids. The origin point of the computational domain is located at the left lower corner. The interface between helium and vacuum is at $j = 200$. A continuous CO₂ laser beam whose wavelength is $10.6 \mu\text{m}$ is incident from the top of the computational domain and propagates along the negative y -direction. The no-gradient boundary condition is applied on all the boundaries enclosing the helium. Initially, the helium is assumed to have a

0.01% ionization degree. The initial number densities of neutrals, ions and electrons are $2.687 \times 10^{19} \text{ cm}^{-3}$, $2.687 \times 10^{15} \text{ cm}^{-3}$ and $2.687 \times 10^{15} \text{ cm}^{-3}$, respectively. The temperatures of all the three species of particles are set identical. According to Saha's equation, $T_{e0} = T_{i0} = T_{n0} = 1.058 \text{ eV}$.

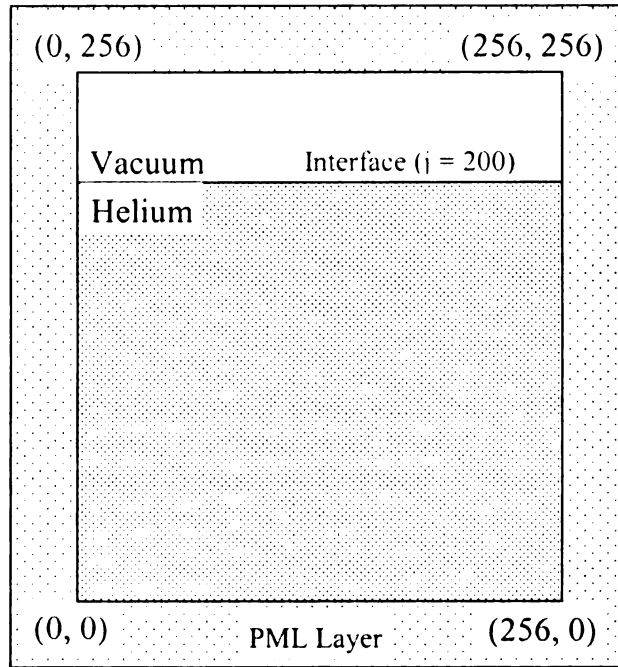


Figure 38 Schematic of the computational domain for simulation of interaction between a continuous CO₂ laser beam and a weakly ionized helium plasma.

After the laser beam crosses the interface, the free electrons in the weakly ionized helium plasma will be accelerated and heated by the laser field. As a result, the electron energy, including both the macroscopic kinetic energy and the thermal energy (temperature) will be increased. If the electron energy is higher than the ionization potential of helium, new free electrons will be generated through the electron impact ionization. Figure 39 shows the evolution of the maximum electron number densities

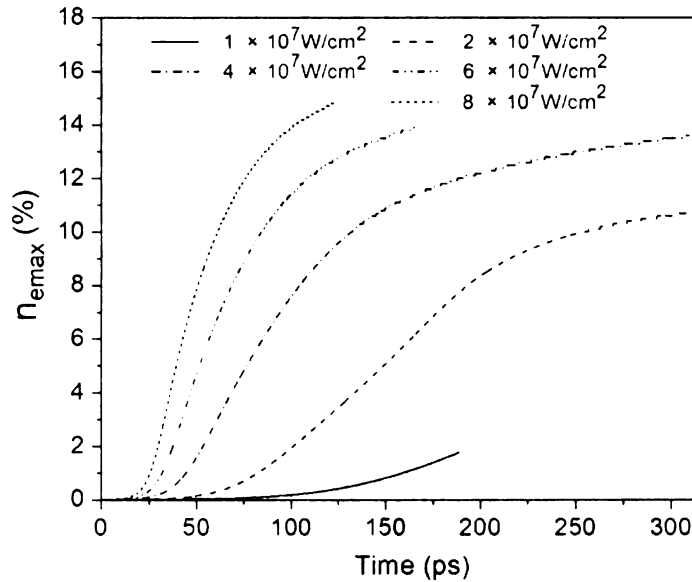


Figure 39 Evolution of maximum electron number density with different laser intensities. At the early stage, the electron number density increases exponentially because of the laser-induced ionization. However, it shows saturation later due to the equilibrium between ionization and recombination.

under exposure to different laser intensities. Note that the values shown in the figure is actually the maximum ratio of the electron number density to the initial neutral number density. Thus, it also can be interpreted as the maximum ionization degree throughout the whole computational domain. From the figure, the exponential increase of the electron number density due to the electron impact ionization can be seen clearly. We can also see that the electrons are generated with a higher rate if the laser intensity is higher. That is natural because higher laser intensity indicates that more laser energy is input into the domain in a unit time and thus leads to a quicker heating of the electrons. As long as the electron energy is above the ionization potential, the ionization will keep taking place and more and more new free electrons will be generated. However, ionization itself is a

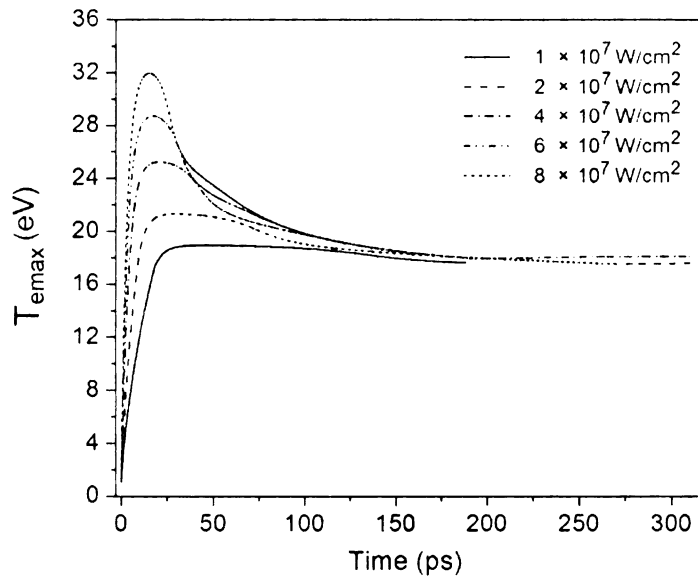


Figure 40 Evolution of maximum electron temperature with different laser intensities. The electron temperature increases very quickly due to the rapid heating. It decreases after the ionization takes place because the generation of new free electrons consumes the laser energy.

cooling scheme for electrons because, after all, the electron energy obtained from the laser beam is used to overcome the ionization potential and thus less laser energy is used to heat the electrons. This is evident in the energy equation where the ionization is just the sink term. Consequently, with more electrons generated, the electron temperature begins to decrease as shown in Figure 40. In this plot, the electron temperature increases very quickly at the early stage when the ionization hasn't taken place effectively. This can be verified by referring to Figure 39. For example, under the laser intensity of $8 \times 10^7 \text{ W/cm}^2$, the maximum electron number density starts to increase around 18 ps, which corresponds to the temperature decrease at about the same time moment as shown

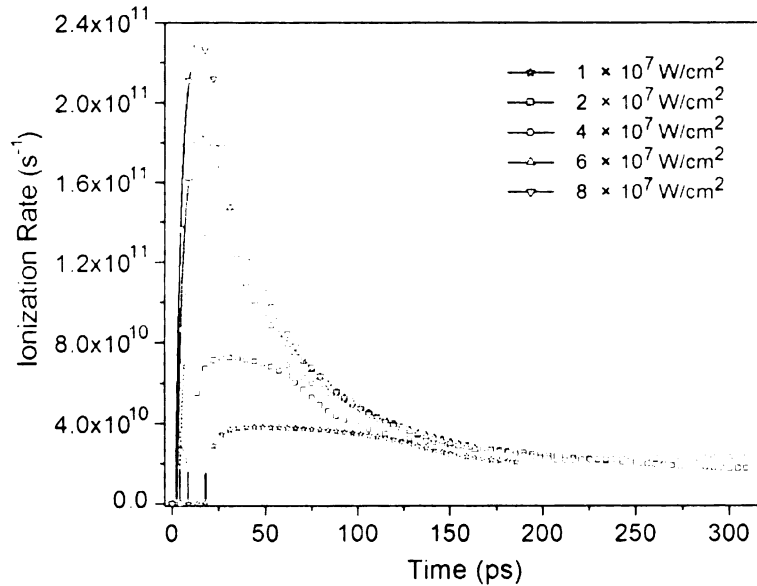


Figure 41 Evolution of ionization coefficient with different laser intensities. The ionization coefficient shows a similar pattern with the electron temperature because it mainly dependent on the electron energy.

in Figure 40. As the electron temperature decreases, the ionization rate is reduced accordingly. At the same time, since the recombination rate is proportional to the number densities of charge particle and inversely proportional to the electron temperature, the recombination becomes more and more prominent in the plasma. Reduction of ionization and enhancement of recombination lead that the generation rate of new free electrons gets lower and thus the electron number density shows a “saturation” phenomenon in Figure 39. This can be explained more evidently by Figure 41 and Figure 42 which are the evolutions of the ionization coefficient and the recombination coefficient respectively. Referring to Eq. (133), the ionization coefficient is mainly dependent on the electron energy. That is why the evolution of the ionization coefficient shown in Figure 41 has the

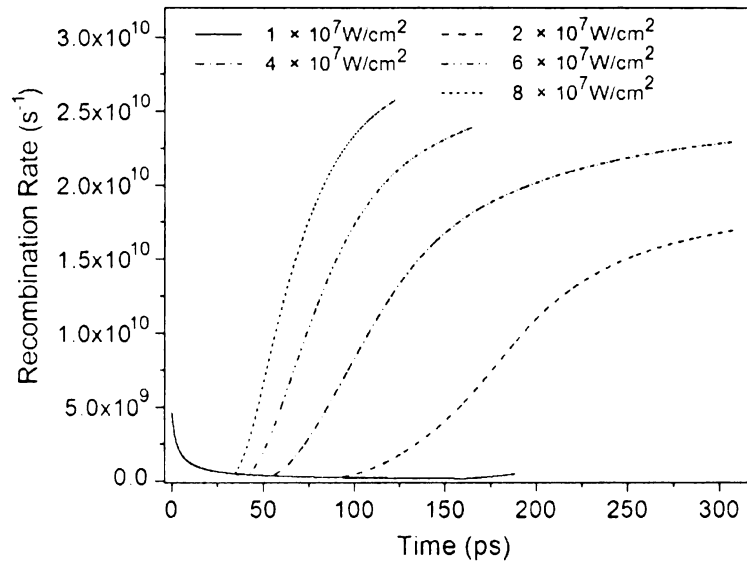


Figure 42 Evolution of recombination coefficient under different laser intensities. The recombination coefficient increases due to the generation of new free electrons and the decrease of the electron temperature.

similar pattern as the electron temperature. The pattern of evolution of the recombination coefficient can be explained by Eq. (134). Note that there are also “saturation” phenomena for the recombination coefficient. That happens when the electron number density and the electron temperature approach the “static” state as shown in Figure 39 and Figure 40.

Figure 43 and Figure 44 show the temperature evolutions of ion and neutral respectively. The ions are also heated by the laser field directly. But the heating rate is much slower because the ions are much heavier than the electrons. The ion temperature also decreases after some time as do the electrons. However, the cause of this temperature decrease is mainly due to the attenuation of the electric field instead of the cooling scheme of the ionization. That is why the decreasing points of the ion temperature are

much later than those of electron temperature. Of course, the attenuation of the electric field, which will be shown later, also affects the heating of electrons. But it is believed to be the minor factor comparing to the effects of the ionization for electrons. Unlike the charged particles, the neutrals are only heated by the heat transferred from the charged particles. That explains the latest increasing time of the neutral temperature as shown in Figure 44 and its continuous increases with time: as long as there is temperature difference between charged particles and neutrals, the cross heat transfer will be continued and the neutrals will be kept heated.

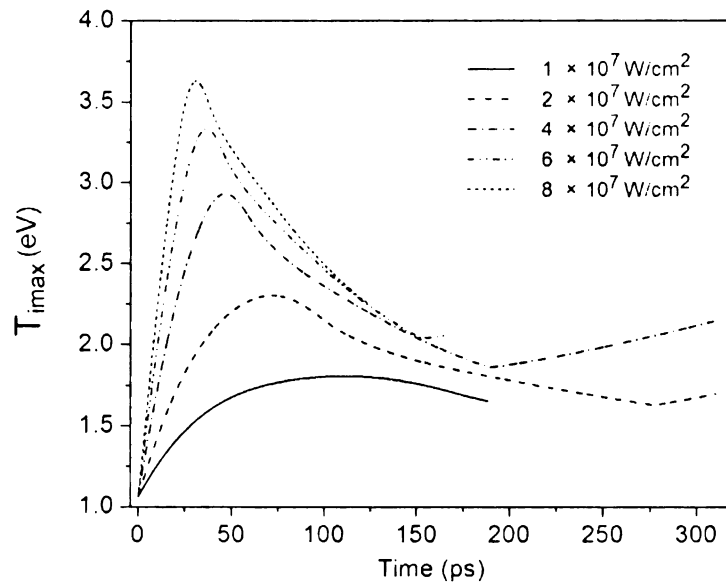


Figure 43 Evolution of maximum ion temperature with different laser intensities. Compared to the electron temperature, the ion temperature increases with a lower rate because of the heavy mass. It decreases due to the attenuation of the electric field.

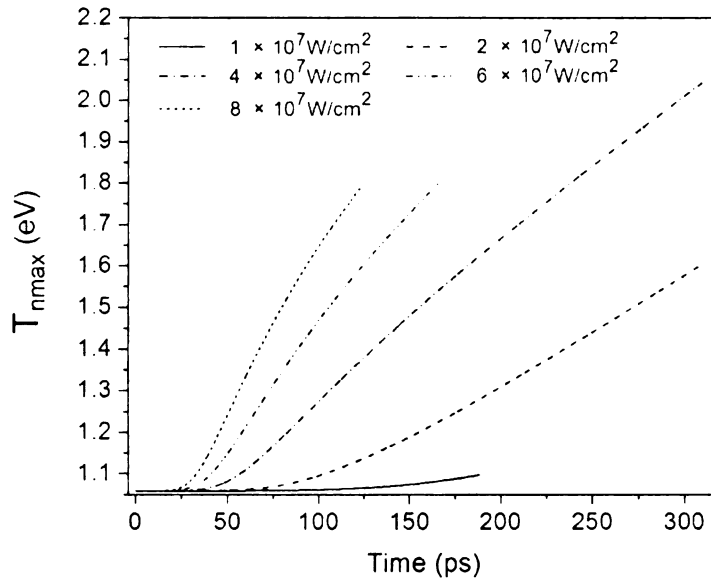


Figure 44 Evolution of neutral temperature with different laser intensities. Unlike the temperatures of electrons and ions, the neutral temperature keeps increasing because the neutrals are heated by the cross-heat transfer from the charged particles.

Figure 45 and Figure 46 show the distributions of electron temperature and electron number density along the beam propagation axis respectively where the incident laser intensity is $2 \times 10^7 \text{ W/cm}^2$. It can be seen from the figures that, very naturally, the electrons are heated first near the interface and thus the largest electron number density always emerges at the interface. As analyzed above, after some time, the temperature near the interface decreases due to the ionization. The temperature distribution on the axis becomes more and more uniform with time lapse. Finally, an almost uniform temperature is established along the axis and it decreases very slowly which is believed to be due to the temperature diffusion process. The saturation of electron number density can also be seen from Figure 46 where the number density near the interface increase very slowly with time in the later stage.

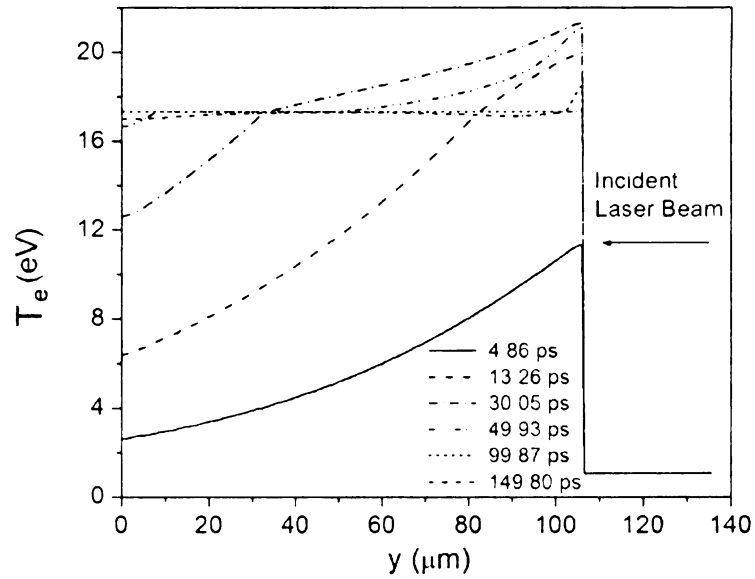


Figure 45 Distribution of electron temperature along beam propagation axis at different time moments. The highest temperature always appears at the interface.

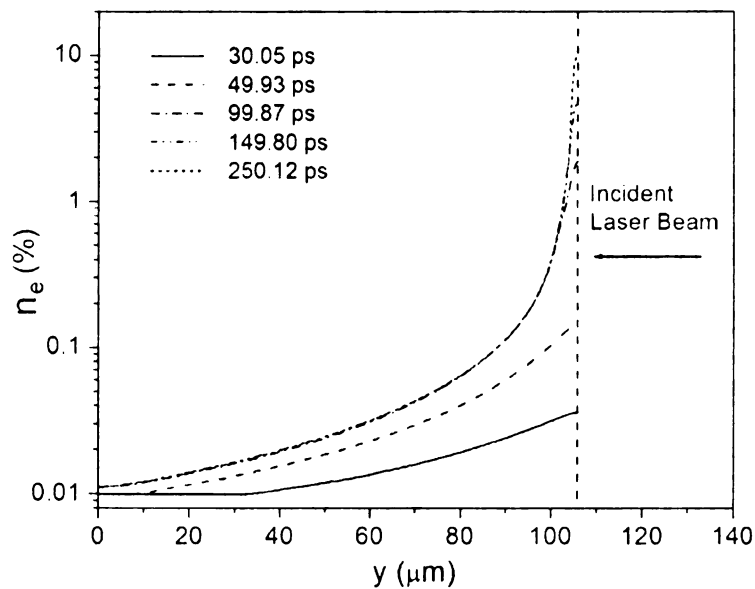
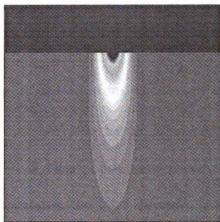
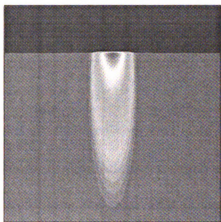
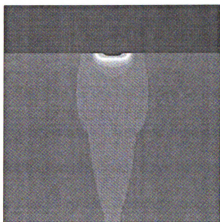
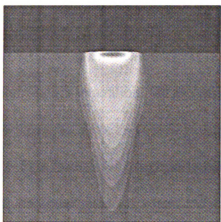


Figure 46 Distribution of electron number density along the beam propagation axis at different time moments. Most of the new free electrons are generated near the interface.



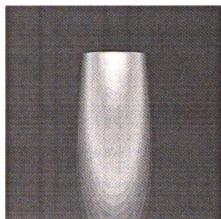
(a) $t = 49.93$ ps



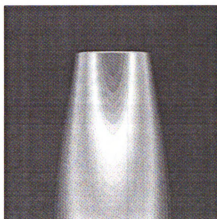
(b) $t = 149.80$ ps

Figure 47 Snapshots of electron and neutral number densities at (a) $t = 49.93$ ps and (b) $t = 149.80$ ps

Figure 47 shows the contours of electron and neutral number densities at two time moments where the unit of the number density in the plot is cm^{-3} . The laser intensity in this illustration is $2 \times 10^7 W/cm^2$. The generation of free electrons and loss of neutral particles are matched very well from the plots, which is evident by the ionization terms introduced in the Boltzmann equations. Further, it is clearly that more electrons are generated along the axis. That is understandable because the laser intensity is higher along the axis due to its Gaussian distribution in space. It also can be seen that most of the free electrons are generated in the flat thin layer below the interface as shown in Figure 47 (b). This can be explained as follows. The electrons on the axis are heated at the earliest and when their energy is high enough, they will ionize the neutrals due to the electron impact ionization. On the other hand, the electrons at the outer rim of the laser field will not be heated so quickly because the laser intensity there is not as high as in the center. This leads to the highest temperature on the axis at the early stage as shown in Figure 48 (a), (b) and (c) where the temperature is in unit of eV. However, because the ionization rate is higher at the center, the temperature decreases also quicker there due to the ionization. In such a case, it is possible that the temperature at the outer rim of the laser field is higher after some time as shown in Figure 48 (d). As a result, more electrons are generated at those locations than on the axis. Then a flat pattern of the electron number density below the interface emerges. This can be seen more clearly from Figure 49 which is the electron number density distribution along the x-axis at $j = 195$, i.e. 5 grid points below the interface. The above analysis can be verified more evidently by Figure 50 which shows the snapshots of ionization coefficient $R_c^i (s^{-1})$ and recombination



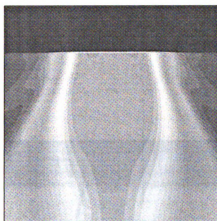
(a) $t = 4.86$ ps



(b) $t = 13.26$ ps



(c) $t = 49.93$ ps



(d) $t = 149.80$ ps

Figure 48 Contours of electron temperature at (a) $t = 4.86$ ps, (b) $t = 13.26$ ps, (c) $t = 49.93$ ps and (d) 149.80 ps

coefficient R_e^r (s^{-1}) at $t = 149.80$ ps. It can be seen that the ionization becomes stronger at the outer rim of the laser beam below the interface. At the same positions, the recombination is weaker while it is more prominent in the center. This leads to relatively less electron generated in the center and more generation of electrons at the outer rim of the laser beam.

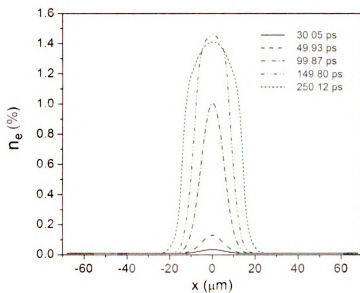


Figure 49 Electron number density distribution along x-axis at $j = 195$ at different time moments

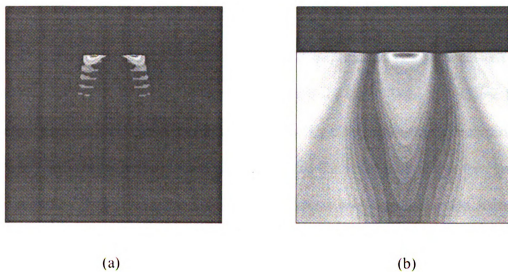
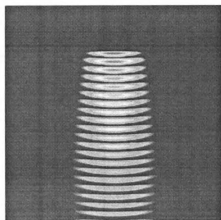
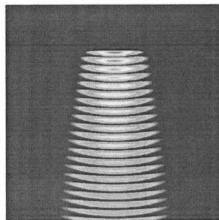


Figure 50 Snapshot of (a) impact ionization coefficient and (b) recombination coefficient at $t = 149.80$ ps

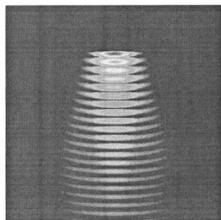
The temperature evolution as shown in Figure 48 can be explained from the point view of Joule heating, which is essentially the laser energy deposited into the plasma. The snapshots of Joule heating at four time moments are shown in Figure 51. It is clearly seen that the Joule heating is attenuated along the laser beam propagation and most of the laser energy is deposited in the thin layer below the interface eventually. According to the definition, Joule heating is dependent on two factors: the current density and the electric field. After a further analysis, one can find that the Joule heating is essentially proportional to the number densities of the charged particles and the square of the electric field while inversely proportional to the electron temperature. Thus, it is natural to conclude that the Joule heating decreases in the region where the number densities of charged particles are low and the electron temperature is high, just as shown in Figure 51. For the electric field, with the increase of the current density (mainly due to the increase of number densities of charged particles), the electric field is reduced according to the Maxwell's equation. It is apparent that the current density is the highest on the axis below the interface because the strongest ionization takes place there. Thus, the electric field is attenuated most in that region as shown in Figure 52. Comprehensively considering the effects of the current density and the electric field, the Joule heat shows the "leaking" phenomenon as shown in Figure 51. This also explains why there is similar phenomena in temperature evolution.



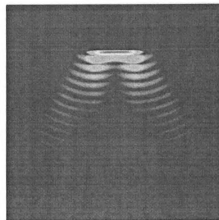
(a) $t = 4.86$ ps



(b) $t = 13.26$ ps

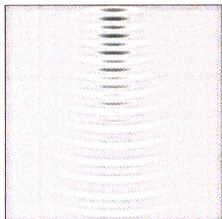


(c) $t = 49.93$ ps

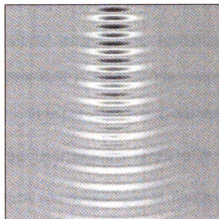


(d) $t = 149.80$ ps

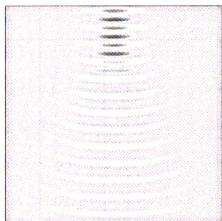
Figure 51 Snapshots of Joule heating at (a) $t = 4.86$ ps, (b) $t = 13.26$ ps, (c) $t = 49.93$ ps and (d) $t = 149.80$ ps



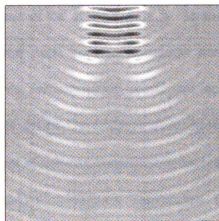
(a) $t = 4.86$ ps



(b) $t = 13.26$ ps



(c) $t = 49.93$ ps

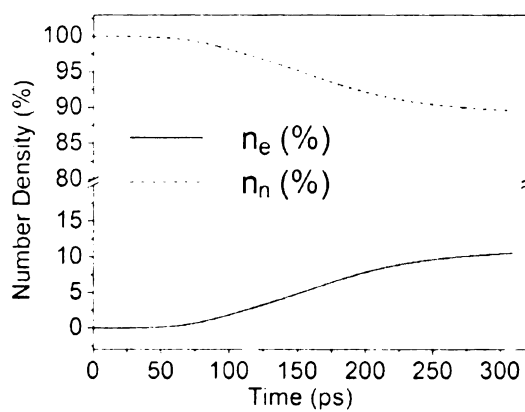


(d) $t = 149.80$ ps

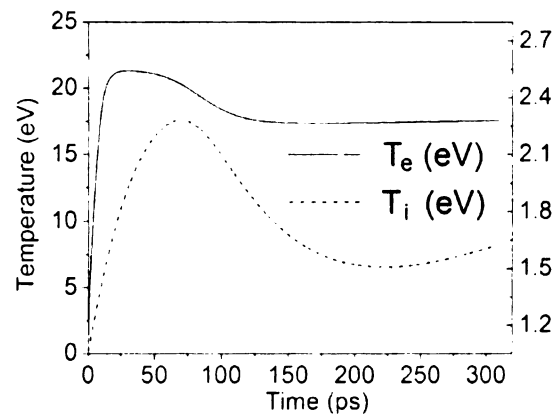
Figure 52 Snapshots of x-component of electric field at (a) $t = 4.86$ ps, (b) $t = 13.26$ ps, (c) $t = 49.93$ ps and (d) $t = 149.80$ ps

Finally, the evolutions of number densities, temperatures, ionization and recombination coefficients, and magnitude of electric field at Point A (the center point just below the interface whose coordinate is (128, 199) in the grid system) are shown in Figure 53. Those results are obtained by using the laser intensity of $2 \times 10^7 \text{ W/cm}^2$. Generation of electrons and loss of neutrals happen correspondingly as illustrated by Figure 53 (a) where the saturation phenomenon can be shown very clearly. This saturation can be explained directly by Figure 53 (c). In that plot, the ionization coefficient reaches a “static” state due to the decrease of the electron energy. As analyzed above, this energy loss is caused by the ionization itself because ionization here also plays a role for cooling the electrons. Meanwhile, the recombination coefficient increases thanks to the combined effects of electron number density and temperature. Moreover, recombination of charged particles also releases heat which can contribute to increase the electron temperature. Eventually, the recombination coefficient approaches to the ionization coefficient as shown in the plot. Then the equilibrium between the ionization and recombination is expected to be established. The electron temperature and ion temperature are shown in Figure 53 (b). The different heating rate of electrons and ions caused by their far different masses are apparent from the plot. The electron temperature increases very quickly at the early stage mainly due to the rapid heating from the laser energy through Joule heating in this model. After the effective ionization takes place, the electron temperature starts to decrease due to the dynamics of ionization and recombination as analyzed before. Like the electrons, the ions are also heated by the incident laser beam but with a much lower heating rate. Decrease of the ion temperature

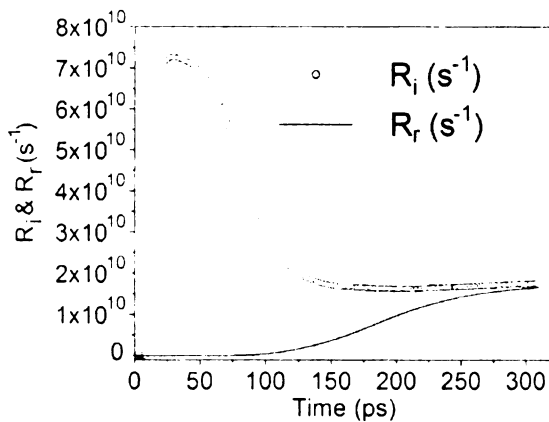
is mainly caused by the attenuation of the electric field as illustrated in Figure 53 (d). This attenuation of electric field is deduced by the increased current density which is dependent on the temperatures and number densities of charged particles. Since both the temperatures and number densities illustrate the saturation behavior, the attenuation of the electric field is also presenting the similar pattern as expected.



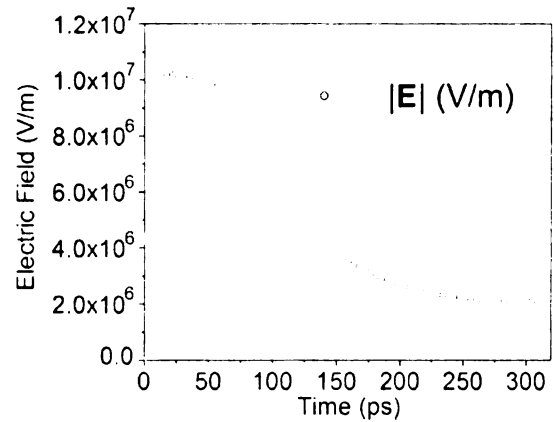
(a)



(b)



(c)



(d)

Figure 53 Evolution of (a) number densities (b) temperatures (c) ionization and recombination coefficients and (d) magnitude of electric field at Point A

In conclusion, the interaction between laser and weakly ionized plasma shows very complicated behaviors due to the dynamics of ionization and recombination. The propagation of the laser beam and the laser energy deposition are significantly affected by the generation of the free electrons. Meanwhile, the heating pattern of free electrons by the laser beam also determines the ionization and recombination dynamics of the plasma. The spatial distribution of the laser field makes the problem more complicated. The simulation results presented above show the great potential of the current model to simulate laser interaction with weakly ionized plasma. Not only the wave characteristics of the laser beam are retained, but also the physical heating patterns for all the plasma particles are illustrated by using this model. Unlike the kinetic-based model, such as PIC, this model can be applied for physical problems with much larger timing and spatial scales. Comparing to the hydrodynamic models, the present model has less assumptions (such as continuum assumption) and thus can be used to simulate a wide range of problems.

Chapter 6

Conclusion

A new LBM based model is developed in this dissertation, for the first time, to simulate laser interaction with weakly ionized plasmas. By introducing an additional term in the Boltzmann equations, the effects of electron impact ionization and its inverse process, three-body recombination, on the change of rate of the distribution functions are included so that the ionization and recombination dynamics can be taken into account in this model. The Boltzmann equations, particle energy equations and Maxwell's equations are coupled and constitute the governing equations of the present model. The Boltzmann equations are solved by the traditional D2Q9 LBM on a uniform square grid system. The external force term in the Boltzmann equation is evaluated by using He's model after an elaborate comparison of the results of some hydrodynamics flows obtained by the other four models. In the evaluation of the external force term and the Joule heating term in the energy equation, the FDTD method is adopted to solve the full set of Maxwell's equation so that the wave nature of the electromagnetic field carried by the laser beam and generated by the plasma dynamics can be retained to the greatest content. The energy (temperature) evolutions of the individual species of particles in the plasma are solved from the energy equations which are directly derived from the Boltzmann equations by taking proper moments of the distribution functions.

To match the physical properties of the plasma, a rescaling scheme is proposed in this study to select the proper simulation parameters used in LBM. This rescaling scheme

is validated by the two-dimensional driven cavity flow and the isothermal weakly ionized plasma simulations. In the practical implementation of the present model, the spacing Δx is usually determined by the resolution requirements of the physical problem, the time step Δt is selected by the stability requirement of the FDTD solver and the dimensionless relaxation time τ can be prescribed arbitrarily as long as it is in the valid range. Once the above three parameters are determined, the lattice sound speed $\tilde{\theta}_s$, the lattice relaxation time $\tilde{\lambda}_{sn}$ ($s = e, i, n$) and the lattice acceleration term $\tilde{\mathbf{a}}_s$ ($s = e, i$) can be found according to the rescaling rules and would be used in the LBM calculations. After the standard collision step and streaming step, it is necessary to introduce an interpolation step to find the on-node values of the distribution functions. This is due to the fact that the particles in the plasma cannot travel to their neighboring nodes in the period of a time step Δt . Conclusively, the Boltzmann equations with the ionization and recombination term are solved by the standard D2Q9 LBM with supplement of the rescaling scheme and an interpolation step following the streaming step. The number densities, macroscopic velocities and current densities of the plasma particles can be found as the results of the LBM solver and are used in the solvers of the FDTD and the energy equations.

As a simulation example, the interaction between a continuous CO₂ laser beam and a weakly ionized helium plasma is simulated by using the proposed model in this dissertation. The results show the physical heating patterns of the particles in the plasma due to the laser energy deposition. The ionization and recombination dynamics and its effects on the heating and generation of free electrons are also illustrated from the simulation results. Although the simulation conducted in this dissertation is only a preliminary application, it still could show the capabilities and limitations of the present

model. Compared to the kinetic-based methods, such as PIC models and MD simulations, our model is much less computationally expensive because there is no need to solve the Newton-Lorentz equation for every single particle. Thus it is possible to use the “real” plasma particles in the simulation instead of those “super-particles” used in PIC and MD simulations. The advantage of the present model over the hydrodynamics models is that there is no continuum assumption employed in this model. As a consequence, this model can be applied in a wide range of the physical problems. Another prominent feature of the present model is that Maxwell’s equation is directly solved here to retain the most detailed wave behaviors of the electromagnetic field. Thus, this model is applicable for even the most complicated wave related problems, such as complex geometries, multiple incident laser beams and ablation of gradient materials. Finally, the present model is very easy to implement because each of the three solvers is well developed and many achievements in the individual field can be inherited in development of this model.

Of course, no “general” model which can be applied for all physical problems exists. The limitations of the present model include the following aspects. First of all, this model is only applicable for relatively low laser intensity. This limitation is mainly due to the low Mach number assumption made in the derivation of the lattice Boltzmann equations. High laser intensity, as expected, will induce high electron velocities which might break the low Mach number assumption. To overcome this problem, it is intuitive to abandon the low Mach number assumption and adopt more velocity components in discretization of the phase space. But unfortunately, this multiple-speed approach for high Mach flow is still under development and always suffers from high instability. Therefore, a high Mach number LBM scheme is highly desired for plasma simulation.

Second, the physical spatial and temporal scales that can be simulated by this model are largely limited by the FDTD method. In order to capture the wave nature of the electromagnetic field accurately, the spacing Δx in FDTD is required to be much less than the wave length of the laser beam. Further, due to the stability requirement, the time step Δt also needs to be sufficiently small. Thus, an ultra-stable FDTD solver is needed for simulation of real size physical problems. Third, an interface tracking technique may be needed to simulate the plasma plume expansion in vacuum. Plasma plume expansion is very important in many applications, such as laser welding and pulsed laser deposition. However, one difficulty in simulating this phenomenon is how to track the evolution of the interface between the plasma and the vacuum. One possible approach is to use the level set method. But apparently, there is a long way to go to combine the level set method with the LBM.

In conclusion, although the LBM model developed in this dissertation is only in its preliminary stage, it has already shown great potential for simulation of laser interaction with weakly ionized plasmas. It is hoped that those aforementioned limitations could be eliminated in the future and as a result, this new model could be applied widely and successfully.

REFERENCE

1. Du, D., et al., *Laser-Induced Breakdown by Impact Ionization in SiO₂ with Pulse Widths from 7 Ns to 150 Fs*. Applied Physics Letters, 1994. **64**(23): p. 3071-3073.
2. Perry, M.D., et al., *Ultrashort-pulse laser machining of dielectric materials*. Journal of Applied Physics, 1999. **85**(9): p. 6803-6810.
3. Fan, C.H. and J.P. Longtin, *Modeling optical breakdown in dielectrics during ultrafast laser processing*. Applied Optics, 2001. **40**(18): p. 3124-3131.
4. Schlessinger, L. and J. Wright, *Inverse-Bremsstrahlung Absorption Rate in an Intense Laser Field*. Physical Review A, 1979. **20**(5): p. 1934-1945.
5. Wierling, A., et al., *Inverse bremsstrahlung of hot, weakly coupled plasmas*. Physics of Plasmas, 2001. **8**(8): p. 3810-3819.
6. Leemans, W.P., et al., *Stimulated Compton-Scattering from Preformed Underdense Plasmas*. Physical Review Letters, 1991. **67**(11): p. 1434-1437.
7. Kosarev, I.N., *Kinetic theory of plasma and gas. Interaction of high-intensity laser pulses with plasmas*. Physics-Uspekhi, 2006. **49**(12): p. 1239-1252.
8. Gibbon, P. and E. Forster, *Short-pulse laser-plasma interactions*. Plasma Physics and Controlled Fusion, 1996. **38**(6): p. 769-793.
9. Rozmus, W. and V.T. Tikhonchuk, *Skin Effect and Interaction of Short Laser-Pulses with Dense-Plasmas*. Physical Review A, 1990. **42**(12): p. 7401-7412.
10. Pert, G.J., *Inverse Bremsstrahlung in Strong Radiation-Fields at Low-Temperatures*. Physical Review E, 1995. **51**(5): p. 4778-4789.
11. Offenberger, A.A., et al., *2-Plasmon Decay in a Co₂-Laser-Plasma Interaction Experiment*. Physical Review A, 1978. **18**(2): p. 746-749.
12. Machacek, A.C. and J.S. Wark, *A fluid-kinetic model for the two plasmon decay instability*. Physics of Plasmas, 2001. **8**(10): p. 4357-4366.
13. Berger, R.L., et al., *On the dominant and subdominant behavior of stimulated Raman and Brillouin scattering driven by nonuniform laser beams*. Physics of Plasmas, 1998. **5**(12): p. 4337-4356.
14. Lindl, J.D., et al., *The physics basis for ignition using indirect-drive targets on the National Ignition Facility*. Physics of Plasmas, 2004. **11**(2): p. 339-491.

15. Kruer, W.L., *The physics of laser plasma interactions*. 1988, Redwood City, Calif.: Addison-Wesley. xviii, 182 p.
16. Maximov, A.V., et al., *Modeling of stimulated Brillouin scattering near the critical-density surface in the plasmas of direct-drive inertial confinement fusion targets*. *Physics of Plasmas*, 2004. **11**(6): p. 2994-3000.
17. Shukla, P.K., et al., *Relativistic Nonlinear Effects in Plasmas*. *Physics Reports-Review Section of Physics Letters*, 1986. **138**(1-2): p. 1-149.
18. Sharma, P., et al., *Laser beam filamentation and stochastic electron heating at upper hybrid layer*. *Physics of Plasmas*, 2008. **15**(4): p. 042105.
19. Max, C.E., J. Arons, and A.B. Langdon, *Self-Modulation and Self-Focusing of Electromagnetic-Waves in Plasmas*. *Physical Review Letters*, 1974. **33**(4): p. 209-212.
20. Antonsen, T.M. and P. Mora, *Self-Focusing and Raman-Scattering of Laser-Pulses in Tenuous Plasmas*. *Physics of Fluids B-Plasma Physics*, 1993. **5**(5): p. 1440-1452.
21. Brunel, F., *Not-So-Resonant, Resonant Absorption*. *Physical Review Letters*, 1987. **59**(1): p. 52-55.
22. Bauer, D. and P. Mulser, *Vacuum heating versus skin layer absorption of intense femtosecond laser pulses*. *Physics of Plasmas*, 2007. **14**(2): p. 023301.
23. Kruer, W.L. and K. Estabrook, *Jxb Heating by Very Intense Laser-Light*. *Physics of Fluids*, 1985. **28**(1): p. 430-432.
24. Denavit, J., *Absorption of High-Intensity Subpicosecond Lasers on Solid Density Targets*. *Physical Review Letters*, 1992. **69**(21): p. 3052-3055.
25. Leemans, W.P., et al., *Experiments and Simulations of Tunnel-Ionized Plasmas*. *Physical Review A*, 1992. **46**(2): p. 1091-1105.
26. Auguste, T., et al., *Defocusing Effects of a Picosecond Terawatt Laser-Pulse in an Underdense Plasma*. *Optics Communications*, 1992. **89**(2-4): p. 145-148.
27. Chen, S.Y., et al., *Evolution of a plasma waveguide created during relativistic-ponderomotive self-channeling of an intense laser pulse*. *Physical Review Letters*, 1998. **80**(12): p. 2610-2613.
28. Vujicic, N., et al., *Low-density plasma channels generated by femtosecond pulses*. *Applied Physics B-Lasers and Optics*, 2006. **82**(3): p. 377-382.
29. Umstadter, D., *Relativistic laser-plasma interactions*. *Journal of Physics D-Applied Physics*, 2003. **36**(8): p. R151-R165.

30. Bogaerts, A. and Z.Y. Chen, *Effect of laser parameters on laser ablation and laser-induced plasma formation: A numerical modeling investigation*. Spectrochimica Acta Part B-Atomic Spectroscopy, 2005. **60**(9-10): p. 1280-1307.
31. Christen, H.M. and G. Eres, *Recent advances in pulsed-laser deposition of complex oxides*. Journal of Physics-Condensed Matter, 2008. **20**(26): p. 264005.
32. Dwivedi, A., *Recent advances in pulsed laser ablated plasma plumes: A review*. Surface review and letters, 2007. **14**(1): p. 57-69.
33. Chen, X. and H.X. Wang, *Prediction of the laser-induced plasma characteristics in laser welding: a new modelling approach including a simplified keyhole model*. Journal of Physics D-Applied Physics, 2003. **36**(13): p. 1634-1643.
34. McCrory, R.L., et al., *Progress in direct-drive inertial confinement fusion*. Physics of Plasmas, 2008. **15**(5): p. 055503.
35. Badziak, J., S. Jablonski, and J. Wolowski, *Progress and prospect of fast ignition of ICF targets*. Plasma Physics and Controlled Fusion, 2007. **49**(12B): p. B651-B666.
36. Tajima, T. and J.M. Dawson, *Laser Electron-Accelerator*. Physical Review Letters, 1979. **43**(4): p. 267-270.
37. Joshi, C., et al., *Forward Raman Instability and Electron Acceleration*. Physical Review Letters, 1981. **47**(18): p. 1285-1288.
38. Esarey, E., et al., *Overview of plasma-based accelerator concepts*. Ieee Transactions on Plasma Science, 1996. **24**(2): p. 252-288.
39. Bingham, R., J.T. Mendonca, and P.K. Shukla, *Plasma based charged-particle accelerators*. Plasma Physics and Controlled Fusion, 2004. **46**(1): p. R1-R23.
40. Wang, F.C., et al., *Electron acceleration by a propagating laser pulse in vacuum*. Physics of Plasmas, 2007. **14**(8): p. 083102.
41. Modena, A., et al., *Electron Acceleration from the Breaking of Relativistic Plasma-Waves*. Nature, 1995. **377**(6550): p. 606-608.
42. Pasquini, C., et al., *Laser induced breakdown spectroscopy*. Journal of the Brazilian Chemical Society, 2007. **18**(3): p. 463-512.
43. Babushok, V.I., et al., *Double pulse laser ablation and plasma: Laser induced breakdown spectroscopy signal enhancement*. Spectrochimica Acta Part B-Atomic Spectroscopy, 2006. **61**(9): p. 999-1014.
44. Gordon, C.L., et al., *Time-Gated Imaging with an Ultrashort-Pulse, Laser-Produced-Plasma X-Ray Source*. Optics Letters, 1995. **20**(9): p. 1056-1058.

45. Tillman, C., et al., *Elemental biological imaging by differential absorption with a laser-produced x-ray source*. Journal of the Optical Society of America B-Optical Physics, 1996. **13**(1): p. 209-215.
46. Tillman, C., et al., *Imaging Using Hard X-Rays from a Laser-Produced Plasma*. Applied Physics B-Lasers and Optics, 1995. **61**(4): p. 333-338.
47. Zimmerman G, et al., *LASNEX Code for Inertial Confinement Fusion*. Journal of the Optical Society of America, 1978. **68**(4): p. 549.
48. *The Lawrence Livermore laser fusion program: A status report*. Annals of the New York Academy of Sciences, 2006. **267**(Third Conference on the Laser): p. 93-110.
49. Clark, D.S., S.W. Haan, and J.D. Salmonson, *Robustness studies of ignition targets for the National Ignition Facility in two dimensions*. Physics of Plasmas, 2008. **15**: p. 056305.
50. Li, C.K., et al., *Measuring E and B fields in laser-produced plasmas with monoenergetic proton radiography*. Physical Review Letters, 2006. **97**: p. 135003.
51. Gus'kov, S.Y., et al., *Numerical modeling of a 2D wave of electron thermal conductivity produced by a laser beam in targets of subcritical density*. Journal of Russian Laser Research, 2000. **21**(2): p. 157-167.
52. Craxton, R.S. and R.L. Mccrory, *Hydrodynamics of Thermal Self-Focusing in Laser Plasmas*. Journal of Applied Physics, 1984. **56**(1): p. 108-117.
53. Marinak, M.M., et al., *Three-dimensional HYDRA simulations of National Ignition Facility targets*. Physics of Plasmas, 2001. **8**(5): p. 2275-2280.
54. Meezan, N.B., et al., *Hydrodynamics simulations of 2 omega laser propagation in underdense gasbag plasmas*. Physics of Plasmas, 2004. **11**(12): p. 5573-5579.
55. Schmitt, A.J. and B.B. Afeyan, *Time-dependent filamentation and stimulated Brillouin forward scattering in inertial confinement fusion plasmas*. Physics of Plasmas, 1998. **5**(2): p. 503-517.
56. Myatt, J., et al., *Modeling stimulated Brillouin scattering in the underdense corona of a direct drive inertial confinement fusion target*. Physics of Plasmas, 2004. **11**(7): p. 3394-3403.
57. Divol, L., et al., *Three-dimensional modeling of laser-plasma interaction: Benchmarking our predictive modeling tools versus experiments*. Physics of Plasmas, 2008. **15**(5): p. 056313.
58. Divol, L., et al., *Three-dimensional modeling of stimulated Brillouin scattering in ignition-scale experiments*. Physical Review Letters, 2008. **100**(25): p. 255001.

59. Myatt, J., et al., *Nonlinear propagation of a randomized laser beam through an expanding plasma*. Physical Review Letters, 2001. **87**(25): p. 255003.
60. Riazuelo, G. and G. Bonnaud, *Coherence properties of a smoothed laser beam in a hot plasma*. Physics of Plasmas, 2000. **7**(10): p. 3841-3844.
61. Walraet, F., G. Bonnaud, and G. Riazuelo, *Velocities of speckles in a smoothed laser beam propagating in a plasma*. Physics of Plasmas, 2001. **8**(11): p. 4717-4720.
62. Weber, S., et al., *Modeling of laser-plasma interaction on hydrodynamic scales: Physics development and comparison with experiments*. Laser and Particle Beams, 2004. **22**(2): p. 189-195.
63. Lewis, K., G. Riazuelo, and C. Labaune, *Modeling of imaging diagnostics for laser plasma interaction experiments with the code PARAX*. Review of Scientific Instruments, 2005. **76**(9): p. 093502.
64. Marinak, M.M., et al., *Nonlinear Rayleigh-Taylor evolution of a three-dimensional multimode perturbation*. Physical Review Letters, 1998. **80**(20): p. 4426-4429.
65. Marinak, M.M., et al., *Three-dimensional simulations of Nova high growth factor capsule implosion experiments*. Physics of Plasmas, 1996. **3**(5): p. 2070-2076.
66. Schurtz, G.P., P.D. Nicolai, and M. Busquet, *A nonlocal electron conduction model for multidimensional radiation hydrodynamics codes*. Physics of Plasmas, 2000. **7**(10): p. 4238-4249.
67. Devore, C.R., *Flux-Corrected Transport Techniques for Multidimensional Compressible Magnetohydrodynamics*. Journal of Computational Physics, 1991. **92**(1): p. 142-160.
68. Hittinger, J.A.F. and M.R. Dorr, *Improving the capabilities of a continuum laser plasma interaction code*. Journal of Physics: Conference Series, 2006. **46**: p. 422-432.
69. Bibi, F.A. and J.P. Matte, *Influence of the electron distribution function shape on nonlocal electron heat transport in laser-heated plasmas*. Physical Review E, 2002. **66**(6): p. 066414.
70. Huller, S., P. Mounaix, and D. Pesme, *Numerical simulation of filamentation and its interplay with SBS in underdense plasmas*. Physica Scripta, 1996. **T63**: p. 151-157.
71. Finke, B.R., P.D. Kapadia, and J.M. Dowden, *A Fundamental Plasma Based Model for Energy-Transfer in Laser Material Processing*. Journal of Physics D-Applied Physics, 1990. **23**(6): p. 643-654.

72. Tix, C. and G. Simon, *A Transport Theoretical-Model of the Keyhole Plasma in Penetration Laser-Welding*. Journal of Physics D-Applied Physics, 1993. **26**(11): p. 2066-2074.
73. Kaplan, A., *A Model of Deep Penetration Laser-Welding Based on Calculation of the Keyhole Profile*. Journal of Physics D-Applied Physics, 1994. **27**(9): p. 1805-1814.
74. Beck, M., P. Berger, and H. Hugel, *The effect of plasma formation on beam focusing in deep penetration welding with CO₂ lasers*. Journal of Physics D-Applied Physics, 1995. **28**(12): p. 2430-2442.
75. Kim, K.R. and D.F. Farson, *CO₂ laser-plume interaction in materials processing*. Journal of Applied Physics, 2001. **89**(1): p. 681-688.
76. Ki, H., P.S. Mohanty, and J. Mazumder, *Modeling of laser keyhole welding: Part I. Mathematical modeling, numerical methodology, role of recoil pressure, multiple reflections, and free surface evolution*. Metallurgical and Materials Transactions a-Physical Metallurgy and Materials Science, 2002. **33**(6): p. 1817-1830.
77. Ki, H., P.S. Mohanty, and J. Mazumder, *Modeling of laser keyhole welding: Part II. Simulation of keyhole evolution, velocity, temperature profile, and experimental verification*. Metallurgical and Materials Transactions a-Physical Metallurgy and Materials Science, 2002. **33**(6): p. 1831-1842.
78. Zhang, D.M., et al., *A new model of pulsed laser ablation and plasma shielding*. Physica B-Condensed Matter, 2005. **362**(1-4): p. 82-87.
79. Tan, X.Y., et al., *Ionization effect to plasma expansion study during nanosecond pulsed laser deposition*. Physics Letters A, 2007. **370**(1): p. 64-69.
80. Mazhukin, V.I., V.V. Nossov, and I. Smurov, *Modeling of plasma-controlled surface evaporation and condensation of Al target under pulsed laser irradiation*. Applied Surface Science, 2007. **253**(19): p. 7686-7691.
81. Fang, Q.Y. and X.H. Hu, *Modeling of skin tissue ablation by nanosecond pulses from ultraviolet to near-infrared and comparison with experimental results*. Ieee Journal of Quantum Electronics, 2004. **40**(1): p. 69-77.
82. Kennedy, P.K., *A First-Order Model for Computation of Laser-Induced Breakdown Thresholds in Ocular and Aqueous-Media .I. Theory*. Ieee Journal of Quantum Electronics, 1995. **31**(12): p. 2241-2249.
83. Amoruso, S., *Modeling of UV pulsed-laser ablation of metallic targets*. Applied Physics a-Materials Science & Processing, 1999. **69**(3): p. 323-332.

84. Eidmann, K., et al., *Hydrodynamic simulation of subpicosecond laser interaction with solid-density matter*. Physical Review E, 2000. **62**(1): p. 1202-1214.
85. Ramis, R., R. Schmalz, and J. Meyertervehn, *Multi - a Computer Code for One-Dimensional Multigroup Radiation Hydrodynamics*. Computer Physics Communications, 1988. **49**(3): p. 475-505.
86. Itina, T.E., et al., *Numerical study of ultra-short laser ablation of metals and of laser plume dynamics*. Applied Physics a-Materials Science & Processing, 2004. **79**(4-6): p. 1089-1092.
87. Veysman, M.E., et al., *Femtosecond optical diagnostics and hydrodynamic simulation of Ag plasma created by laser irradiation of a solid target*. Journal of Physics B-Atomic Molecular and Optical Physics, 2008. **41**(12): p. 125704.
88. Jiang, L. and H.L. Tsai, *Plasma modeling for ultrashort pulse laser ablation of dielectrics*. Journal of Applied Physics, 2006. **100**(2): p. 023116.
89. Li, H.Y. and H.S. Ki, *Effect of ionization on femtosecond laser pulse interaction with silicon*. Journal of Applied Physics, 2006. **100**(10): p. 104907.
90. Itina, T.E., et al., *Laser-generated plasma plume expansion: Combined continuous-microscopic modeling*. Physical Review E, 2002. **66**(6): p. 066406.
91. Birdsall, C.K., *Particle-in-Cell Charged-Particle Simulations, Plus Monte-Carlo Collisions with Neutral Atoms, Pic-Mcc*. Ieee Transactions on Plasma Science, 1991. **19**(2): p. 65-85.
92. Birdsall, C.K. and A.B. Langdon, *Plasma physics via computer simulation*. 1985, New York: McGraw-Hill. xxiii, 479 p.
93. Hockney, R.W. and J.W. Eastwood, *Computer simulation using particles*. 1994, Bristol [England] ; Philadelphia: Institute of Physics Publishing. xxi, 540 p.
94. Chessa, P., P. Mora, and T.M. Antonsen, *Numerical simulation of short laser pulse relativistic self-focusing in underdense plasma*. Physics of Plasmas, 1998. **5**(9): p. 3451-3458.
95. Mora, P. and T.M. Antonsen, *Kinetic modeling of intense, short laser pulses propagating in tenuous plasmas*. Physics of Plasmas, 1997. **4**(1): p. 217-229.
96. Verboncoeur, J.P., A.B. Langdon, and N.T. Gladd, *An Object-Oriented Electromagnetic Pic Code*. Computer Physics Communications, 1995. **87**(1-2): p. 199-211.
97. Bruhwiler, D.L., et al., *Particle-in-cell simulations of plasma accelerators and electron-neutral collisions*. Physical Review Special Topics-Accelerators and Beams, 2001. **410**(10): p. art. no.-101302.

98. Bruhwiler, D.L., et al., *Particle-in-cell simulations of tunneling ionization effects in plasma-based accelerators*. Physics of Plasmas, 2003. **10**(5): p. 2022-2030.
99. Huang, C., et al., *QUICKPIC: A highly efficient particle-in-cell code for modeling wakefield acceleration in plasmas*. Journal of Computational Physics, 2006. **217**(2): p. 658-679.
100. Lefebvre, E., et al., *Electron and photon production from relativistic laser-plasma interactions*. Nuclear Fusion, 2003. **43**(7): p. 629-633.
101. d'Humieres, E., et al., *Proton acceleration mechanisms in high-intensity laser interaction with thin foils*. Physics of Plasmas, 2005. **12**(6): p. 062704.
102. Baton, S.D., et al., *Inhibition of fast electron energy deposition due to preplasma filling of cone-attached targets*. Physics of Plasmas, 2008. **15**(4): p. 042706.
103. Morse, R.L. and C.W. Nielson, *Numerical Simulation of Weibel Instability in One and 2 Dimensions*. Physics of Fluids, 1971. **14**(4): p. 830-840.
104. Decker, C.D., W.B. Mori, and T. Katsouleas, *Particle-in-Cell Simulations of Raman Forward Scattering from Short-Pulse High-Intensity Lasers*. Physical Review E, 1994. **50**(5): p. R3338-R3341.
105. Fonseca, R.A., et al., *OSIRIS: A three-dimensional, fully relativistic particle in cell code for modeling plasma based accelerators*. Computational Science-Iccs 2002, Pt Iii, Proceedings, 2002. **2331**: p. 342-351.
106. Lefebvre, E., et al., *Numerical modeling and applications of laser-accelerated ion beams*. Computer Physics Communications, 2007. **177**(1-2): p. 60-63.
107. Petrov, G.M., et al., *Modeling of clusters in a strong 248-nm laser field by a three-dimensional relativistic molecular dynamic model*. Physical Review E, 2005. **71**(3): p. 036411.
108. David, N. and S.M. Hooker, *Effects of polarization on inverse Bremsstrahlung heating of a plasma*. Physical Review E, 2005. **72**(3): p. 036402.
109. David, N., D.J. Spence, and S.M. Hooker, *Molecular-dynamic calculation of the inverse-bremsstrahlung heating of non-weakly-coupled plasmas*. Physical Review E, 2004. **70**(5): p. 056411.
110. Gibbon, P., et al., *Tree-code simulations of proton acceleration from laser-irradiated wire targets*. Physics of Plasmas, 2004. **11**(8): p. 4032-4040.
111. Matte, J.P. and J. Virmont, *Electron Heat-Transport down Steep Temperature-Gradients*. Physical Review Letters, 1982. **49**(26): p. 1936-1939.

112. Matte, J.P., et al., *Electron Heat-Flow with Inverse Bremsstrahlung and Ion Motion*. Physical Review Letters, 1984. **53**(15): p. 1461-1464.
113. Liu, J.M., *Measurements of inverse bremsstrahlung absorption and non-Maxwellian electron velocity distributions*. Physical Review Letters, 1994. **72**(17): p. 2717-2720.
114. Matte, J.P., et al., *Spectroscopic Signature of Non-Maxwellian and Nonstationary Effects in Plasmas Heated by Intense, Ultrashort Laser-Pulses*. Physical Review Letters, 1994. **72**(8): p. 1208-1211.
115. Ethier, S. and J.P. Matte, *Electron kinetic simulations of solid density Al plasmas produced by intense subpicosecond laser pulses. I. Ionization dynamics in 30 femtosecond pulses*. Physics of Plasmas, 2001. **8**(5): p. 1650-1658.
116. Marchand, R., S. Lafortune, and X. Bonnin, *Average Ion Approximation for Modeling Impurity Transport in Tokamaks*. Computer Physics Communications, 1993. **76**(2): p. 203-214.
117. Town, R.P.J., A.R. Bell, and S.J. Rose, *Fokker-Planck Simulations of Short-Pulse-Laser-Solid Experiments*. Physical Review E, 1994. **50**(2): p. 1413-1421.
118. Town, R.P.J., A.R. Bell, and S.J. Rose, *Fokker-Planck Calculations with Ionization Dynamics of Short-Pulse Laser-Solid Interactions*. Physical Review Letters, 1995. **74**(6): p. 924-927.
119. Batani, D., et al., *A cellular automaton model of laser-plasma interactions*. Laser and Particle Beams, 2001. **19**(4): p. 631-642.
120. Gusarov, A.V., A.G. Gnedovets, and I. Smurov, *Gas dynamics of laser ablation: Influence of ambient atmosphere*. Journal of Applied Physics, 2000. **88**(7): p. 4352-4364.
121. Itina, T.E., et al., *Monte Carlo simulation study of the effects of nonequilibrium chemical reactions during pulsed laser desorption*. Journal of Chemical Physics, 1997. **106**(21): p. 8905-8912.
122. Ruhl, H., et al. *Kinetic approach to superintense laser-solid interaction*. in *In Superstrong Fields in Plasmas*. 1998. Woodbury, CT: American Institute of Physics.
123. Chen, S. and G.D. Doolen, *Lattice Boltzmann method for fluid flows*. Annual Review of Fluid Mechanics, 1998. **30**: p. 329-364.
124. He, X.Y. and L.S. Luo, *A priori derivation of the lattice Boltzmann equation*. Physical Review E, 1997. **55**(6): p. R6333-R6336.

125. He, X.Y. and L.S. Luo, *Theory of the lattice Boltzmann method: From the Boltzmann equation to the lattice Boltzmann equation*. Physical Review E, 1997. **56**(6): p. 6811-6817.
126. Gombosi, T.I., *Gaskinetic theory*. 1994, Cambridge [England] ; New York: Cambridge University Press. xiv, 297.
127. Versteeg, H.K. and W. Malalasekera, *An introduction to computational fluid dynamics : the finite volume method*. 1995, Harlow, Essex, England Longman Scientific & Technical ; New York : Wiley. x, 257 p.
128. Bhatnagar, P.L., E.P. Gross, and M. Krook, *A Model for Collision Processes in Gases .I. Small Amplitude Processes in Charged and Neutral One-Component Systems*. Physical Review, 1954. **94**(3): p. 511-525.
129. Bittencourt, J.A., *Fundamentals of plasma physics*. 3rd ed. 2004, New York: Springer. xxiii, 678 p.
130. Oxenius, J., *Kinetic theory of particles and photons : theoretical foundations of non-LTE plasma spectroscopy*. 1986, Berlin ; New York: Springer-Verlag. xii, 353 p.
131. Epperlein, E.M., *Implicit and Conservative Difference Scheme for the Fokker-Planck Equation*. Journal of Computational Physics, 1994. **112**(2): p. 291-297.
132. Mousseau, V.A. and D.A. Knoll, *Fully implicit kinetic solution of collisional plasmas*. Journal of Computational Physics, 1997. **136**(2): p. 308-323.
133. Bobylev, A.V. and K. Nanbu, *Theory of collision algorithms for gases and plasmas based on the Boltzmann equation and the Landau-Fokker-Planck equation*. Physical Review E, 2000. **61**(4): p. 4576-4586.
134. He, X.Y. and L.S. Luo, *Lattice Boltzmann model for the incompressible Navier-Stokes equation*. Journal of Statistical Physics, 1997. **88**(3-4): p. 927-944.
135. Hou, S.L., et al., *Simulation of Cavity Flow by the Lattice Boltzmann Method*. Journal of Computational Physics, 1995. **118**(2): p. 329-347.
136. Chen, R.H., et al., *Simulation of viscous flow in a 2D-cavity by the lattice Boltzmann method*. Acta Physica Sinica, 2000. **49**(4): p. 631-635.
137. Yu, D.Z., et al., *Viscous flow computations with the method of lattice Boltzmann equation*. Progress in Aerospace Sciences, 2003. **39**(5): p. 329-367.
138. Guo, Z.L., C.G. Zheng, and B.C. Shi, *Discrete lattice effects on the forcing term in the lattice Boltzmann method*. Physical Review E, 2002. **65**(4): p. 046308.

139. He, X.Y., et al., *Analytic solutions of simple flows and analysis of nonslip boundary conditions for the lattice Boltzmann BGK model*. Journal of Statistical Physics, 1997. **87**(1-2): p. 115-136.
140. Martys, N.S., X.W. Shan, and H.D. Chen, *Evaluation of the external force term in the discrete Boltzmann equation*. Physical Review E, 1998. **58**(5): p. 6855-6857.
141. Luo, L.S., *Unified theory of lattice boltzmann models for nonideal gases*. Physical Review Letters, 1998. **81**(8): p. 1618-1621.
142. Luo, L.S., *Theory of the lattice Boltzmann method: Lattice Boltzmann models for nonideal gases*. Physical Review E, 2000. **62**(4): p. 4982-4996.
143. Ladd, A.J.C. and R. Verberg, *Lattice-Boltzmann simulations of particle-fluid suspensions*. Journal of Statistical Physics, 2001. **104**(5-6): p. 1191-1251.
144. Breyiannis, G. and D. Valougeorgis, *Lattice kinetic simulations in three-dimensional magnetohydrodynamics*. Physical Review E, 2004. **69**(6): p. 065702(R).
145. Buick, J.M. and C.A. Greated, *Gravity in a lattice Boltzmann model*. Physical Review E, 2000. **61**(5): p. 5307-5320.
146. He, X.Y., X.W. Shan, and G.D. Doolen, *Discrete Boltzmann equation model for nonideal gases*. Physical Review E, 1998. **57**(1): p. R13-R16.
147. Nourgaliev, R.R., et al., *The lattice Boltzmann equation method: theoretical interpretation, numerics and implications*. International Journal of Multiphase Flow, 2003. **29**(1): p. 117-169.
148. Li, B.M. and D.Y. Kwok, *Discrete Boltzmann equation for microfluidics*. Physical Review Letters, 2003. **90**(12): p. 124502.
149. Li, B.M. and D.Y. Kwok, *Lattice Boltzmann model of microfluidics with high Reynolds numbers in the presence of external forces*. Langmuir, 2003. **19**(7): p. 3041-3048.
150. Gunstensen, A.K., et al., *Lattice Boltzmann Model of Immiscible Fluids*. Physical Review A, 1991. **43**(8): p. 4320-4327.
151. Swift, M.R., W.R. Osborn, and J.M. Yeomans, *Lattice Boltzmann Simulation of Nonideal Fluids*. Physical Review Letters, 1995. **75**(5): p. 830-833.
152. Grunau, D., S.Y. Chen, and K. Eggert, *A Lattice Boltzmann Model for Multiphase Fluid-Flows*. Physics of Fluids a-Fluid Dynamics, 1993. **5**(10): p. 2557-2562.

153. Succi, S., *The lattice Boltzmann equation for fluid dynamics and beyond*. Numerical mathematics and scientific computation. 2001, Oxford, New York: Clarendon Press ; Oxford University Press. xvi, 288 p.
154. Makabe, T., *Plasma Electronics : Applications in Microelectronic Device Fabrication*. 2006, Hoboken: CRC Press. 355.
155. Chen, S.Y., et al., *Lattice Boltzmann Model for Simulation of Magnetohydrodynamics*. Physical Review Letters, 1991. **67**(27): p. 3776-3779.
156. Martinez, D.O., S.Y. Chen, and W.H. Matthaeus, *Lattice Boltzmann Magnetohydrodynamics*. Physics of Plasmas, 1994. **1**(6): p. 1850-1867.
157. Schaffnerberger, W. and A. Hansmeier, *Two-dimensional lattice Boltzmann model for magnetohydrodynamics*. Physical Review E, 2002. **66**(4): p. 046702.
158. Dellar, P.J., *Lattice kinetic schemes for magnetohydrodynamics*. Journal of Computational Physics, 2002. **179**(1): p. 95-126.
159. Orszag, S.A. and C.M. Tang, *Small-Scale Structure of 2-Dimensional Magnetohydrodynamic Turbulence*. Journal of Fluid Mechanics, 1979. **90**(JAN): p. 129-143.
160. Dahlburg, R.B. and J.M. Picone, *Evolution of the Orszag-Tang Vortex System in a Compressible Medium .1. Initial Average Subsonic Flow*. Physics of Fluids B-Plasma Physics, 1989. **1**(11): p. 2153-2171.
161. Mei, R., et al., *Lattice Boltzmann method for 3-D flows with curved boundary*. Journal of Computational Physics, 2000. **161**(2): p. 680-699.
162. Grauer, R. and C. Marliani, *Current-sheet formation in 3D ideal incompressible magnetohydrodynamics*. Physical Review Letters, 2000. **84**(21): p. 4850-4853.
163. Finn, J.M. and P.K. Kaw, *Coalescence Instability of Magnetic Islands*. Physics of Fluids, 1977. **20**(1): p. 72-78.
164. Longcope, D.W. and H.R. Strauss, *The Coalescence Instability and the Development of Current Sheets in 2-Dimensional Magnetohydrodynamics*. Physics of Fluids B-Plasma Physics, 1993. **5**(8): p. 2858-2869.
165. Marliani, C. and H.R. Strauss, *Reconnection of coalescing magnetic islands*. Physics of Plasmas, 1999. **6**(2): p. 495.
166. Luo, L.S. and S.S. Girimaji, *Lattice Boltzmann model for binary mixtures*. Physical Review E, 2002. **66**(3): p. 035301.
167. Sofonea, V. and R.F. Sekerka, *BGK models for diffusion in isothermal binary fluid systems*. Physica A, 2001. **299**(3-4): p. 494-520.

168. Guo, Z.L. and T.S. Zhao, *Finite-difference-based lattice Boltzmann model for dense binary mixtures*. Physical Review E, 2005. **71**(2): p. 026701.
169. Xu, A.G., *Finite-difference lattice-Boltzmann methods for binary fluids*. Physical Review E, 2005. **71**(6): p. 066706.
170. Asinari, P., *Viscous coupling based lattice Boltzmann model for binary mixtures*. Physics of Fluids, 2005. **17**(6): p. 067102.
171. Sofonea, V. and R.F. Sekerka, *Diffuse-reflection boundary conditions for a thermal lattice Boltzmann model in two dimensions: Evidence of temperature jump and slip velocity in microchannels*. Physical Review E, 2005. **71**(6): p. 066709.
172. He, X.Y., L.S. Luo, and M. Dembo, *Some progress in lattice Boltzmann method .I. Nonuniform mesh grids*. Journal of Computational Physics, 1996. **129**(2): p. 357-363.
173. Guo, Z.L., C.G. Zheng, and T.S. Zhao, *A lattice BGK scheme with general propagation*. Journal of Scientific Computing, 2001. **16**(4): p. 569.
174. He, X.Y. and G.D. Doolen, *Lattice Boltzmann method on a curvilinear coordinate system: Vortex shedding behind a circular cylinder*. Physical Review E, 1997. **56**(1): p. 434-440.
175. He, X.Y., L.S. Luo, and M. Dembo, *Some progress in the lattice Boltzmann method: Reynolds number enhancement in simulations*. Physica A, 1997. **239**(1-3): p. 276-285.
176. Dunweg, B., U.D. Schiller, and A.J.C. Ladd, *Statistical mechanics of the fluctuating lattice Boltzmann equation*. Physical Review E, 2007. **76**(3): p. 036704.
177. Boghosian, B.A., et al., *Galilean-invariant multi-speed entropic lattice Boltzmann models*. Physica D-Nonlinear Phenomena, 2004. **193**(1-4): p. 169-181.
178. Chikatamarla, S.S., S. Ansumali, and I.V. Karlin, *Entropic lattice Boltzmann models for hydrodynamics in three dimensions*. Physical Review Letters, 2006. **97**(1): p. 010201.
179. Ghia, U., K.N. Ghia, and C.T. Shin, *High-Re Solutions for Incompressible-Flow Using the Navier Stokes Equations and a Multigrid Method*. Journal of Computational Physics, 1982. **48**(3): p. 387-411.
180. He, X.Y. and G. Doolen, *Lattice Boltzmann method on curvilinear coordinates system: Flow around a circular cylinder*. Journal of Computational Physics, 1997. **134**(2): p. 306-315.

181. Li, H.Y. and H. Ki, *Lattice Boltzmann method for weakly ionized isothermal plasmas*. Physical Review E, 2007. **76**(6): p. 066707.
182. Kim, Y.K. and M.E. Rudd, *Binary-Encounter-Dipole Model for Electron-Impact Ionization*. Physical Review A, 1994. **50**(5): p. 3954-3967.
183. Shah, M.B., et al., *Single and Double Ionization of Helium by Electron-Impact*. Journal of Physics B-Atomic Molecular and Optical Physics, 1988. **21**(15): p. 2751-2761.
184. Montague, R.G., M.F.A. Harrison, and A.C.H. Smith, *A Measurement of the Cross-Section for Ionization of Helium by Electron-Impact Using a Fast Crossed Beam Technique*. Journal of Physics B-Atomic Molecular and Optical Physics, 1984. **17**(16): p. 3295-3310.
185. Kemp, A.J., R.E.W. Pfund, and J. Meyer-ter-Vehn, *Modeling ultrafast laser-driven ionization dynamics with Monte Carlo collisional particle-in-cell simulations*. Physics of Plasmas, 2004. **11**(12): p. 5648-5657.
186. Taflove, A. and S.C. Hagness, *Computational electrodynamics : the finite-difference time-domain method*. 2nd ed. Artech House antennas and propagation library. 2000, Boston: Artech House. xxiii, 852 p.
187. Berenger, J.P., *A Perfectly Matched Layer for the Absorption of Electromagnetic-Waves*. Journal of Computational Physics, 1994. **114**(2): p. 185-200.
188. Sacks, Z.S., et al., *A perfectly matched anisotropic absorber for use as an absorbing boundary condition*. Ieee Transactions on Antennas and Propagation, 1995. **43**(12): p. 1460-1463.
189. Kaganov, M.I., I.M. Lifshitz, and L.V. Tanatarov, *Relaxation between Electrons and the Crystalline Lattice*. Soviet Physics JETP-USSR, 1957. **4**(2): p. 173-178.

MICHIGAN STATE UNIVERSITY LIBRARIES



3 1293 03062 4328